



National Library
of Canada

Bibliothèque nationale
du Canada

Canadian Theses Service Service des thèses canadiennes

Ottawa, Canada
K1A 0N4

NOTICE

The quality of this microform is heavily dependent upon the quality of the original thesis submitted for microfilming. Every effort has been made to ensure the highest quality of reproduction possible.

If pages are missing, contact the university which granted the degree.

Some pages may have indistinct print especially if the original pages were typed with a poor typewriter ribbon or if the university sent us an inferior photocopy.

Previously copyrighted materials (journal articles, published tests, etc.) are not filmed.

Reproduction in full or in part of this microform is governed by the Canadian Copyright Act, R.S.C. 1970, c. C-30.

AVIS

La qualité de cette microforme dépend grandement de la qualité de la thèse soumise au microfilmage. Nous avons tout fait pour assurer une qualité supérieure de reproduction.

S'il manque des pages, veuillez communiquer avec l'université qui a conféré le grade.

La qualité d'impression de certaines pages peut laisser à désirer, surtout si les pages originales ont été dactylographiées à l'aide d'un ruban usé ou si l'université nous a fait parvenir une photocopie de qualité inférieure.

Les documents qui font déjà l'objet d'un droit d'auteur (articles de revue, tests publiés, etc.) ne sont pas microfilmés.

La reproduction, même partielle, de cette microforme est soumise à la Loi canadienne sur le droit d'auteur, SRC 1970, c. C-30.

THE UNIVERSITY OF ALBERTA

FABRICATION AND CHARACTERIZATION OF
SILICON-DOPING SUPERLATTICES

BY



GRAHAM HUGH MCKINNON

A THESIS

SUBMITTED TO THE FACULTY OF GRADUATE STUDIES AND RESEARCH
IN PARTIAL FULFILMENT OF THE REQUIREMENTS FOR THE DEGREE
OF MASTER OF SCIENCE

DEPARTMENT OF ELECTRICAL ENGINEERING

EDMONTON, ALBERTA

SPRING 1988

Permission has been granted to the National Library of Canada to microfilm this thesis and to lend or sell copies of the film.

L'autorisation a été accordée à la Bibliothèque nationale du Canada de microfilmer cette thèse et de prêter ou de vendre des exemplaires du film.

The author (copyright owner) has reserved other publication rights, and neither the thesis nor extensive extracts from it may be printed or otherwise reproduced without his/her written permission.

L'auteur (titulaire du droit d'auteur) se réserve les autres droits de publication; ni la thèse ni de longs extraits de celle-ci ne doivent être imprimés ou autrement reproduits sans son autorisation écrite.

ISBN 0-315-42819-8

THE UNIVERSITY OF ALBERTA

RELEASE FORM

NAME OF AUTHOR: GRAHAM HUGH MCKINNON

TITLE OF THESIS: FABRICATION AND CHARACTERIZATION OF SILICON DOPING
SUPERLATTICES

DEGREE: MASTER OF SCIENCE

YEAR THIS DEGREE GRANTED: SPRING 1988

Permission is hereby granted to THE UNIVERSITY OF ALBERTA LIBRARY to reproduce single copies of this thesis and to lend or sell such copies for private, scholarly or scientific research purposes only.

The author reserves other publication rights, and neither the thesis nor extensive extracts from it may be printed or otherwise reproduced without the author's written permission.

G. McKinnon

Box 1162

Beaumont, Alberta T0C 0H0A

Date: *Apr. 24, 1988*

THE UNIVERSITY OF ALBERTA
FACULTY OF GRADUATE STUDIES AND RESEARCH

The undersigned certify that they have read, and recommend to the Faculty of Graduate Studies and Research for acceptance, a thesis entitled FABRICATION AND CHARACTERIZATION OF SILICON DOPING SUPERLATTICES submitted by GRAHAM HUGH MCKINNON in partial fulfilment of the requirements for the degree of MASTER OF SCIENCE in ELECTRICAL ENGINEERING.

J. V. McMillin
Supervisor

William J. Brennan
Supervisor

Frank C. Weighman

M. Brett

Date: *Mar 9, 1988*

ABSTRACT

Silicon doping superlattices have been fabricated and some characterization of the electrical and optical characteristics has been performed. An etched silicon shadow mask was produced using an anisotropic chemical etch. This mask was used to shadow the impurities during MBE to grow silicon doping superlattice mesas with intrinsic layers at the edges. Selective contacts were made to the mesa which formed interdigital contacts with the superlattice layers. Electrical behavior of the contacts and the superlattice is compared with current transport theory. Although reasonable diode behavior has been attained, substrate leakage currents due to carrier generation are found to be substantial. The conductance of the layers was measured using a split contact arrangement and is found to vary with an applied bias across the superlattice.

The optical absorption in moderate width silicon doping superlattices is studied theoretically. The large internal fields developed across the p-n layers will result in optical absorption at energies less than the fundamental edge due to the Franz-Keldysh effect. Measurements have been made of the photoconductive response of the silicon superlattice. The absorption shift has not been observed as yet due to the poor substrate isolation and lower than expected internal fields.

ACKNOWLEDGEMENTS

It is a pleasure to express my gratitude to Dr. J.N. McMullin and Dr. H.G. Schmidt-Weinmar, my supervisors, for their strong support throughout this project. Their advice and encouragement is greatly appreciated.

This project has been a cooperative effort with many individuals involved. I owe a great deal of thanks to a great number of people for the help and support they have given me. I would like to take this opportunity to express my thanks (working my way west):

Dr. B. Landheer (NRC) for his active participation in this project. A great deal of the research in this thesis stems directly from his work and I am indebted to him for his support.

Dr. M.A. Buchanan (NRC) for the countless hours put into developing a suitable processing procedure for the mesa contacts. Also for numerous advices and for the SEM and microscope photographs.

Dr. M.W. Denhoff (NRC) for MBE growth of superlattices. Also for 4-point probe data and numerous advices.

Dr. R. Normandin (NRC) for his generous assistance with lifetime measurements including use of equipment and useful discussion.

Dr. P. Janega (NRC) for information on contacts and for processing.

Dr. T.E. Jackman (NRC) and Dr. J.A. Jackman (CNET) for their great care in the SIMS analysis and also for their hospitality.

P. Chow-Chong (NRC) for his expert skill in microscopy processing.

Other NRC staff who assisted in this project including Dr. E. Kornelson and Dr. D. Houghton for processing and Paul Marshall for microbonding and other assistance.

Dr. G. Tarr, H. Robillard and L. Berndt (U. of Carleton, Dept. of E.E.)
for platinum sputtering of contacts.

Dr. M. Brett (U. of A., E.E.) for advice on silicon etching, surface
mobility during MBE growth, and for making the AMC facilities
available. Also for silicon wafers.

Dr. F. Weichman (U. of Physics) for use of equipment and advice for
initial photoconductivity measurements.

Dr. J. Tulip and M. Paulson (U. of A., E.E.) for use of a furnace for
oxide growth on wafers.

Dr. A. Kalantar (U. of A., Chemistry) for advice on properties of
chemical etchants and use of equipment.

Dr. Kumar (U. of A., Physical Therapy) for use of computing equipment
to transfer data files from NRC.

K. Westra for advice and assistance with AMC facilities.

A. Parameswaran for assistance with photoresist and micro-photography.

Other AMC associates who assisted me including: C. Eastman for advice
on oxide growth and for supplying wafers with oxide for test
etching. Jo Weichman for wafer priming and photography. M.
Buchbinder for surface profile measurements. C. Finley for advice
and for photoresist and developer. Glen Fitzpatrick for
assistance with equipment and microbonding. T. Smy for help with
equipment.

I also wish to express my sincere thanks to my colleague, K.H. Teo. He
has been a constant source of encouragement and inspiration. I
wish him the very best in his continuing work with this project.

TABLE OF CONTENTS

CHAPTER	PAGE
1. Introduction	1
2. Fabrication	5
2.1 Shadow Mask Method	5
2.1.1 Shadow Mask and Contact Design	12
2.2 Fabrication of the Shadow Mask	18
2.2.1 Silicon Anisotropic Etching	18
2.2.2 Shadow Mask Results	24
2.3 Superlattice Fabrication	26
2.4 Contact Fabrication	36
3. Contact Characteristics	44
3.1 Metal-Semiconductor Contacts	44
3.2 Reverse Bias Effects	49
3.3 P-side Contacts	52
3.4 N-side Contacts	60
4. Electrical Characteristics	68
4.1 Notes on Substrate Effects	70
4.2 Reverse Bias Characteristics	78
4.3 Forward Bias Characteristics	85
4.4 Transconductance	95
5. Optical Characteristics	104
5.1 Modelling of Nipi Absorption	104
5.2 Photoconductivity Measurements	113
6.0 Summary and Conclusions	121
References	124
Appendix A	127

LIST OF TABLES

TABLE	PAGE
2.1 Summary of MBE Growth Runs.	35
3.1 Schottky Barrier Lowering.	51
3.2 Summary of PtSi Results.	55
3.3 Summary of Magnesium Results.	66
4.1 Comparison of Figs. 4.3 and 4.4.	77
4.2 Minority Carrier Diffusion Current.	80
4.3 Generation Current.	81
4.4 Metal-Semiconductor Schottky Current.	81
4.5 Forward Bias Results for Nipi Diodes.	90
4.6 Transconductance Background Levels.	103

LIST OF FIGURES

FIGURE		PAGE
2.1	Shadow mask method of MBE growth.	7
2.2	Geometry of NRC MBE chamber.	8
2.3	MBE geometry indicating location of 3" substrate.	9
2.4a	Surface profile of a mesa edge for MBE #318.	11
2.4b	Idealized diagram of superlattice layers at the edge of the mesa.	11
2.5	Layout of shadow mask pattern.	14
2.6	Mask pattern set for shadow mask and contact processing.	15
2.7	Final arrangement of contacts.	17
2.8	Anisotropic etching of silicon.	19
2.9a	Variation of boron concentration across 3" wafer.	30
2.9b	Variation of arsenic concentration across 3" wafer.	30
2.10	Variation in silicon thickness across 3" wafer.	31
2.11	SIMS analysis of doping concentrations in MBE 360 #8B.	32
2.12	SIMS analysis of doping concentrations in MBE 360 #1C.	33
3.1	Energy level diagram for a metal-semiconductor junction.	46
3.2	Effect of a thin oxide layer between a metal and a semiconductor.	53
3.3a	I vs V for PtSi on 6 Ω -cm p-type silicon.	56
3.3b	I vs V for PtSi on 0.02 Ω -cm p-type silicon.	56
3.4	I vs V for PtSi on 4 Ω -cm n-type silicon.	58
3.5a	I vs V for PtSi on FZ substrate.	59
3.5b	I vs V for PtSi on FZ substrate showing increased leakage at higher voltages.	59

3.6a	I vs V for Mg on 4 Ω -cm n-type silicon.	62
3.6b	I vs V for Mg on 0.02 Ω -cm n-type silicon.	62
3.7	I vs V for Mg on FZ substrate.	64
3.8	I vs V for aluminum on FZ substrate.	64
3.9a	I vs V for gold-antimony on n-type substrate.	67
3.9b	I vs V for gold-antimony on FZ substrate.	67
4.1	I vs V of a nipi diode for MBE 360 #1E.	69
4.2	Mesa-to-mesa contacts and I-V measurement.	72
4.3a	I vs V for PtSi contacts, substrate pairs for MBE 360 #4B.	74
4.3b	I vs V for PtSi contacts, mesa-to-mesa for MBE 360 #4B.	74
4.4a	I vs V for PtSi contacts, substrate pairs for MBE 391 #5E.	76
4.4b	I vs V for PtSi contacts, mesa-to-mesa for MBE 391 #5E.	76
4.5	Diagram of reverse bias leakage paths.	79
4.6	I vs V for MBE 360 # 1E showing low current behavior.	83
4.7	Log(I) vs V_a for MBE 360 #1E.	87
4.8	MBE 360 #1E I-V curve for low forward bias.	91
4.9a	MBE 360 #1E I-V curve for large forward bias.	93
4.9b	Same as Fig. 4.9a except with $I_{s0} = 1 \times 10^{-16}$ A.	93
4.10	MBE 360 #4B I-V curve for large forward bias.	94
4.11	Circuit setup for transconductance measurements.	96
4.12a	Cross-sectional view of transconductance measurement across split contacts.	97
4.12b	Typical I vs V characteristics for a FET.	97

4.13a	Set of I-V curves collected across the split contacts,	100
4.13b	I-V curves of Fig. 4.13a with offset removed.	100
4.14a	Transconductance G_{pp} for MBE 360 #4B.	102
4.14b	Transconductance G_{nn} for MBE 360 #4B.	102
5.1	Energy band diagram for a silicon doping superlattice.	105
5.2	Optical absorption coefficient vs photon energy at $T=300^{\circ}\text{K}$.	111
5.3	Optical absorption coefficient vs photon energy at $T=77^{\circ}\text{K}$.	112
5.4	Measurement setup for photoconductivity.	115
5.5	Photoconductivity for bulk silicon.	117
5.6	Typical photoconductivity measurement of a nipi.	118
5.7	Typical photoconductivity measurement of a nipi at 77°K .	119

LIST OF PHOTOGRAPHIC PLATES

PLATE	PAGE
Ia Mesa edge and superlattice layers.	41
Ib Window opening in the silicon shadow mask.	41
Ic Detail of an etched edge of the shadow mask.	41
Id Shadow mask with a major fault along one edge.	41
Ie Sloping faces and window opening of the shadow mask.	41
If Portion of shadow mask showing windows for two cells.	41
IIa Corner of a mesa from MBE 360.	43
IIb Detail of the rough MBE growth from MBE 360.	43
IIc Mesa with contacts produced with the first mask.	43
IId Corner of a mesa and with a PtSi contact.	43
IIe Split contact mesa.	43
IIf Mesa and substrate after surface etch.	43

LIST OF SYMBOLS

CZ	Czochralski method of crystal growth
d_n, d_p	thickness of n-type (p-type) layer
D_n, D_p	diffusion constant for electrons (holes)
E_c	energy level of conduction band
E_f	Fermi energy level
E_g	energy bandgap
E_v	energy level of valence band
FZ	floating-zone method of crystal growth
G_{nn}, G_{pp}	transconductance of n-type (p-type) layers
I_g	generation current density
I_{ms}	current density for a Schottky barrier
I_r	recombination current density
I_s	current density for an ideal diode
k	Boltzmann's constant
kT/q	thermal voltage
L_n, L_p	diffusion length of minority carrier electrons (holes)
M-S	metal-semiconductor
n_i	intrinsic carrier concentration
n, p	electron (hole) carrier density
N_d, N_a	donor (acceptor) impurity density
N_c, N_v	effective density of states in conduction (valence) band
q	electronic charge
R_c	contact resistance in M-S junction
R_d	diode resistance
V_a	applied voltage

x_d width of the space charge region
 α absorption coefficient
 ϵ dielectric constant for silicon
 ϕ_{Bn} Schottky barrier height for electrons
 ϕ_{Bp} Schottky barrier height for holes
 ϕ_i built-in potential at a junction
 ρ resistivity

 τ_n, τ_p minority carrier lifetime for electrons (holes)
 τ effective recombination lifetime
 $h\nu$ photon energy
 μ_n, μ_p electron (hole) mobility

Chapter 1

Introduction

The use of ultra-thin alternating layers of semiconductor material to fabricate structures with novel electronic properties was first investigated in 1970 [1]. Two types of superlattices were proposed: (a) compositional superlattices made of alternating layers of semiconductor materials having different energy bandgaps and (b) doping superlattices consisting of a single semiconductor crystal with alternating layers of p-type and n-type impurities. The name "nipi" was coined for doping superlattices after the original anticipated composition of a four layer period consisting of n-type, intrinsic, p-type, intrinsic layers [2].

A doping superlattice is characterized by a constant bandgap throughout with the energy levels of the conduction and valence bands being spatially modulated. The narrow period results in a bandgap that may be considered as indirect in real space. The difference between the conduction band minimum and the valence band maximum, called the "effective bandgap", is tunable and this tunability may induce other interesting effects. Many novel properties including tunable luminescence, tunable absorption and extremely long lifetimes were predicted for nipi's and have since been observed. The majority of the research to date on doping superlattices has been with III-V compounds, in particular GaAs. For a current review see Döhler [3].

Recent advancements in silicon epitaxial growth, such as molecular beam epitaxy (MBE) [4,5] have made the fabrication of silicon doping superlattices practical. Many of the interesting properties found in the III-V nipi's are also expected in silicon. However there will be

some differences. In addition to the larger effective masses and the smaller bandgap, silicon is an indirect bandgap material (in k-space).

When this work commenced, there was no published research on silicon doping superlattices. Since then, self-consistent calculations of the electron sub-band energies have been independently reported by two groups [6,7] in addition to the work carried out at the University of Alberta [8]. Experimental results have also started to appear. An enhanced Hall mobility in silicon nipi's grown by MBE has been investigated [9]. Silicon nipi's grown by iterated solid phase epitaxy (ISPE) have also been reported along with photoluminescence spectra [10].

The original goal of this project was to investigate the tunable absorption properties of silicon doping superlattices. Preliminary studies of the tunability of the effective bandgap demonstrated the feasibility of fabricating nipi's with tunable parameters from silicon [8]. A theoretical study of the optical absorption near the fundamental edge for silicon nipi's was undertaken [11]. The results of this study are presented in Chapter 5.

In order to experimentally verify the results of this study, work was undertaken in conjunction with the Microstructural Sciences Laboratory at the National Research Council in Ottawa to fabricate silicon doping superlattices with selective contacts to the n and p-type layers. The problems and complications associated with the fabrication proved to be far more extensive than first anticipated. Selective contacts on a silicon nipi have never been fabricated previously. A major portion of this project deals with the more basic aspects of silicon nipi's, namely, fabrication, selective contacts and

fundamental electrical properties.

A major problem associated with the measurement of the electronic properties of doped superlattices is selective contacts. The n-type and p-type layers must be separately contacted. In GaAs, this has been accomplished for low doping levels by diffusion of the appropriate selective metals through the layers. Contacts formed in this manner have been used for tunable absorption measurements in GaAs [12]. However, at higher doping levels ($>10^{18} \text{ cm}^{-3}$), selective contacts cannot be formed in this way due to tunnelling effects [13]. An ingenious method of providing selective contacts has been devised and used successfully with GaAs [14]. The technique makes use of the MBE geometry and a shadow mask to form grown-in selective contacts during epitaxial growth of the superlattice. Tunable absorption measurements of GaAs nipi's using selective contacts made by this method have been reported [15,16]. The shadow mask method is used in this project to produce selective contacts on silicon nipi's.

Chapter 2 discusses the fabrication aspects of this project including shadow mask etching, superlattice growth and contact processing. The design of the shadow mask and the contact mask is described. Shadow masks have been fabricated from silicon wafers using an anisotropic chemical etch. The method of making these masks and the results obtained are presented. The shadow masks were used during MBE growth to produce superlattice mesas with built-in selective contacts. Complications associated with MBE growth, and SIMS results for some of the samples are given. As well, processing and etching procedures are outlined for making the contacts. For the first time, the shadow mask

method has been used to make selective contacts on a silicon doping superlattice.

The rectifying and ohmic contacts required for the selective contacts proved to be more elusive than first expected. Chapter 3 presents the electrical characteristics of the various contact metals investigated and discusses some of the reasons for their behavior.

In Chapter 4, the electrical properties of the nipi are investigated, including the large reverse bias leakage currents that have been observed. Initial results indicate that substrate effects may be quite substantial. The electrical behavior of the nipi under reverse and forward bias is compared with current transport models. Results for the conductance through the n and p-type layers are also presented. A silicon nipi has indeed been produced and the long lifetimes expected in a nipi have been observed [17].

Chapter 5 investigates some of the optical properties associated with silicon nipi's. A summary of the tunable absorption calculations for a silicon nipi is presented. The measurement method and preliminary results of the photoconductivity measurements are also given.

The fabrication of the silicon doping superlattices requires three separate fabrication stages. The first is the fabrication of the silicon shadow mask. The shadow mask is made from a silicon wafer which has been "micro-machined" using an anisotropic chemical etch. The second stage of fabrication is MBE growth of the superlattice using the shadow mask. The procedure is different from normal MBE growth since the substrate is shielded by the shadow mask and is not rotating. The third stage includes the lithography and processing of the contact metals required for the selective contacts.

This chapter outlines the shadow mask method and describes the design of the shadow mask and the contact masks. In addition, the procedures and results for each of the three fabrication stages are presented.

2.1 Shadow Mask Method

Selective contacts to the n and p-type layers are vital to realizing the full potential of doping superlattices. One approach to this problem is through the use of a shadow mask. This technique, first used by Döhler [14] involves forming selective contacts in situ during MBE growth. The arrangement makes use of the fact that in the MBE chamber, the molecular beams have different angles of incidence for the various sources.

The shadow mask is used to block the deposition of the doping impurities from certain regions. Such an arrangement is depicted in Fig. 2.1a. The silicon source is situated directly over the mask and

as the silicon is deposited, an epitaxial mesa will be formed having the same outline as the opening in the mask. The p-type and n-type doping sources are offset from the central axis on each side of the silicon source. One side of the mesa will be shadowed from the n-type impurity while the other side is shadowed from the p-type.

As the two shutters which control the impurity deposition are opened and closed, a p-n-p-n structure will be formed in the central region of the mesa. On the side of the mesa that is shadowed from the p-type impurity, an n-i-n-i type of structure will result. Similarly, the other side of the mesa will consist of a p-i-p-i structure. (See Fig. 2.1b.) The formation of selective contacts is now much easier as tunnelling effects to the opposing layers have been eliminated, however rectifying contacts are still required with the intrinsic regions.

The physical arrangement of the MBE chamber at the NRC is shown in Fig. 2.2. The doping sources are offset from the central axis by about 17° . As will be discussed later, a silicon wafer $400\mu\text{m}$ thick is used for the shadow mask making the intrinsic regions on each side of the mesa about $120\mu\text{m}$ wide. The mask and substrate are supported by a holder and the molecular beams travel from below, up to the wafers. The NRC system is designed for 4" wafers so a tantalum insert was fabricated in order to hold the 3" masks and substrates used for the nipi's. The arrangement is viewed from above in Fig. 2.3 with the 3" substrate, 4" holder and the doping and silicon sources shown in their relative positions.

The case described above is for a mesa centered on the axis in line with the silicon source, but this will not be the case for the majority of the mesas. As the shadow mask window is moved further

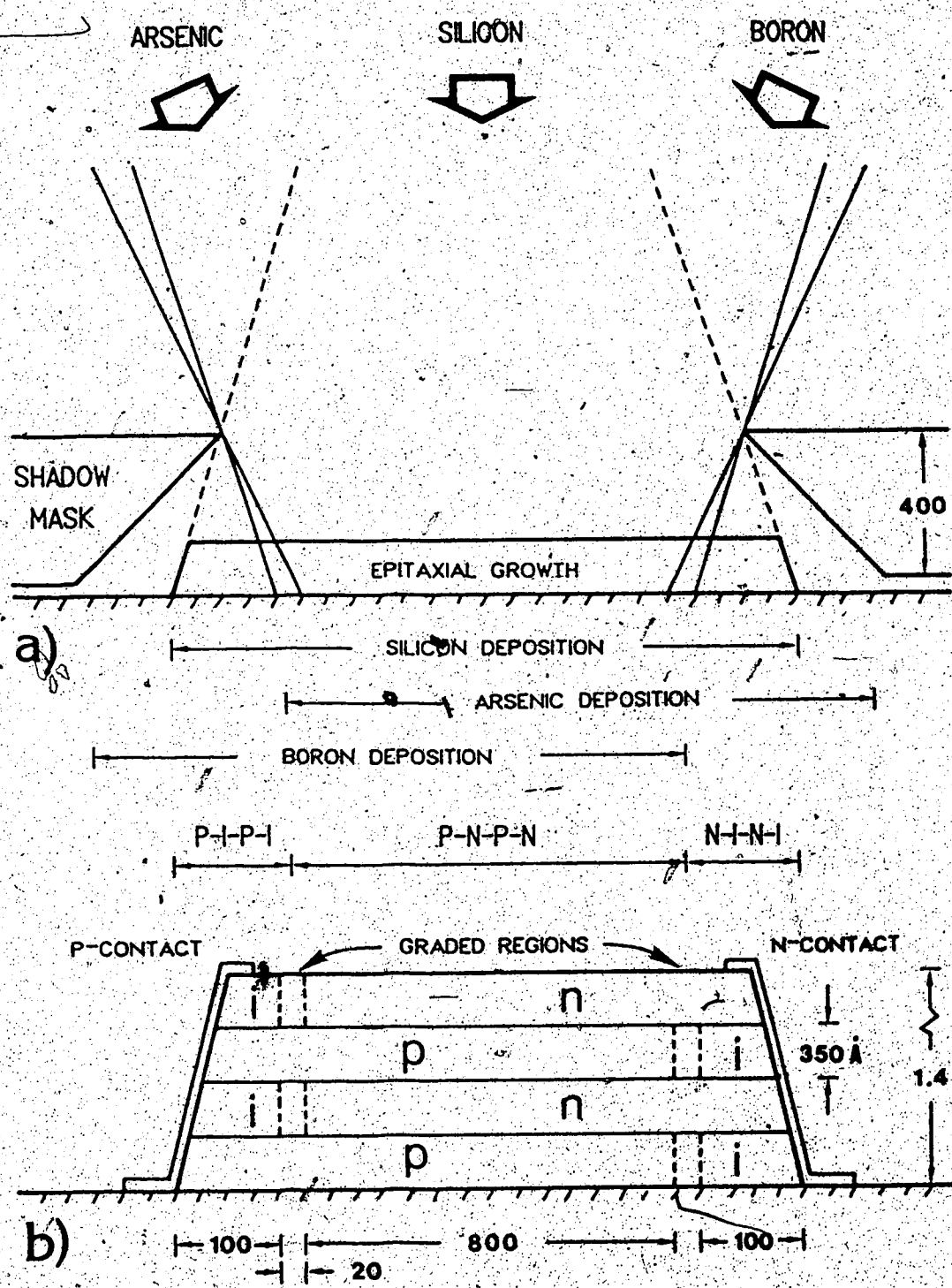


Fig. 2.1 Shadow mask method of MBE growth.
 a) Relative position of shadow mask and nipi mask.
 b) Cross section of a doping superlattice with built in contacts. Dimensions are in microns unless otherwise marked. Drawn for a four layer superlattice; typically 20 to 40 layers were grown.

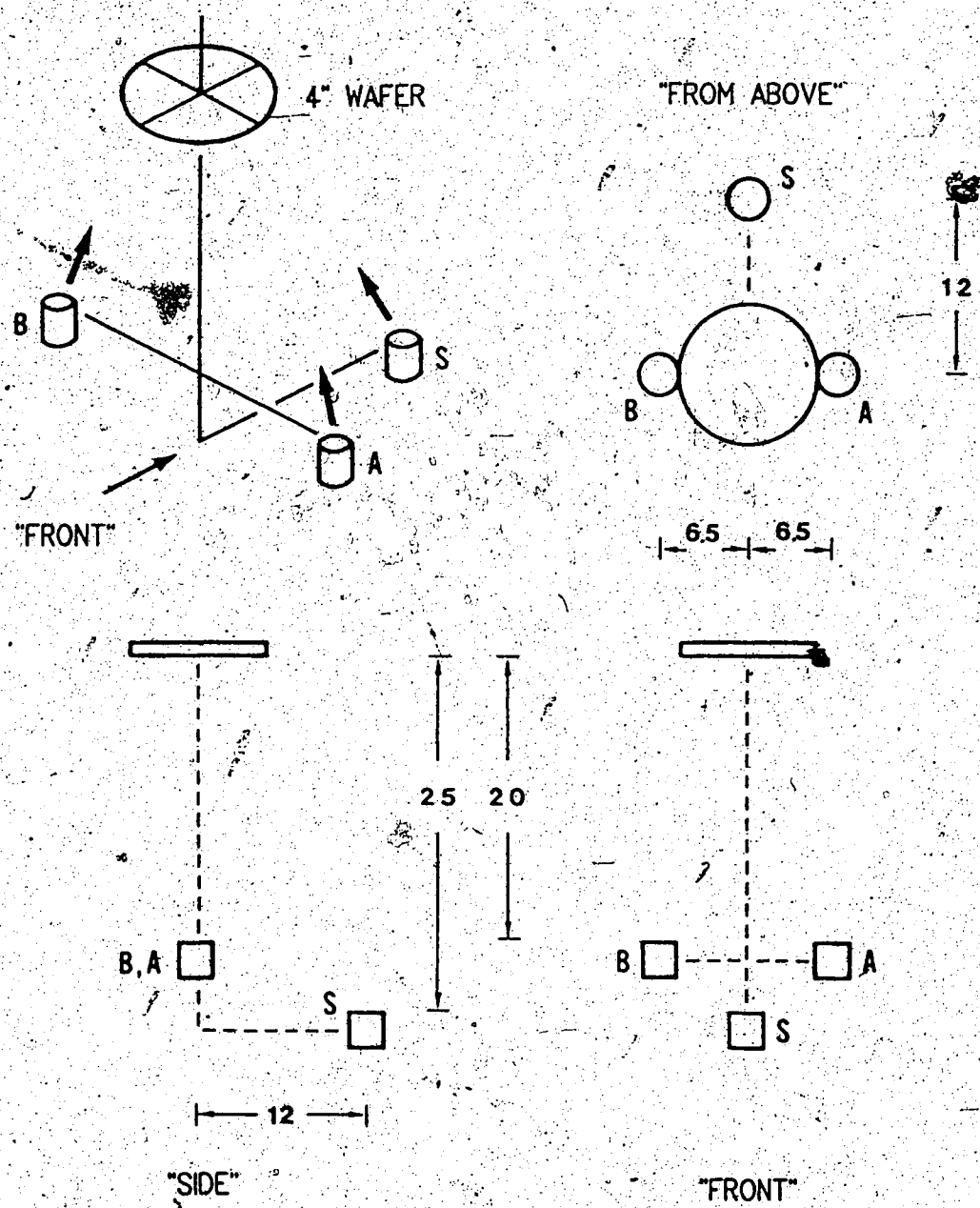


Fig. 2.2 Geometry of NRC MBE chamber. The relative position of each doping source with respect to the 4" substrate holder is shown. Dimensions are in cm. S - Silicon source. B - Boron doping source. A - Arsenic doping source.

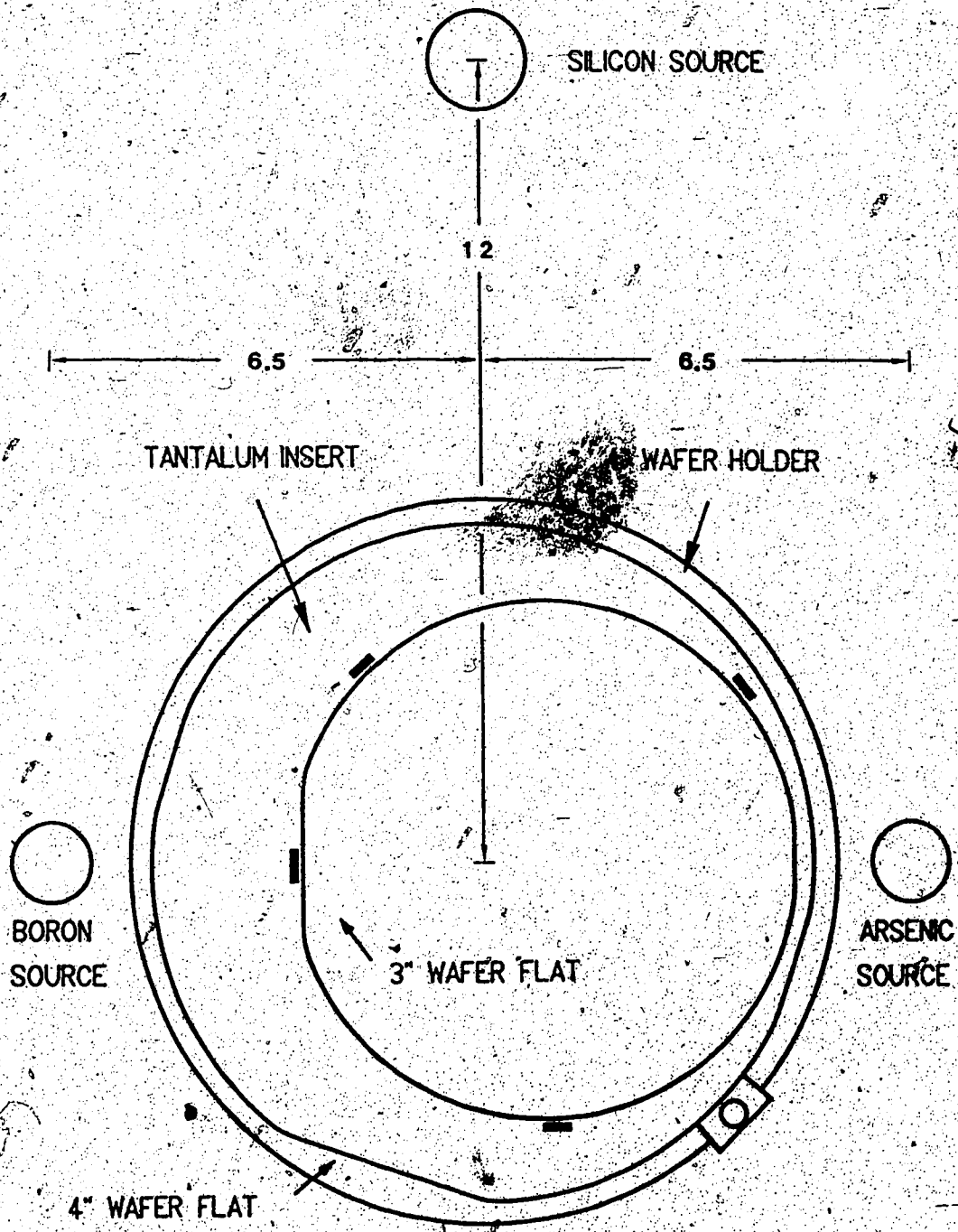


Fig. 2.3 MBE geometry indicating location of 3" substrate. View is from above looking down. Doping sources lie below the substrate. Dimensions are in cm.

the axis, there will be an additional offset due to the angle of the incident beam. However, there is a similar offset of the doping sources. By taking the offsets of all three source beams into account, the width of the intrinsic regions will vary from $110\mu\text{m}$ to $140\mu\text{m}$ across the 3" substrate.

There is also an offset in the other direction associated with the difference in angle between the silicon sources and the impurity sources (See Fig. 2.2, side view). Hence, the end of the mesa closest to the silicon source will not be doped. The width of this undoped region will be about $200\mu\text{m}$ on average.

The doping sources are not point sources but have a finite width of about 1-2 cm. The molecular beam that passes the shadow mask edge will not have a sharp cutoff but will decrease gradually resulting in a graded region of about $20\text{-}30\mu\text{m}$ wide. The interface between the doped and intrinsic regions will consist of a graded junction rather than an abrupt junction.

This is also true of the silicon source but in this case, it will result in a wider edge profile (step) for the mesa edge. Fig. 2.4a is a surface profile of the mesa edge for MBE 318. The $0.3\mu\text{m}$ mesa step is about $30\mu\text{m}$ wide and it is over this edge that the contact metal is to be placed. Although the silicon deposition drops off across this edge, the impurity deposition will remain constant resulting in highly doped silicon along the step. An idealized edge profile, as depicted in Fig. 2.4b, implies that the vertical edge of each superlattice layer may not be exposed to the contact metal. In the actual edge profile the impurities are expected to be distributed throughout all the layers as the mesa height drops off contact to each layer is expected to occur

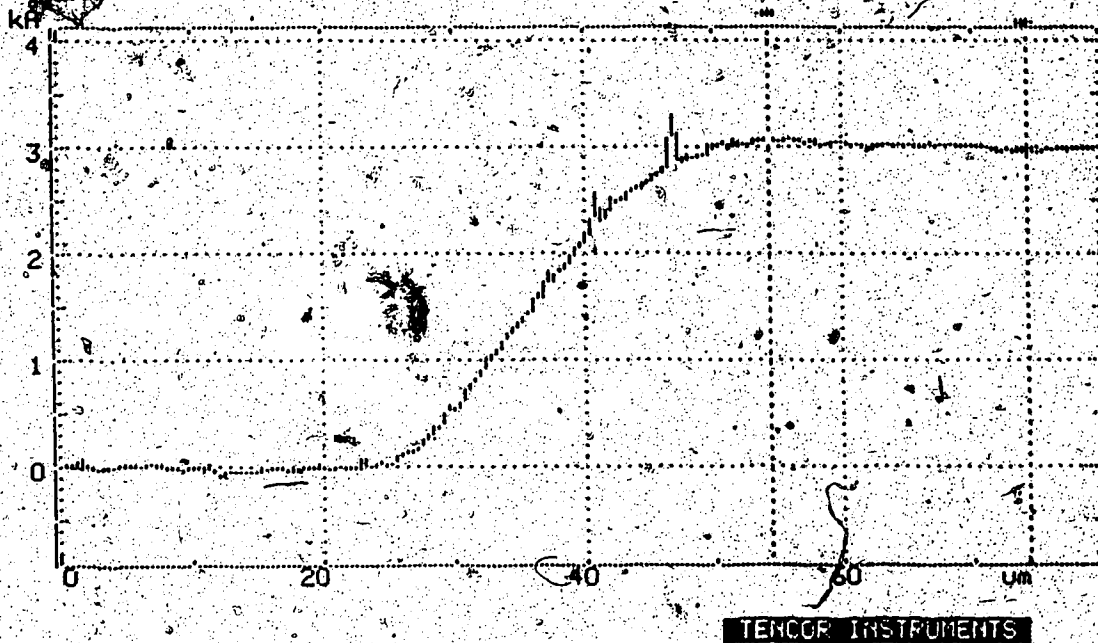


Fig. 2.4a. Surface profile of a mesa edge for MBE #318.

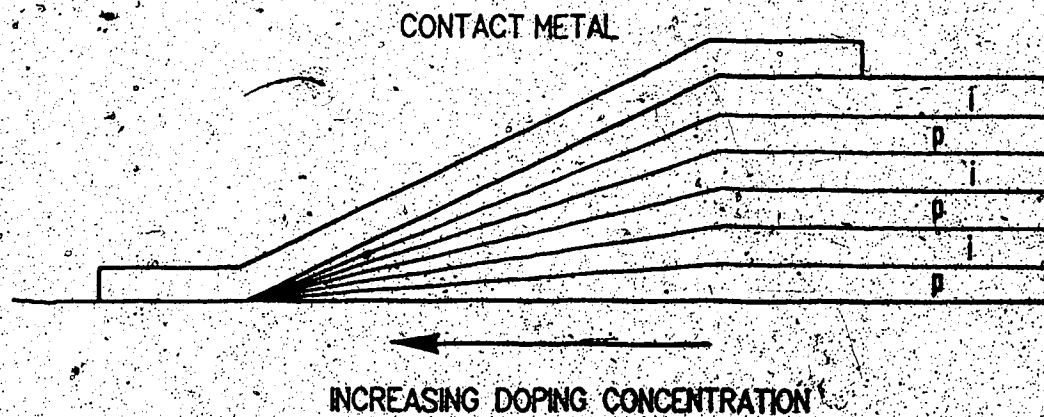


Fig. 2.4b. Idealized diagram of superlattices layers at the edge of the mesa. The doping concentration will increase as the layers get thinner near the edge. The mesa height is much smaller than the width of the sloping edge. (For the case of MBE 318, $0.3\mu\text{m}$ vs $30\mu\text{m}$)

as a result of annealing. On the left-hand side of Plate Ia (end of Chapter 2), the edge profile is shown (from above). The right-hand side of this mesa has undergone a selective chemical etch which allows the individual layers of the superlattice to be seen.

2.1.1 Shadow Mask and Contact Design

Two different mesa and shadow mask designs have been produced to date. The first shadow mask design was used in the fabrication of MBE 318 and MBE 321. A proper contact mask was not available for the mesas on this mask but a contact mask was improvised at the NRC using the shadow mask as a pattern. An example of a mesa with these contacts is shown in Plate IIc for MBE 318.

With the first contact arrangement, there is a great deal of surface area between the contact metal and the substrate. It was felt that the substrate effects were overwhelming the observation of any of the mesa results. Two steps were taken to improve this situation. First, substrates with a higher resistivity were purchased (7,000 Ω -cm, an increase of over three orders of magnitude.) Second, a new pattern mask set with an improved geometry was designed in order to reduce the surface area of substrate-metal contact by a factor of 10. The following is a description of the new mask pattern set.

There are four pattern masks required. The first is a full wafer pattern for the fabrication of the shadow mask. The remaining pattern masks are needed for the contact metal, for the metalization and bonding pads and to delineate the etching region for the notches in the split contacts. Another mask was also made to open windows in an oxide layer but it was not used in the processing.

The devices are grouped into "cells" of 8 mesas, placed close together with a wider separation between the cells in order to leave room to cleave the wafer for contact processing. The size of each cell is 1.2 cm by 0.8 cm with 26 cells on the wafer as shown in Fig. 2.5. There are four device sizes in each cell which have been placed symmetrically to allow the use of one mask for contacting both sides of the mesas. The designed length of each device is 1.45 mm and the designed widths are 0.35, 0.55, 0.75 and 0.95 mm. The actual sizes will depend on the silicon shadow mask window openings. Two of the devices have two contacts on each side of the mesa to allow separate electrical measurements of each layer type. A small mark in the corner of each cell will aid in identifying the n-type and p-type sides. Fig. 2.6a depicts the pattern for etching the shadow mask and the window openings that will result.

It is not possible to predict the final width of the windows in the silicon shadow mask because of the variation in the wafer thickness. In order to avoid this problem, the contact masks have been split into pairs in such a way that only one side of the mesa is aligned for patterning at a time. The contact mask design is thus independent of the shadow mask window width.

The pattern mask for the contacts is designed for one cell only since each cell will be processed separately. The mask will open a window on each device for the application of the contact metal on one side of each mesa. The same mask will be used for the contacting of the other side. The width of the contact metal is $50\mu\text{m}$. Since the average width of the mesa step is around $20\text{-}30\mu\text{m}$, this will allow the entire step to be covered (See Fig. 2.4b). The length of the contact

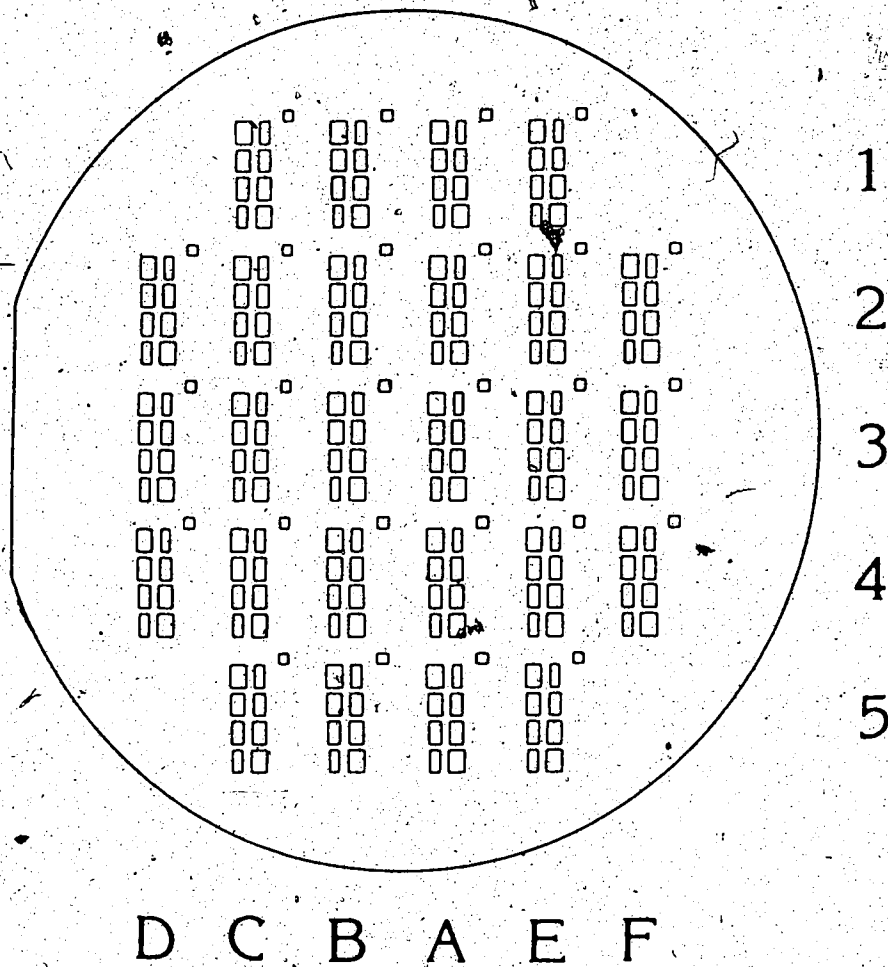
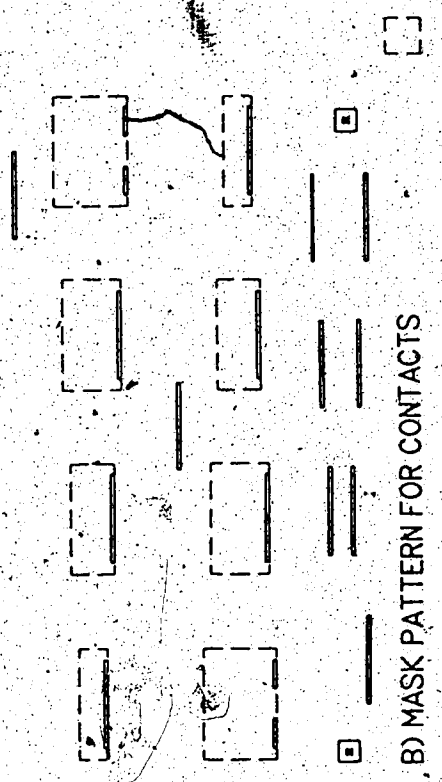
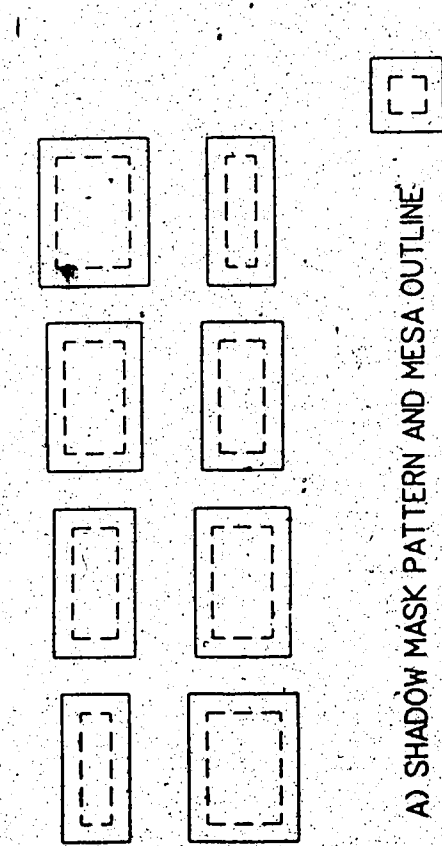


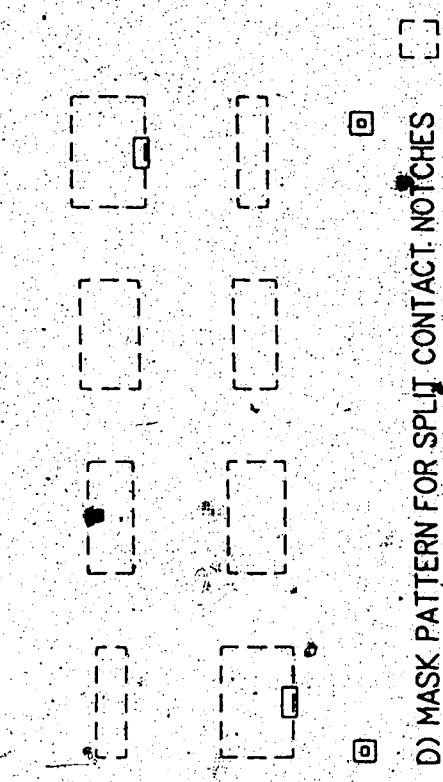
Fig. 2.5 Layout of shadow mask pattern.
 The wafer is divided into 26 cells of 8 mesas each.
 The numbers 1-5 and letters A-F are used in the text to refer to particular sample cells. Figure is drawn 1.5x actual size.



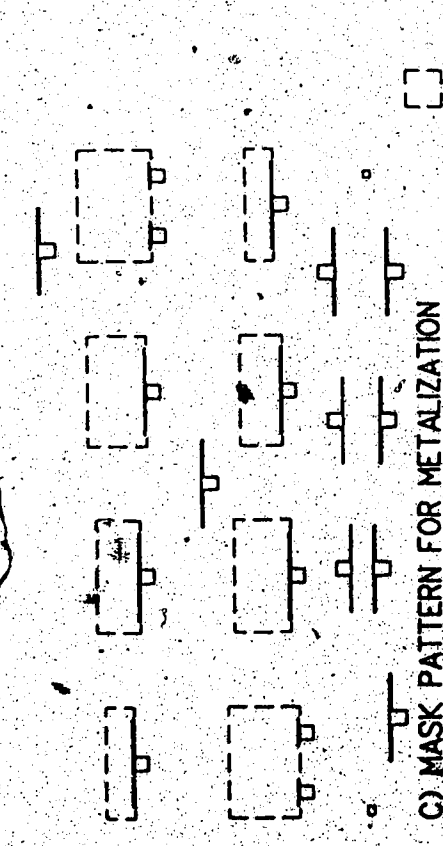
A) SHADOW MASK PATTERN AND MESA OUTLINE



B) MASK PATTERN FOR CONTACTS



C) MASK PATTERN FOR METALIZATION



D) MASK PATTERN FOR SPLIT CONTACT NOTCHES

Fig. 2.6 Mask pattern set for shadow mask and contact processing. Dashed lines represent mesa outline. Figure is drawn 10x actual size.

is 1.2mm which leaves about $100\mu\text{m}$ at each end of the device free. The split contacts are similar but with a $400\mu\text{m}$ break in the middle.

Fig. 2.6b shows the mesa outlines (dashed lines) along with the pattern for the p-side contacts. Also shown in the figure are nine contacts on the substrate. These are used to help characterize the contacts and are discussed later. The two small squares are registration marks used with the later pattern masks.

The metalization mask has also been split in order to accommodate variations in the window width. Since the metalization for both sides is processed at once, a double exposure of the photoresist is required. With a positive photoresist, it is possible to expose the metalization windows on one side, rotate and re-expose for the other side. The photoresist can then be developed leaving properly aligned windows on both sides of each mesa. The metalization consists of $30\mu\text{m}$ wide strips resting on the contact metal and bonding pads ($250\mu\text{m}$ square) as shown in Fig. 2.6c.

The procedure for etching the notches follows a similar processing technique as the metalization mask. A double exposure is used to delineate both sides of the mesa for etching. In some cases, multiple exposures were done, increasing the size of the notch to ensure the intrinsic regions were fully removed. (See Fig. 2.6d)

Since the mesas are quite visible, the mesa edges themselves are used for alignment of the contact mask. Registration marks are provided for aligning the other two masks. The mesa outlines along with the contacts for both sides of the mesa are shown in Fig. 2.7. The bonding pads for the p-side contacts have been marked in order to show the pairs of substrate contacts.

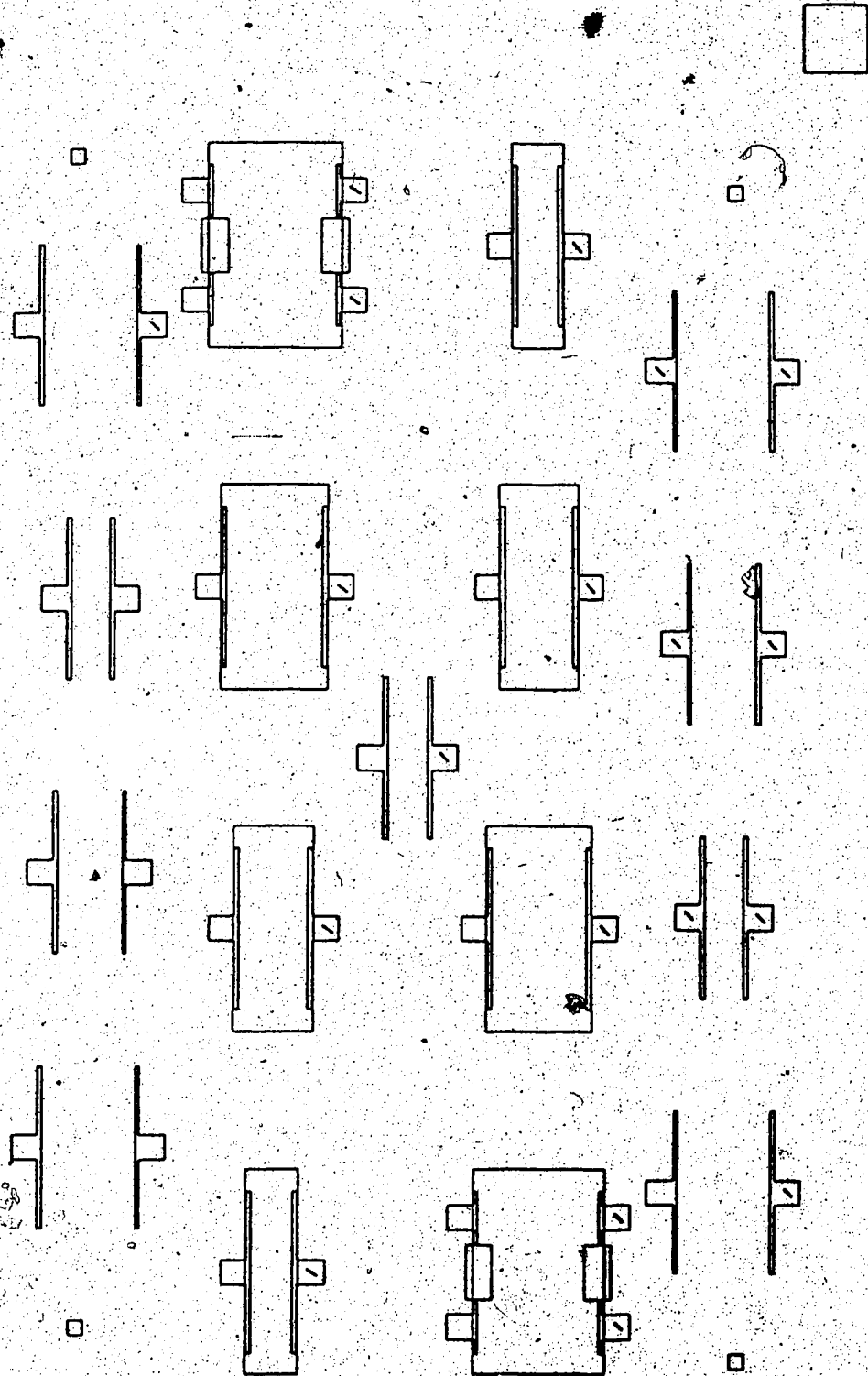


Fig. 2.7 Final arrangement of contacts. Shown for one group of mesas with both n-type and p-type contacts. The marked pads indicate the p-type contacts. The arrangement of the substrate pads is also shown. Figure is drawn 20x actual size.

2.2 Fabrication of the Shadow Mask

The shadow mask is made from a silicon wafer using an anisotropic chemical etch. There are several reasons for using a silicon wafer as the shadow mask. 1) Silicon remains rigid at the high temperatures required for MBE growth (860°C for the prebake). 2) Silicon will not contaminate the MBE chamber through outgassing, etc. 3) The thickness of a semiconductor wafer is approximately the same as that needed to produce the desired shadow (about 1/2 mm). 4) Chemical etching procedures for silicon are well known and can produce a very precise edge for the shadow mask. 5) Commercial silicon wafers are inexpensive.

The method chosen for the shadow mask preparation involved the simplest design and processing procedure possible. The etching is performed from the back side of the mask toward the front forming a V-shaped groove in the wafer. Only one photolithography pattern is required and hence no further alignment is needed. The procedure for silicon etching is described in the next section. The results obtained for etching the shadow mask are presented in Section 2.2.2.

2.2.1 Silicon Anisotropic Etching

With an anisotropic etch, the etch rate is dependent upon the crystal orientation. For the EDP etchant for example, the etch rate in the (100):(110):(111) directions is 50:30:3 $\mu\text{m/hr}$ [18]. If (100) silicon wafers are used with an appropriate etch mask, V-grooves can be formed in the surface due to the inhibited etch in the (111) direction as shown in Fig. 2.8. The angle of the groove will be given by $\tan \alpha = 2^{1/2}$ or $\alpha = 54.7^\circ$.

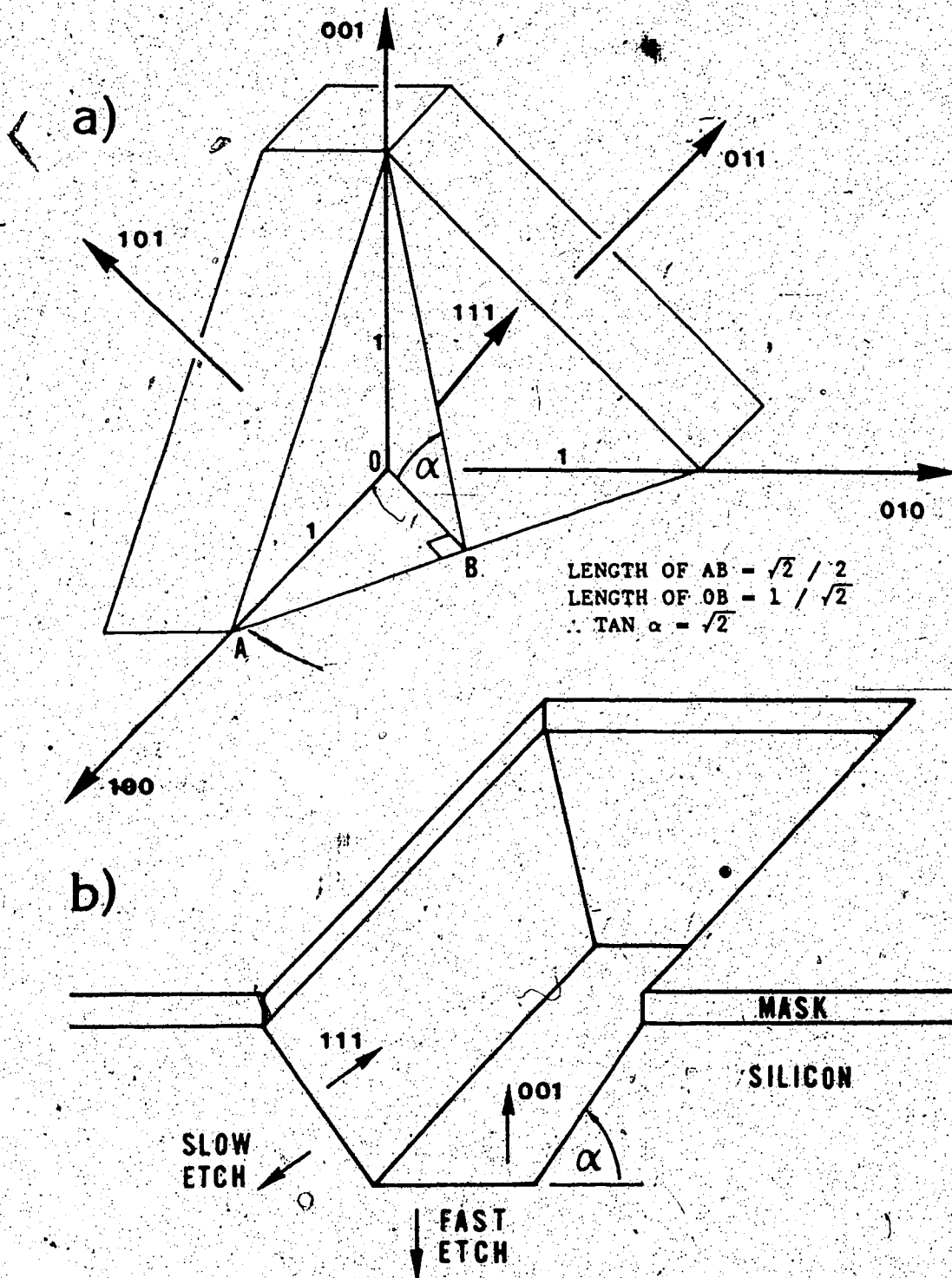


Fig. 2.8 Anisotropic etching of silicon
 a) Crystal planes of silicon showing relationship between (111) plane and the angle α .
 b) Diagram of a partial silicon etch. If left to etch longer, the flat bottom would be etched away leaving a V-shaped groove.

There are many known anisotropic chemical etchants for silicon. These generally consist of a strong alkaline solution which is used at elevated temperatures. All of the etchants investigated etch fastest in the (100) direction and slowest in the (111) direction. The ratio of the fastest to slowest etching rates (degree of selectivity) in these directions is roughly the same for most of the etchants, about 17 to 1. The main types of anisotropic etchants for silicon are given here (grouped by their main ingredients) along with some of their characteristics [18]:

Potassium Hydroxide solutions (KOH)

Advantages include a fast etch rate (about 60 $\mu\text{m/hr}$), relatively safe, and convenient to work with. Their main disadvantage is the rapid etching of the oxide etch mask.

Solutions containing hydrazine.

Since hydrazine is extremely volatile, these solutions were not considered for this work because of safety reasons. Their advantages include a very fast etch rate.

Ethylenediamine-Pyrocatechol (EDP)

This is a popular silicon etch consisting of ethylenediamine, pyrocatechol and water. It is relatively safe, easy to work with, does not explode and is easy to clean up. Advantages include a fast silicon etch rate and a slow etch of SiO_2 masks.

Tetramethylammonium hydroxide

Advantages include alkali free etching which was not a concern in the shadow mask processing. The etch rate is slow (22 $\mu\text{m/hr}$).

Ammonium fluoride

This etchant also has a slow etch rate.

In order to pattern the wafer for etching, some sort of mask is required that will withstand the etching solutions. The silicon anisotropic etchants are all strong caustic solutions which means that an organic mask will be quickly destroyed. This is especially true at higher temperatures. The most practical mask available is SiO_2 . An oxide layer is easy to grow, may be patterned using standard lithography and provides suitable etch resistance. For EDP, the etch rate for SiO_2 was found to be about 200Å per hour. The etch rate of the oxide mask with the KOH solutions was found to be quite fast, about 1000Å per hour. Etching a 400µm wafer with KOH at 50 µm/hr would require a SiO_2 mask of at least 0.8µm thick.

The KOH solutions were tried first and the etch results were very good but because of the fast etch of the oxide mask, it was not used further. The EDP solution had excellent etching qualities and the oxide mask stood up well. This solution was chosen for all further etching and good results were obtained in the fabrication of the shadow masks. The last two etchants were not tried since the EDP results were adequate.

The oxide was thermally grown in an air environment with a Lindberg furnace that was normally used for baking ceramics. Since an oxide layer was required on both sides of the wafer, they were supported on-edge in the furnace. In this way, only a small portion of the wafer edge was protected from the air. Up to three wafers could be processed at once and about 40 wafers in all were coated this way. The wafers were baked at 1100°C for 16 hours which produced an oxide layer of about 5000Å thick.

Several factors affected the quality of the oxide. Any specks of dust or dirt that were on the wafer when it was heated would result in pinholes in the oxide. The furnace itself was quite dirty, during baking a black carbon-like dust would fall on the wafers which also resulted in pinholes forming in the oxide. This effect worsened as the temperature was increased but if the oven was "cycled" while empty at high temperature previous to oxide growth, the problem was reduced. The oxide layer sometimes developed cloudy patches which felt rough to the touch. In general, these regions did not affect the quality of the oxide as a mask although they did appear to contain more pinholes. There was a temperature gradient inside the furnace which resulted in a variation in the oxide thickness of up to 600Å. The amount of available fresh air also affected the rate of oxide growth. The portions of the wafer where the air flow was restricted had a thinner oxide layer. By making the overall oxide thick enough, any problems due to variation in oxide thickness were avoided.

The quality of the oxide grown by this method is probably quite poor. However for the purpose of providing a protective layer for silicon etching it does an excellent job. The ability of the oxide to hold photoresist, its etching characteristics (in buffered HF acid) and its masking characteristics in the etchant were excellent. The only problem encountered was with pinholes.

The procedure for silicon etching with the EDP solution is very straightforward. The following is a summary of the etching setup and method. The EDP solution was placed in a two litre beaker filling it about 1/3 full. A hotplate with magnetic stir bar was used for heating and agitation. The hotplate was connected to a temperature controller

with a sensor placed in the EDP solution. A temperature of 105°C was maintained during etching.

References on EDP etching recommend using a reflux arrangement [18,19]. For the shadow mask etching, an oversize watchglass on top of the beaker was found to suffice. The air flow in the fume hood actually cooled the watchglass quite well and the evaporated solution condensed and dripped back into the beaker. Although some of the solution was probably lost, it could be used many times without a noticeable decrease in strength. Water was found to be quite adequate for cleaning. A white froth-like residue sometimes formed on the etched wafer after it was removed from the EDP. A very thorough rinsing in water is required after etching in order to prevent this crust from forming.

The etch rate is greatly effected by agitation of the solution. The oxidation process involved in the silicon etching creates bubbles which adhere to the wafer; the etch is inhibited under the bubble until it is blown away. A stir bar was used for agitation of the solution but some care is required to prevent the accidental breakage of the mask. Since the etch is along crystal planes, the wafer is severely weakened by the etching and quite susceptible to cracking.

The time taken to etch completely through the wafers is about 6 hours. The wafer needed to be left in the solution for at least 1/2 hour after the first holes appeared in order to clean out all the corners. The etching took place at a remarkably even pace across the wafer. The variation in etch times was due to factors such as strength of solution, agitation rate, and temperature.

Different wafer holders were used with mixed success. Plastic and

teflon holders were tried but because of the high temperatures, they softened and became more flexible and the wafers often dropped out of them. Various metal holders were tried but they contaminated the EDP solution causing the etching rate to drop. A good holder was made of glass rod which held the wafer securely. The holder rested against one wall of the beaker providing room for the stir bar in the center of the beaker.

2.2.2 Shadow Mask Results

The shadow masks were fabricated from 3" n-type silicon wafers with (100) orientation. The average wafer thickness was $375\mu\text{m}$ which will result in an edge undercut of about $265\mu\text{m}$ on each side of the opening. The final width of the window opening will depend on wafer thickness. Since the wafers used vary in thickness by $\pm 25\mu\text{m}$, this can result in a substantial variation in the window width of up to $\pm 40\mu\text{m}$. The thickness variation across a single wafer is small and no variation in window width across a wafer was observed.

The oxide mask will also be undercut to some extent which will widen the window due to etching in the (111) directions. An oxide lip could be viewed on the shadow masks after etching and before the oxide removal and was found to be about $8\mu\text{m}$ in width. Measurements of the width of the step (horizontal displacement of top and bottom edge) when compared with the expected values also indicated an undercut of $8\mu\text{m}$. An etch of $8\mu\text{m}$ along the wafer surface indicates an etch of $8\mu\text{m} / \sin \alpha = 10\mu\text{m}$ in the (111) direction in the time it takes to etch through the wafer. The ratio of the (100) to (111) etch rate is found to be about 40:3. This is much higher than the ratio of 50:3 often

cited in the literature although on n-type silicon, etch ratios as high as 40:1 have been noted [19].

The orientation of the photoresist pattern on the wafer is critical as the etch will follow crystal planes and not the edge patterns of the mask. Normal mask-aligners have some orientation control but not to the extent needed here. Even the wafer flats were found to be slightly rounded which made alignment difficult. Great care had to be taken to ensure that the best possible alignment (much less than one degree off-axis). Successful alignment was obtained in the majority of the wafers processed.

Plate 1b is an SEM photograph of the window in the shadow mask for the small alignment tag. The shadow mask is viewed from the patterned side. The smaller window on the opposite side of the wafer will provide the shadow mask edges. The properties of the anisotropic etch are evident with the (111) planes and their intersections clearly shown. This photograph is typical of the quality of the shadow mask windows produced.

Plate 1c is a detail of the bottom lip of an etched shadow mask. It is this edge that will produce the actual shadow edge for mesa growth. Although the oxide mask on the opposite side of the wafer first determines the location of this edge, the final edge quality is affected by six hours of etching along a $500\mu\text{m}$ plane. Crystal imperfections, impurities, variation in agitation and etchant all take their toll resulting in a slightly degraded edge as shown in Plate 1c. These effects can be seen in Plate 1e where a polarizer has been used to bring out some of the detail. The edge variation which is on the order of microns is still much smaller than the required tolerances of

the shadow edge. As noted earlier, the physical width of the doping sources and silicon source will result in graded regions of about $20\mu\text{m}$.

The major contributing factor of flaws in the shadow mask windows was the oxide quality. The small pinholes in the oxide would result in the etch propagating along new crystal planes, widening the intended window. Furthermore, pinholes on both sides of the wafer contribute to these faults. Plate Id shows a serious flaw which was caused by a pinhole (or several pinholes) near the edge of the oxide pattern. The two small planes which extend from the top to the bottom of the wafer lie in the (110) planes. If left to etch longer, the new edge that has been formed would continue to enlarge until the (111) planes at each end of the mesa were reached resulting in a window with a wider width.

In the same SEM photograph, a small inverted pyramid that has resulted from a pinhole may also be seen. The size of the rectangle is determined by the extent of the original pinhole in the (110) directions. Pinholes in the oxide that lie far from the pattern edge (either inside or outside) will not affect the edge quality. Plate If shows two cells with the window openings for the mesas and the orientation tag.

2.3 Superlattice Fabrication

The second stage of nipi fabrication is the MBE growth of the superlattice layers. Two factors make this technique different from normal MBE growth. The substrate is not rotating and the shadow mask shields the substrate from the heating sources in the chamber. Details of MBE growth and results for the layers grown are presented in this section.

All samples were grown in a V.G. Semicon V80 Silicon MBE machine at the NRC. The doping source for the p-type layers is a Knudsen cell with boron oxide in a silicon nitride crucible. A V.G. Semicon IBD-100 ion beam doper is used to produce 500eV As⁺ ions for the n-type doping.

An e-beam evaporator provides the silicon source. Although the loading system on the MBE machine is set up for 4" wafers, the tantalum insert described earlier allowed 3" wafers to be used with the standard loading mechanism.

The shadow mask and the substrate are placed one on top of the other in the holder. Three small tabs are used to hold the two wafers in position. During two of the growth runs, the shadow mask and the substrate fused together. The shadow mask broke either during cooling or in attempting to detach it. The problem was subsequently avoided by placing small tantalum shims 10 μ m thick between the shadow mask and the wafer.

The substrates were first given a 50 minute ultra-violet ozone treatment to remove carbon contamination before placement in the vacuum system. Any surface oxide is removed with a high temperature bake at 860 $^{\circ}$ C for 5 minutes. An additional 5 minute bake with a slow silicon flux is used to "tickle" the remaining SiO₂ from the surface leaving an extremely clean surface for epitaxial growth.

The substrate temperature is then lowered to the temperature used for growth, typically 650 $^{\circ}$ C to 700 $^{\circ}$ C. With the shutters closed, the K-cell is raised to the desired temperature. Next a thin layer of silicon is grown on the surface (about 700 \AA). At this time the computer program is started to control the shutter operation of the doping sources to grow the superlattice. The base pressure in the MBE

chamber was typically 3×10^{-9} torr with a pressure of 5×10^{-8} torr during growth. The deposition rate was about 180Å per minute.

Some of the wafers have a rough surface which resembles "orange peel." This is shown in Plate IIA and in more detail in an SEM photograph in Plate IIB for MBE 360. Since the mesa is only $1.5 \mu\text{m}$ thick, it appears that the damage may be right through the mesa to the substrate. In the case of MBE 360, the damage is only on the edge of some of the mesas, but with others such as MBE 368, the damage covers the entire surface.

With the shadow mask in place, the substrate is hidden from the heating source by the mask and will probably be at a lower temperature than normally expected. However, it is not possible to determine the actual substrate temperature when the shadow mask is used. It may be that the temperature of the substrate is too low to support the usual processes, either during the cleaning steps or during growth. Whether or not this is the cause of the rough regions has not been determined as yet.

Normally the substrate is rotated during MBE growth. With the shadow mask method however, the substrate must remain stationary in order to make use of the chamber geometry. The direction of the silicon and doping beams have been optimized to provide even growth when the substrate is being rotated. Hence the molecular beams are expected to have a higher deposition rate near the outside edge of the wafer. The thickness of the mesas and their doping profiles will then vary across the wafer. In order to have reliable information as to how these vary, measurements of thickness (using a surface profiler) and doping (4-point probe method) were made for non-rotating substrates.

The results for the boron and arsenic doping distributions are given in Figs. 2.9a and 2.9b. The variation in thickness for MBE 360 is summarized in Fig. 2.10.

The doping profiles for two MBE 360 samples were determined by SIMS (Secondary Ion Mass Spectroscopy) analysis by T.E. Jackman (NRC) and J.A. Jackman (CANMET). The boron and arsenic distribution for MBE 360 #5B is shown in Fig. 2.11 where the y-axis represents the mesa surface. (Different log scales are used for the two impurities.) The concentration accuracy is $\pm 10\%$. The expected SIMS rolloff is one decade per 200Å. This is about the same as the drop-off on the right hand side of the peaks so the doping profiles may be sharper than what is shown here. The width of one period is 240Å which agrees favorably with the expected increase in thickness for this sample as shown in Fig. 2.10.

The boron profile is shifted by about $1/4$ of a layer thickness from the expected position of half-way between the arsenic peaks. This offset is also evident in the SIMS depth profile of MBE 360 #1C shown in Fig. 2.12. In this case, the beam conditions were chosen to allow simultaneous detection of both impurities and so the offset cannot be attributed to the measurement method. Possible causes of the offset include the implantation of arsenic ions and residual boron doping after the K-cell shutter has closed due to a rich boron layer at the growing silicon surface [20].

The offset will result in impurity compensation, especially in the case when the maximum doping concentrations are not equal. The fabrication of nipi's with layers less than 200Å may not be possible until the offset condition has been resolved. The most recent samples

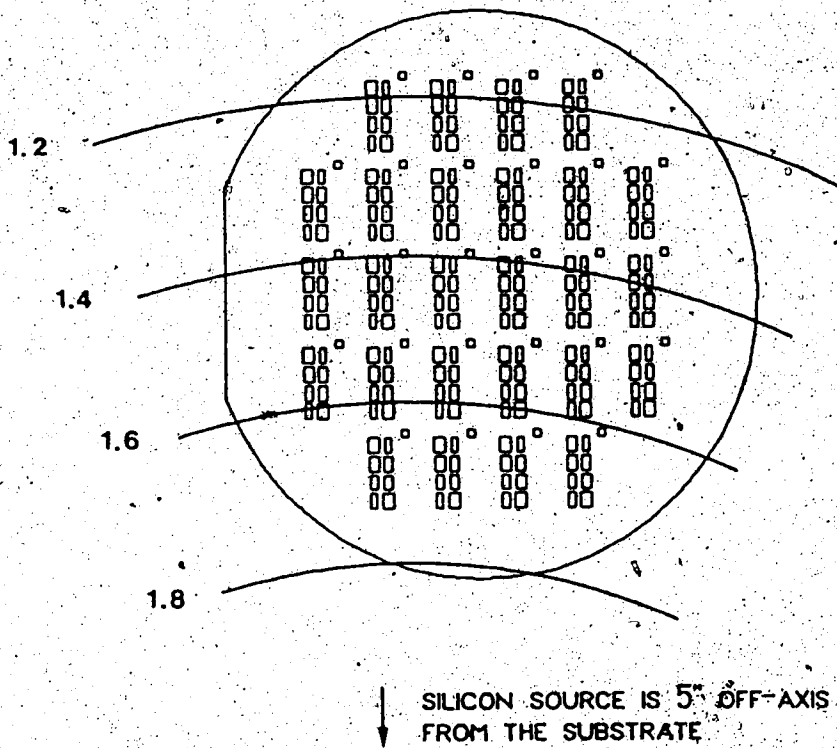


Fig. 2.10 Variation in silicon thickness across 3" wafer.
Numbers indicate thickness of mesas from MBE 360 in microns.

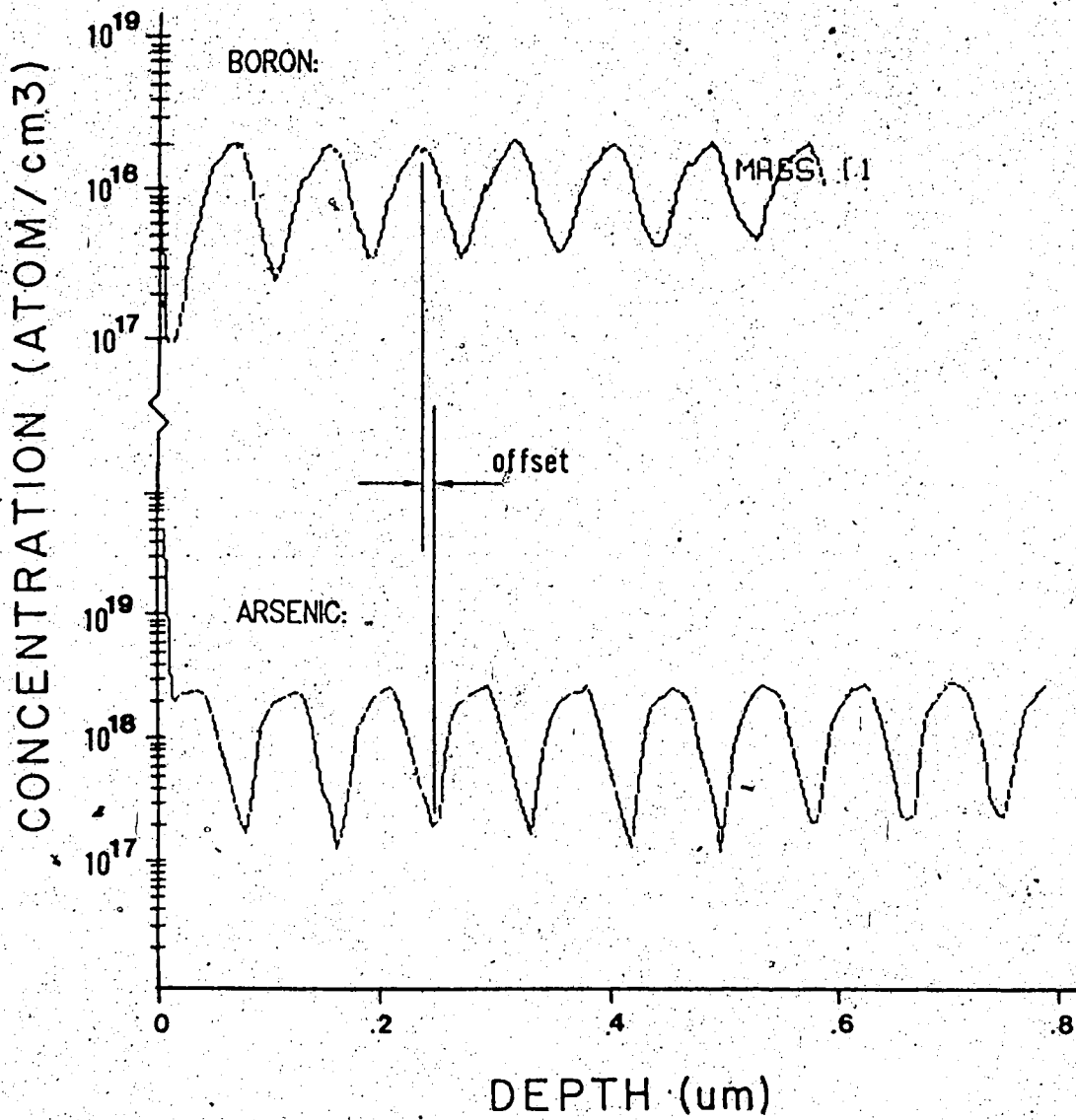


Fig. 2.11. SIMS analysis of doping concentrations in MBE 360 #5B.
Depth is measured from mesa surface.

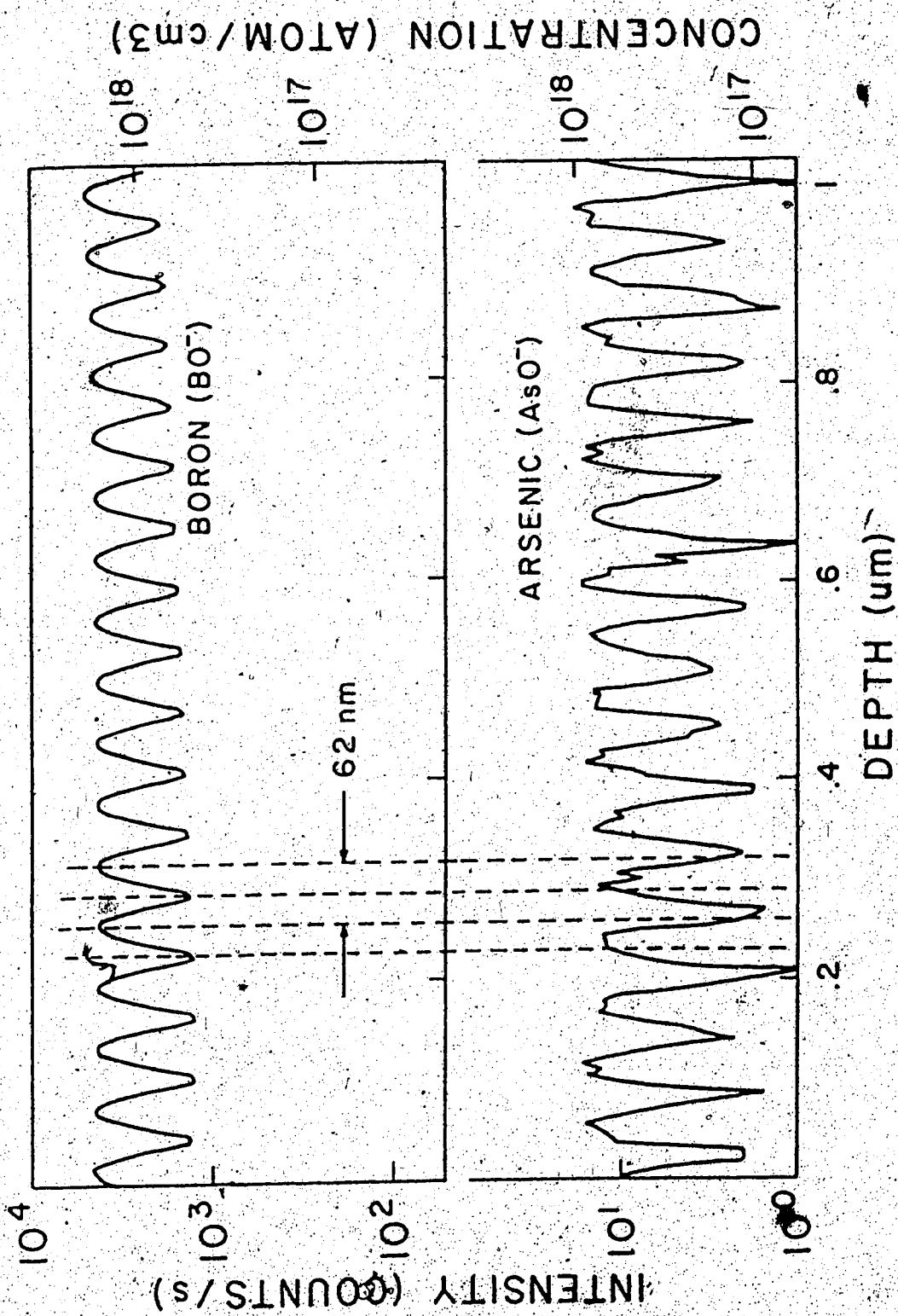


Fig. 2.12 SIMS analysis of doping concentrations in MBE 360 #1C. Depth is measured from mesa surface.

(MBE 404 and 405) were grown with 100Å intrinsic layers between each doped layer to reduce the compensation.

When plotted on a linear scale, the peaks of the impurity concentrations exhibit a sinusoidal behavior while the troughs appear to be linear. When the total doping ($N_a - N_d$) is considered, the doping profile will be determined by the shape of the peaks and the doping concentrations for the nipi's may be modelled with a sinusoidal approximation. Doping concentrations for other mesas may be estimated from these SIMS results and Fig. 2.9 for the doping variation across the wafer.

Table 2.1 summarizes the parameters for the MBE samples processed to date. The first two samples, MBE 318 and 321 were grown with the first mask design on Czochralski (CZ) substrates. The rest of the samples have used the new mask design and all except MBE 405 have used floating zone (FZ) substrates. The majority of the processing and testing has been done with MBE 360. MBE 368 was grown with thin layers but because of the extent of the surface roughness, it has undergone very little electrical testing. The next sample grown, MBE 391 was designed with wider layers but for some reason, there is very poor definition in the doping of the layers (from SIMS analysis). Electrical characteristics for this sample also show very poor diode behavior. The last two samples were processed together on different substrates in order to help investigate some of the substrate effects. Few processed nipi's were available from these samples at the time of writing.

MBE Sample #

	318	321	360	368	391	404	405
Substrate Type	CZ	CZ	FZ	FZ	FZ	FZ	CZ
# of Periods	20	20	20	20	20	10	10
d_n (Å)	50	350	350	120	550	700	700
d_p (Å)	50	350	350	120	550	700	700
N_d ($\times 10^{18} \text{ cm}^{-3}$)	30	4	4	10	4	4	4
N_a ($\times 10^{18} \text{ cm}^{-3}$)	30	4	4	10	4	4	4
Silicon cap* (Å)	1000	1000	0	0	0	0	0
d_i (Å)	0	0	0	0	0	100	100
Thickness (μm)	0.3	1.5	1.4	0.48	2.2	1.6	1.6

* A cap of undoped silicon was grown on the first two samples.

Table 2.1 Summary of MBE Growth Runs

2.4 Contact Fabrication

After MBE growth of the mesas, the next stage in the nipi² fabrication is the processing of the contacts. The steps involved, including growth of an oxide layer, lithography, metal deposition and processing are outlined here. As well, the plasma etching of the notch and the chemical etching of the substrate are described. Some observations of the physical appearance for the various contacts are also given but the electrical characteristics of the contact metals are discussed later in Chapter 3.

Oxide Layer

In order to provide a mask for contact processing and a protective layer between the bonding pads and the silicon substrate, a 5000Å thick layer of SiO₂ was sputtered onto the wafer immediately after MBE. Windows were opened in the oxide for the contacts by using the appropriate pattern mask and a buffered oxide etch.

Platinum Silicide

Platinum silicide is used for the p-side contact. After the oxide windows had been opened and the photoresist stripped, the samples were taken to Carleton University for platinum sputtering. A 60 second back-sputter was performed as a final cleaning to remove any oxide, followed by the deposition of 500Å of platinum. The samples were then baked for 30 minutes at 500°C to form PtSi. The platinum silicide will only form in the oxide windows where the platinum is in contact with the silicon and the remaining platinum is stripped in aqua regia.

The platinum silicide contacts have a smooth uniform metallic appearance as shown in Plate IIc (top contact) and Plate IIId (bottom

contact, shown with metalization). The contacts also adhered well. No major problems were encountered in processing these contacts.

Magnesium

Magnesium has been used for the n-side contacts. The windows are opened in the oxide but the photoresist is not stripped since it is required for the lift off process. A 3000Å layer of magnesium is deposited using thermal evaporation followed by a layer of aluminum to prevent oxidation of the magnesium. A lift off process is used to strip unwanted Mg-Al. The contacts are then annealed in a rapid thermal anneal (RTA) oven at 300°C for 10 minutes.

The Mg contacts have a very uneven physical appearance. In some places the magnesium appears to have peeled off the silicon. After annealing, some parts of the contact became dark as if it oxidized. These features can be seen to some extent on the bottom contacts of Plate IIc and Plate IIe. The insert of Plate IId shows a magnesium contact on a mesa edge before annealing. The problems with magnesium prompted the search for an alternate n-side contact metal.

Gold-Antimony

The recent samples have gold-antimony as the n-side contact. A lift off process is also used for these contacts. After the evaporation of 800Å of gold (with a 1% antimony composition), the contacts are annealed using a rapid thermal anneal at 400°C for 30 seconds. There have been problems with these contacts as well. In many cases they have not adhered at all and peeled off the silicon. The contacts are also very sensitive to annealing; some contacts have been destroyed by annealing too long resulting in an open circuit to the substrate.

Metalization

The metalization pattern is made up of $30\mu\text{m}$ wide strips placed directly on the $50\mu\text{m}$ wide contacts as well as $250\mu\text{m}$ square bonding pads which lie on the oxide. The metalization consists of a 300\AA layer of titanium followed by a 550\AA layer of platinum and topped off with a 3800\AA layer of gold. These were deposited by evaporation and processed using lift-off lithography. No major problems have been encountered in the metalization process. The metalization on the contact can be seen in Plate II d and the bonding pads are shown for the split contact mesa in Plate II e.

Plasma Etch of the Mesas

The notches for the split contacts were made by plasma etching. Windows were opened in the oxide once more and the samples were etched for six minutes forming a notch $2.5\mu\text{m}$ deep. Since the mesas are $1.5\mu\text{m}$ high (MBE 360), the mesa has been completely etched away in the notch region as desired. The rate of the plasma etch depends to some extent on doping. The transition from the p-i-p-i to the p-n-p-n regions is visible in the notched region which provides an excellent indication of whether the notch is wide enough. This is partially visible in the top notch in Plate II e.

The silicon and doping sources in the MBE chamber are also offset in a second direction which results in one end of the mesa being shadowed from both the n and p impurity beams. In the recent samples, these undoped portions of the mesas have also been removed by the plasma etch.

Chemical Etch of Substrate

The substrate surface has also been etched before making the

contacts on the more recent samples to remove the residual doping impurities from the substrate surrounding the mesa. This was done to improve the diode behavior of the metal-substrate interface. The effect of this etch is discussed in Chapter 4. An eight second chemical etch ($\text{HF}:\text{HNO}_3:\text{CH}_3\text{COOH}$) is used to remove approximately $0.1-0.2\mu\text{m}$ of the substrate. The etch rate is dependent on doping concentrations and produces a visible outline of the doping impurities as shown in Plate IIf. The silicon mesa, along with the outline of the boron and arsenic deposition are visible demonstrating the effect of the shadow mask. The widths of the intrinsic regions agree with what was expected. The end-region of the mesa with no doping is also apparent in this photograph.

CAPTIONS FOR PLATE I

Ia Mesa edge and superlattice layers.

The portion of the mesa on the right side of the photograph has undergone a chemical etch exposing the individual layers of the superlattice. The mesa is on the top of the photograph.

Ib Window opening in the silicon shadow mask.

Shown here is the small tag used for orientation. The etched surfaces lie in the (111) planes.

Ic Detail of an etched edge of the shadow mask.

This is the bottom edge of the wafer which is used as the shadow edge. The small variation shown will have no effect on the nipi quality.

Id Shadow mask with a major fault along one edge.

The two smaller planes lie in the (110) planes. The small pit close to the right side is due to an oxide pinhole.

Ie Sloping faces and window opening of the shadow mask.

Mask opening viewed straight on, three of the sloping faces of the window opening can be seen. Center portion of the photograph is the window opening. The dark corners are due to microscope lighting. A polarizer has been used to enhance the variations in the etch.

If Portion of shadow mask showing windows for two cells.

Placing the mesas closer together would make the shadow mask very fragile.

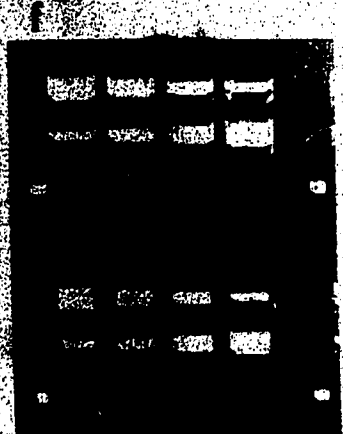
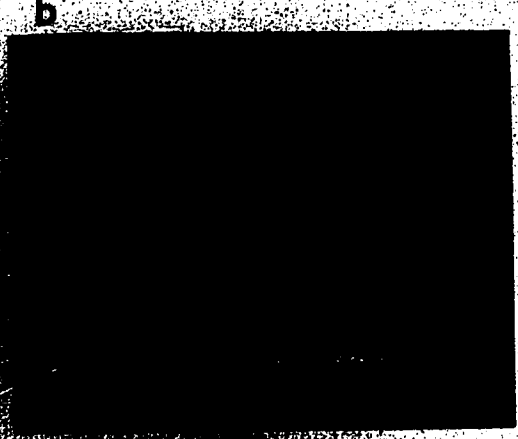
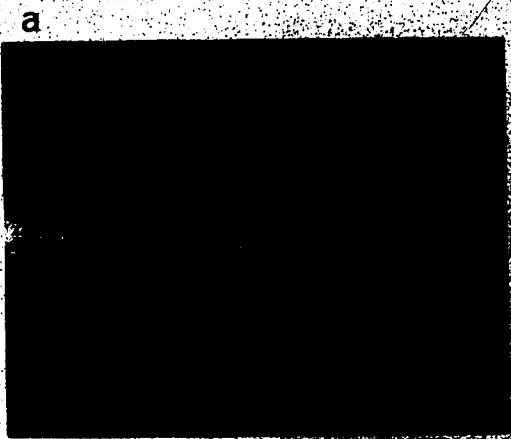


PLATE I

CAPTIONS FOR PLATE II

IIa Corner of a mesa from MBE 360.

The rough portions are evident on the edge of the mesa.

IIb Detail of the rough MBE growth from MBE 360.

Since the mesa is less than $2 \mu\text{m}$ thick, the damage may be through the entire superlattice depth.

IIc Mesa with contacts produced with the first mask.

The top contact is PtSi and the bottom contact is magnesium. The mesa is $10 \mu\text{m}$ wide.

IIId Corner of a mesa and with a PtSi contact.

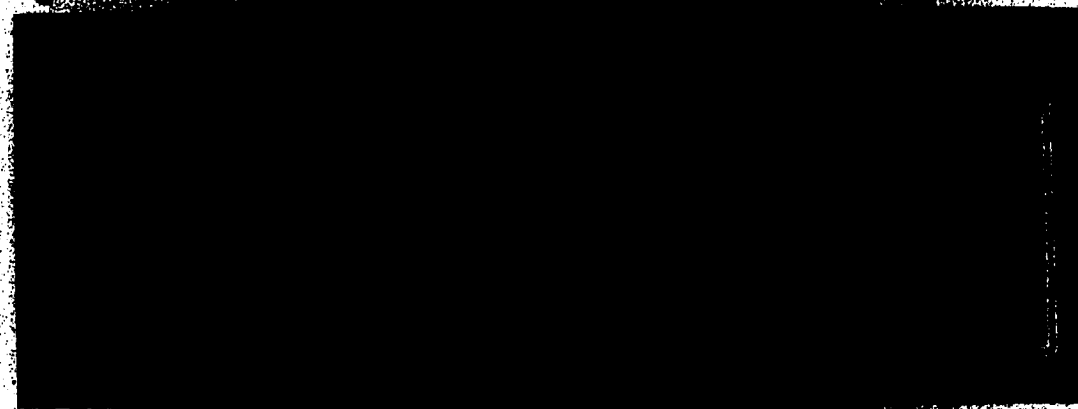
This contact was produced with the second mask set. The gold metalization ($30 \mu\text{m}$ wide) can be seen in the central region of the contact ($50 \mu\text{m}$ wide). The placement of the contact across the mesa step is evident. The inset in the upper right hand corner shows a typical magnesium contact (also $50 \mu\text{m}$ wide).

IIe Split contact mesa.

The position of the split contacts and the plasma-etched notches are shown. On later samples, the notches were cut further into the nipi. The top contacts are PtSi and the bottom contacts are magnesium.

IIIf Mesa and substrate after surface etch.

The outline of the regions of arsenic and boron deposition can be seen on the substrate. The mesa was not etched.



2

9

Chapter 3

Contact Characteristics

The fabrication of selective metal-semiconductor (M-S) contacts is crucial for the successful operation of nipi's. Although the use of the shadow mask has greatly reduced the selectivity requirements, the contacts must still exhibit some degree of selectivity. For example, on the p-side of the mesa, the metal is expected to provide an ohmic contact with the boron-doped layers while maintaining a rectifying barrier to the intrinsic layers. As well, because of the large contact area and the contact placement on the edge of the mesa, a highly rectifying behavior with the substrate is required.

In this chapter, the electrical characteristics of the n-side and p-side contacts are investigated. Although contact behavior was not originally intended to be part of this thesis, the problems encountered with the large reverse bias leakage currents found in the nipi's has made this study necessary. In order to present the results in a clear manner, an introduction to the theory of M-S junctions and the measurement methods used is outlined in Section 3.1. A summary of some of the complications encountered is given in Section 3.2. The remaining two sections discuss the results for the p-side contacts and n-side contacts.

3.1 Metal-Semiconductor Contacts

A common approach to the theory of current transport in M-S junctions is due to Schottky [21]. This model, which is based on the carrier diffusion across the junction, is described in many references such as Muller and Kamins [22] and Sze [23]. The relevant equations

have been summarized in Appendix A. All future references to Schottky theory are from Sze unless referenced otherwise.

The M-S junction is characterized by a potential barrier height $q\phi_{Bn}$ between the lowest empty states of the metal and the lowest conduction band states of the semiconductor. (See Fig. 3.1 for a typical energy level diagram.) Normally, the barrier is expected to depend on the difference between the work function of the metal and the electron affinity of the semiconductor. However, for some semiconductors, including silicon, the barrier height is found to depend on another factor. The effects of the surface state density may be significant enough to pin the Fermi level at the semiconductor surface and hence fix the barrier height. For silicon, this is typically true with barrier heights of around $2/3 E_g$ [22]. The relationship, $E_g = q(\phi_{Bn} + \phi_{Bp})$ implies that on p-type silicon, the barrier heights will generally be quite low ($1/3 E_g$) which makes the fabrication of rectifying contacts to p-type silicon much more difficult.

Ohmic contacts can be formed in several different ways. First, if the barrier height is small, conduction across the barrier is possible due to thermionic emission. On silicon, a barrier height of about 0.4 eV or less will suffice. For example, platinum silicide ($q\phi_{Bp} \approx 0.25$ eV) has been used to contact the p-side layers of the mesa diodes. Another method of obtaining ohmic contacts is to cause the majority carriers to be more numerous at the junction than in the bulk by using a metal-n⁺-n or metal-p⁺-p doping arrangement. This arrangement, known as a Schottky ohmic contact can be fabricated on n-type silicon by using a gold-antimony eutectic alloy. A third method

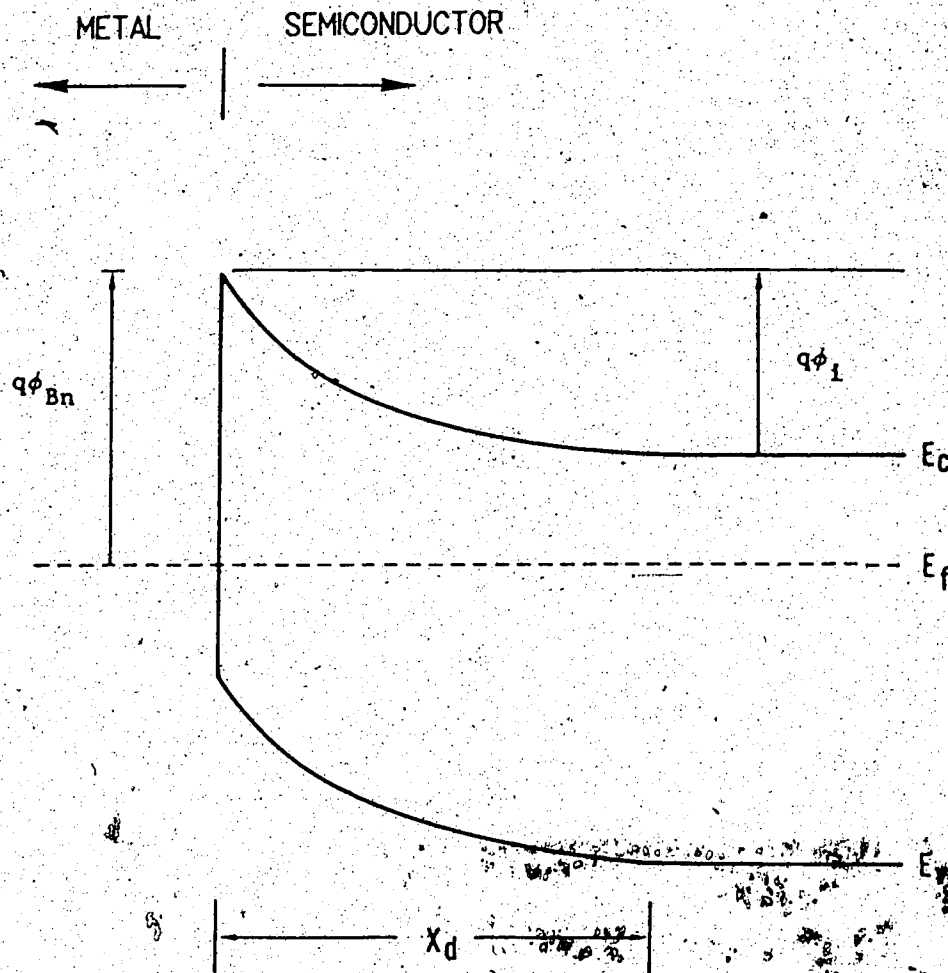


Fig. 3.1 Energy level diagram for a metal-semiconductor junction. Shown for PtSi on 4 Ω -cm n-type silicon.

47

is through the use of tunnel contacts. By using a highly-doped semiconductor, the depletion width can be made very narrow. Although the barrier height may be substantial, the narrow width reduces its effectiveness due to tunnelling through the barrier. Tunnelling starts to contribute to the contact current when doping levels reach about 10^{18} cm^{-3} [13]. All three methods of obtaining ohmic contacts have been used in the fabrication of the mesa diodes.

For rectifying contacts, a high barrier height and moderate doping levels are required. A Schottky diode is formed between the metal and the semiconductor where the metal acts as the positive side of the diode. It should be noted that the current will be blocked in one direction only (from semiconductor to metal) which must be taken into account with the mesa design.

Measurements of the contact characteristics will of course require two contacts. The testing procedures consisted of placing pairs of contacts on silicon substrates of different doping concentrations. Two rectifying metal contacts on a semiconductor will form a pair of opposed (back-to-back) Schottky diodes. The I-V curves for this pair should be symmetric with one diode being forward-biased and the other reverse-biased. Since the current will not be limited by the forward-biased diode for applied voltages larger than several kT/q , the I-V curve will show only the reverse biased characteristics of the M-S junction. This is not the best measurement technique as the forward bias characteristics (which are most often used for Schottky diode characterization) are not observable.

The resistance will consist of two components: (a) the substrate resistance, R_s , which depends on doping and geometry will result in a

linear I-V behavior, and (b) the contact resistance, R_c due to the M-S barrier will result in a diode-like I-V behavior. By comparing the measured resistance with the expected values of R_c and R_s , some characterization of the contacts is possible.

The substrate resistance can be estimated by using a simple approximation for the average current path across the contacts:

$$R_s = \rho L_s / WT \quad (3.1)$$

where T is the wafer thickness, L_s is the contact separation distance and W is the contact width. Although the current path will be longer when T is similar to L_s in magnitude, the resistance will actually be much less since the current path is not limited to the region between the contacts only.

The contact resistance is estimated by using the relationship between the current and the applied voltage in the Schottky barrier approximation as found in Appendix A:

$$R_o = R_c = kT / qI_{ms0}(0) \quad (A.10)$$

For the opposed diode arrangement, the current restrictions will be similar for each diode when $V = 0V$ and hence the measured resistance, R_m will actually be of $R_m = 2R_c + R_s$. In order to avoid any effects of the forward biased diode, R_c is also calculated for non-zero V_a . From the derivative of Eqn. A.1:

$$\frac{\partial I}{\partial V_a} = \frac{\partial I_{ms0}}{\partial V_a} (e^{qV_a/kT} - 1) + \frac{I_{ms0}}{kT/q} e^{qV_a/kT} \quad (3.2)$$

and letting V_a be negative (for the reverse biased diode), the exponential terms will be negligible leaving:

$$\frac{\partial I}{\partial V_a} \approx - \frac{\partial I_{ms0}}{\partial V_a} = -I_{ms0} / 2(\phi_1 - V_a) \quad (3.3)$$

which gives a contact resistance of:

$$R_{c1} = \partial V_a / \partial I = 2(\phi_1 - V_a) / I_{ms0} \quad (3.4)$$

As an arbitrary choice, contact resistance measurements have been made at $(\phi_1 - V_a) = 1$ as well as at $V_a = 0v$ in order to better compare the measured results with theory.

The contacts used for these measurements are the same size as the mesa contacts (1.2mm by 50 μ m). They were placed in pairs with widths L_s of 300, 500 and 700 μ m. In addition, contacts were placed on the substrate with each group of mesas processed. It was hoped that these would provide some insight into the large leakage currents that were found in the first samples grown. For each group of mesas, there were three n-n pairs, three p-p pairs and three p-n pairs as shown in Fig. 2.7.

3.2 Reverse Bias Effects

Although the predicted I-V characteristics are assumed to follow the theory of the Schottky barrier which is based on the diffusion properties of the junction, the observed I-V curves appear to be quite different in many cases. Before going into the details of the contact results, there are several other complications that need to be mentioned.

One of the assumptions of Schottky theory is that the majority carrier concentration will be unaffected by the current flow [23]. The FZ substrates used have a majority carrier concentration that is only

two orders above n_1 and hence only small currents are needed to violate this condition. Using a current of 10^{-8} A at 1.0v (typical for platinum silicide on FZ) will result in an injected carrier concentration of $n \approx 3 \times 10^8 \text{ cm}^{-3}$ which is much less than N_d . However, magnesium contacts on FZ have a low barrier height which allow much higher currents. For example, a current of 10^{-4} A at $V_a = -5$ v will result in a carrier concentration of $n \approx 10^{12} \text{ cm}^{-3} \approx N_d$. Under such conditions, the assumptions of the Schottky theory are no longer valid.

Another approach to current transport is thermionic emission theory [23]. In this case, the reverse bias current is independent of both the doping concentration and the reverse bias. Since the observed I-V curves appear to follow the square root dependence on voltage as given by Schottky theory, thermionic emission theory has not been used to characterize the contacts.

Under reverse bias, the barrier to electron flow from metal to semiconductor will be reduced due to an effect known as Schottky barrier lowering [22]. The metal contact which acts as a conducting plane, will have the effect of a positive image charge on the electron, reducing the barrier height. For FZ substrates, the effect is negligible but for substrates with N_d on the order of 10^{15} cm^{-3} the barrier lowering will cause an increase in the current as shown in Table 3.1 below. Although the effect is even larger at higher doping levels, rectifying contacts on silicon with concentrations higher than 10^{15} cm^{-3} have not been required in the fabrication of the nipi's.

Table 3.1. J/J₀ due to Schottky barrier lowering

Applied Voltage	Na=10 ¹² cm ⁻³	Na=10 ¹⁵ cm ⁻³
0. v	1.06	1.5
-1.	1.11	1.8
-2.	1.13	2.0
-5.	1.16	2.3
-10.	1.20	2.7

The field required for breakdown on FZ is low ($V_B \approx 4 \times 10^4$ V/cm) [22] but because the space charge region is also very large, avalanche breakdown across the junction is not expected. However, the corner on the metal contact where it touches the semiconductor may cause an edge leakage current which can be quite large [23]. In practical diodes, a doped guard ring is usually placed under this edge to increase the breakdown voltage near the corner. It is not possible to predict or characterize this effect in the junctions considered here but it must be noted as a possible cause of some of the high reverse bias currents observed.

In both M-S junctions and p-n junctions, the generation current, due to the net generation of carriers in the space charge region can significantly contribute to the reverse bias current. The low doping concentration of the FZ wafers results in a very wide depletion region and the generation currents are found to dominate in many cases. Recombination centers at the metal-semiconductor interface are also expected to contribute to the generation current [22]. Although this contribution may be significant, it is difficult to estimate. A summary of the recombination current equations is given in Appendix A.

The presence of a thin oxide layer between the metal and the semiconductor will cause a change in the expected behavior of a

Schottky diode [24]. The effect is very sensitive to the oxide width and can result in an increase in the reverse bias current as well as a slow turn-on of the forward bias current. Fig. 3.2 depicts qualitatively the resulting change in I-V behavior for various oxide widths.

The effects of oxide contamination between the metal and semiconductor has also been described in other terms. The oxide layer has the effect of drastically changing the expected barrier height of the M-S contact. For aluminum contacts on clean p-type and n-type silicon, the barrier heights are expected to follow $\phi_{Bp} < \phi_{Bn}$ but oxide formation during evaporation will cause ϕ_{Bp} to be greater than ϕ_{Bn} with $q(\phi_{Bp} + \phi_{Bn}) = E_g$ at all times [25]. In the case of antimony on silicon, the oxide formation will have the opposite effect resulting in higher barrier height on n-type silicon [26].

Each of the effects greatly increases the difficulty in characterizing the contacts considered in this work. In addition, other effects specific to particular metals also may be coming into play as described in the following sections.

3.3 P-Side Contacts

For the p-side of the mesa, the contact metal is expected to form an ohmic contact with p-type layers but provide a rectifying barrier with the intrinsic layers and with the substrate. For the NRC MBE chamber, the intrinsic layers are in fact lightly doped n-type with $N_d \approx 10^{15} \text{ cm}^{-3}$. The substrates used for nipi fabrication have also been lightly doped n-type with $N_d \approx 10^{15} \text{ cm}^{-3}$ (CZ wafers) and $N_d \approx 10^{12} \text{ cm}^{-3}$ (FZ wafers).

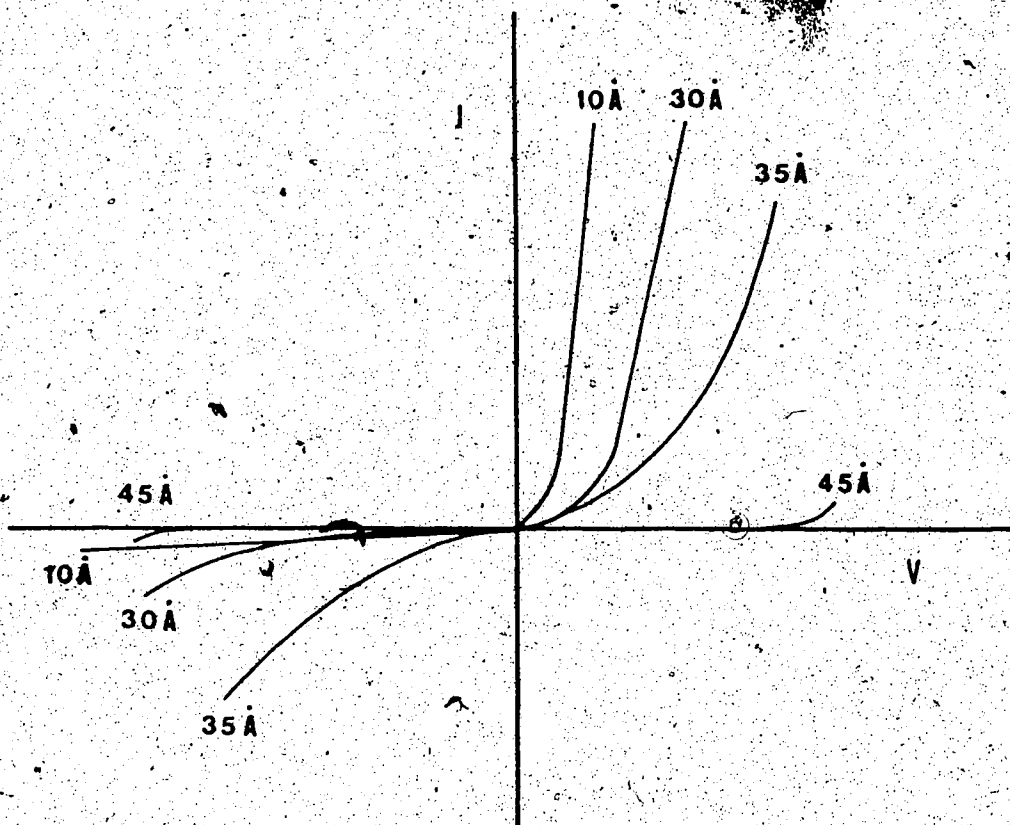


Fig. 3.2 Effect of a thin oxide layer between a metal and a semiconductor. The thickness of the oxide layer is indicated for each curve. For very thin layers, the oxide has no effect. For layers $>40 \text{ \AA}$, the insulating effects restrict the current. Natural oxides on silicon tend to be up to 60 \AA thick. (Modified from Ref. 24)

These contact requirements can be met by using a Schottky diode with a high barrier height. Platinum silicide provides such a barrier, and has been used for the majority of p-type contacts. The barrier height for platinum silicide, is $q\phi_{Bn} = 0.85\text{eV}$ and is fixed by the pinning of the Fermi level [23]. Results for the platinum silicide contacts are summarized in Table 3.2. For platinum silicide on p-type material, the low barrier of $q\phi_{Bp} = 0.26\text{eV}$ should be small enough to allow ohmic behavior with the predicted values for R_s and R_c are both in the range of 1000. Fig. 3.3a is a typical example. The value of the resistance implied by this figure is higher than predicted. The profiles of the I-V curves are fairly linear but show a slight upturn as the bias increases which is the opposite of the square root dependence expected for a Schottky barrier. A possible explanation for this is the formation of a thin oxide layer (Sec. 3.2) which could explain both the observed profile and the higher resistance.

Platinum silicide on p^+ can be observed with the mesa split contacts before the etching of the notch. The I-V curves (Fig. 3.3b) are quite linear and have measured resistances on the same order as R_s . For both the p-type and p^+ silicon, contacts have been formed with a low barrier height and which exhibit an ohmic behavior. Platinum silicide is therefore expected to perform adequately in the contacting of the p-type layers of the mesas.

For platinum silicide on n-type silicon, the measured resistance agrees favourably with the value of the contact resistance and is much larger than the substrate resistance. Resistance measurements at both $V_a = 0\text{v}$ and $V_a = 1\text{v}$ agree with the predicted R_c values. The I-V curves also exhibit the expected square root dependence as well. See Fig. 3.4

Table 3.2 Summary of PtSi Results.

	n-type	FZ	p-type
Impurity type	n	n	p
Doping level (cm^{-3})	10^{15}	10^{12}	2×10^{15}
ρ ($\Omega\text{-cm}$)	4	7000	6
ϕ_i (eV)	0.288	0.1	0.307
ϕ_{Bn} (eV)	0.85	0.85	
ϕ_{Bp} (eV)			0.25
Calculated:			
R_s (Ω)	10^2	10^3	10^2
R_c (Ω)	10^8	5×10^9	small
R_{c1} (Ω)	4×10^9	3×10^{11}	10^2
R_g (Ω)	10^{10}	4×10^8	
Measured:			
R_m at $V=0v$ (Ω)	1.2×10^8	$0.7-2 \times 10^8$	1400
R_m at $V=1v$ (Ω)		$0.4-2 \times 10^9$	800
R_m at $V=2v$ (Ω)	2.5×10^9		800
Dominant R	R_c	R_g	R_s

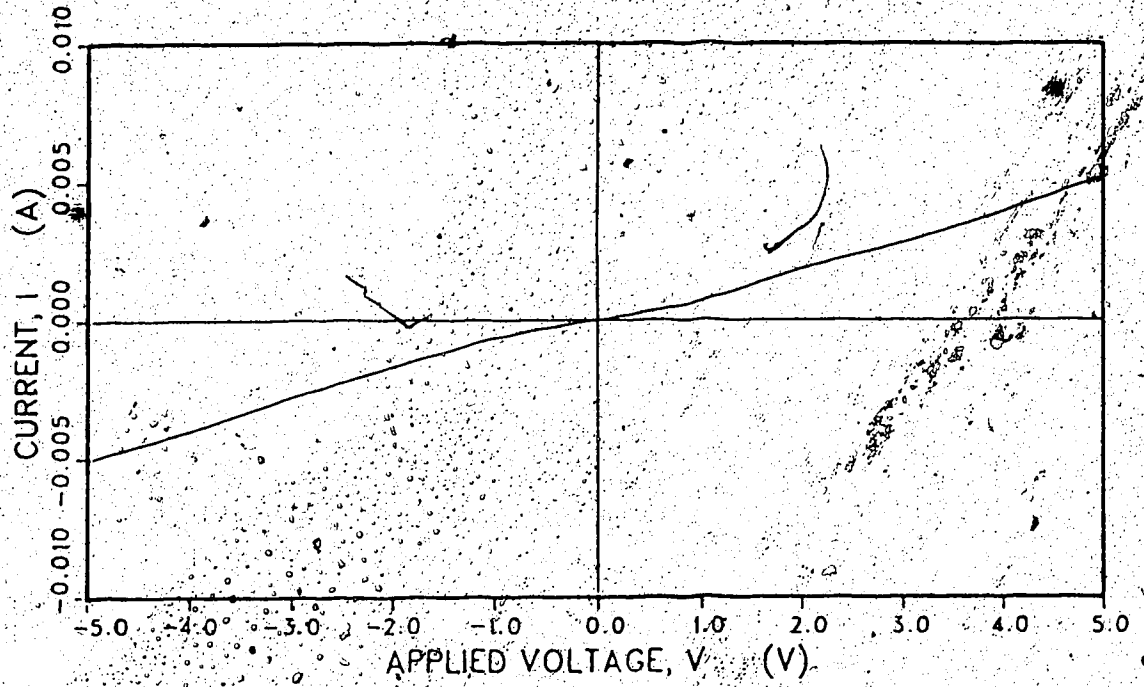


Fig. 3.3a I vs V for PtSi on 6 Ω -cm p-type silicon.
(Re-drawn from original measurement curve.)

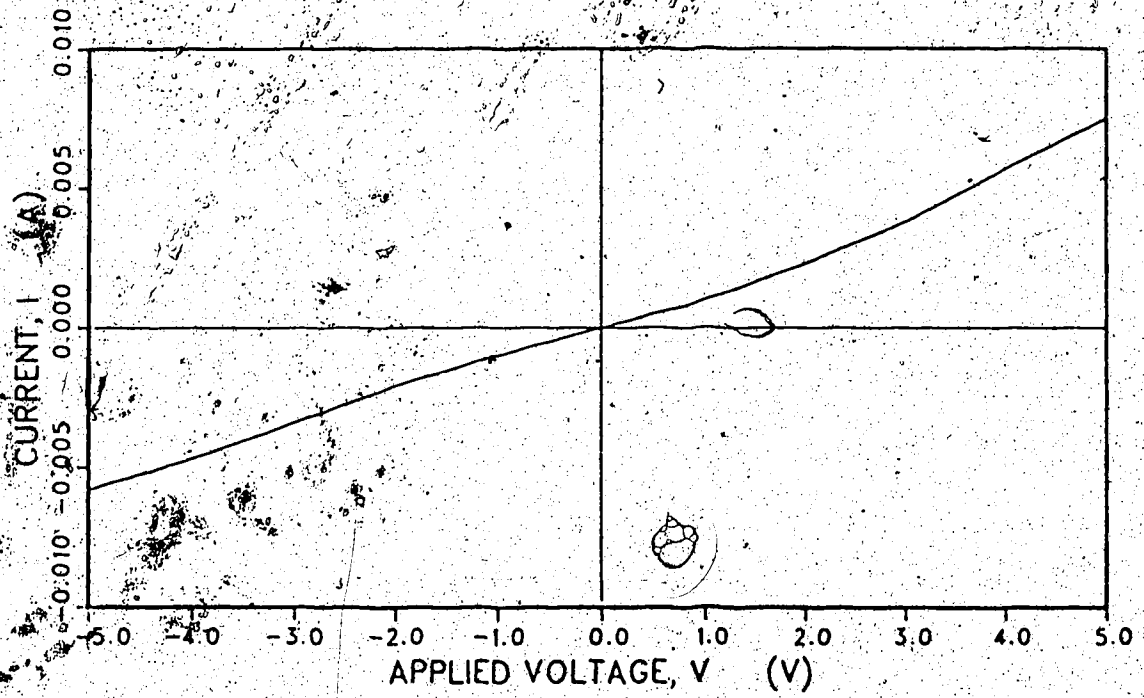


Fig. 3.3b I vs V for PtSi on 0.02 Ω -cm p-type silicon.
From MBE 360 #2C split contact before notch removed.
(Re-drawn from original measurement curve.)

for a typical example. The observed currents were larger than predicted though and curve fitting with Schottky theory indicates that a smaller barrier height of $q\phi_{Bn} \approx 0.8\text{eV}$ may have been formed.

The reverse bias current is a very sensitive function of the barrier height $q\phi_B$. Although for platinum silicide, $q\phi_{Bn}$ is generally listed as about 0.85eV, several factors can affect its value. One possible source of complication is associated with the reaction kinetics for platinum silicide which follow: $\text{Pt} + \text{Si} \rightarrow \text{Pt}_2\text{Si} \rightarrow \text{PtSi}$ [27]. If annealing is done at too low a temperature, the reaction could be halted with only a partial formation of PtSi. Since the annealing temperature used by Andrews [27] to obtain complete PtSi formation was 600°C in comparison with the annealing temperature of 500°C for the PtSi contacts tested here. Since the barrier height for Pt_2Si is 0.78eV, partial PtSi formation could yield a barrier height anywhere between 0.78 and 0.87eV. As mentioned above, by reducing the barrier height to about 0.8eV, close fit for the n-type I-V curves can be obtained. For the FZ substrate, even when the barrier height is reduced to 0.78eV, the theory and measurement do not match.

For platinum silicide on the FZ substrate, the calculated value for R_c is larger than for the n-type substrate, because of the lower carrier concentration. The measured results show the opposite effect though with a drop in the measured resistance. For small V_a ($\pm 3\text{v}$), the I-V curves show the expected square root dependence (Fig. 3.5a) but the measured resistance is much smaller than the expected R_c for the Schottky barrier. In the case of FZ substrates, generation currents are probably the dominant current transport mechanism. Fitting the observed profiles with Eqn. A.7 gives an effective lifetime of about

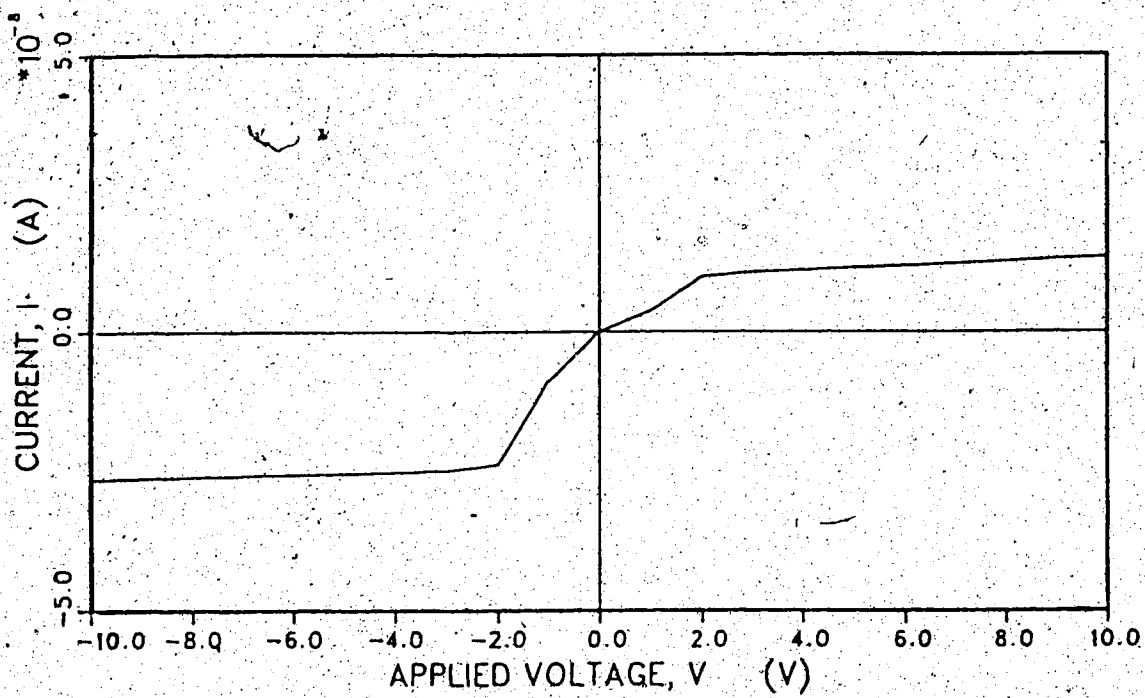


Fig. 3.4 I vs V for PtSi on 4 Ω-cm n-type silicon.
(Re-drawn from original measurement curve.)

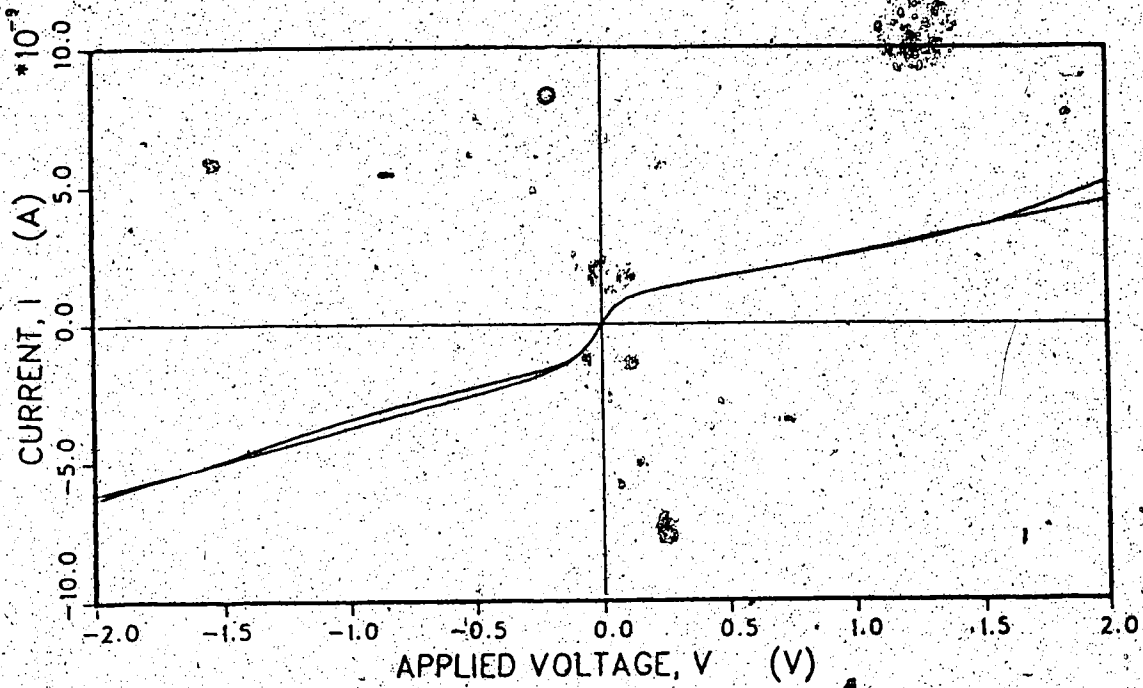


Fig. 3.5a I vs V for PtSi on FZ substrate.
Curves are shown for two contact pairs.

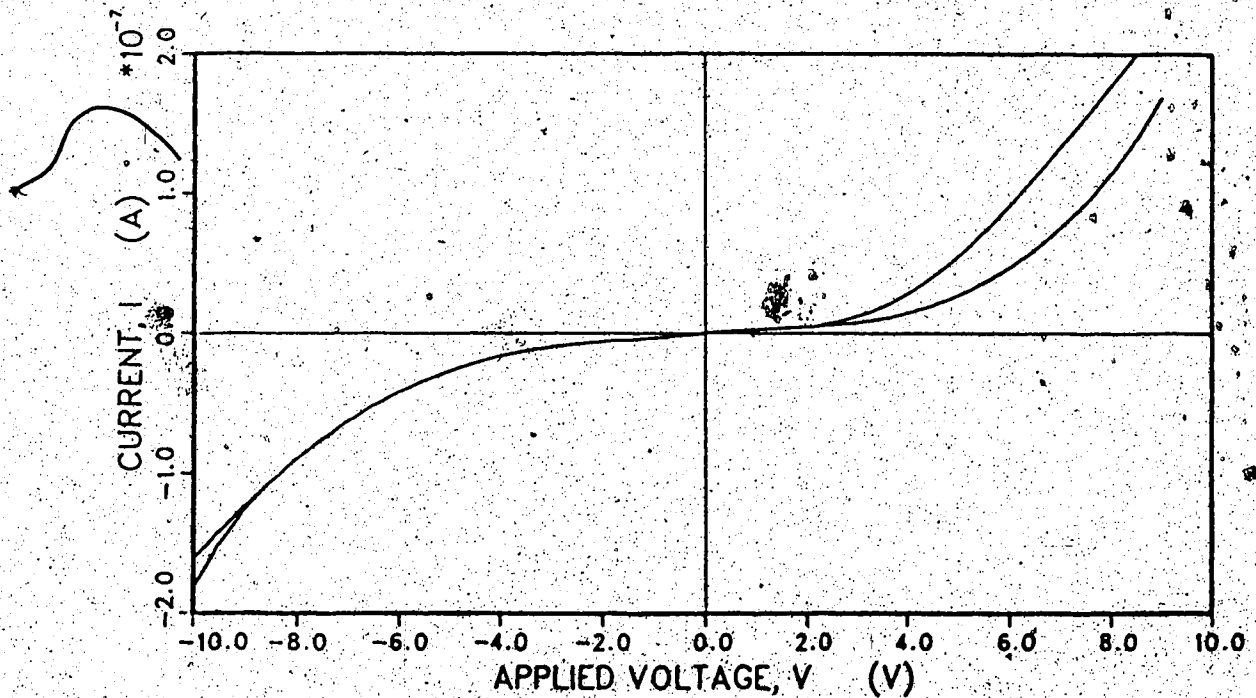


Fig. 3.5b I vs V for PtSi on FZ substrate showing increased leakage at higher voltages.

$\tau = 2 \mu\text{sec}$. As V_a increases, the current takes an upturn as shown in Fig. 3.5b. The current is small enough that the carrier equilibrium condition has not been violated, even at $V_a = 10\text{v}$. As well Schottky barrier lowering is not expected to contribute as noted earlier. It is speculated that the current increase at the higher voltages is due to edge effects. Since the contacts need only operate under small voltage conditions ($\pm 2\text{v}$), the increased current at higher voltages does not present a problem.

The variation in the reverse bias characteristics for the Pt-Si pairs varies substantially from sample to sample, from wafer to wafer and from contact to contact on the same sample. The measured resistances in the majority of cases have the values shown in Table 3.2 but some can drop to as low as $7\text{M}\Omega$ vs the normal $500\text{M}\Omega$. The onset of the upturn in the curves also appears to vary quite a bit but is generally around 3 to 5 volts.

Results indicate that platinum silicide will serve as an adequate contact for the p side of the mesas. Ohmic behavior is observed on both p and p^+ type silicon while a rectifying barrier is provided on n-type silicon. Since there were few difficulties with the fabrication of the platinum silicide contacts, they have been used for the majority of the p-side contacts.

3.4 N-Side Contacts

For the n side, the contact metal must form an ohmic contact with the n-type layers and provide a rectifying contact with the intrinsic layers and the substrate. Since both the background material and the substrates used also consist of n-type silicon, the task of providing a

good contact metal is more difficult. Materials that have been tried to date for the n-side contacts are magnesium, aluminum and gold-antimony.

The first material used for the n-type contacts was magnesium with a layer of aluminum on top to inhibit oxidation. Experimental results suggest that the barrier height is pinned due to surface states as in the case of platinum silicide. A barrier height of $q\phi_{Bn} = 0.4\text{eV}$ for magnesium on both p-type and n-type silicon has been reported for unannealed contacts on very clean silicon surfaces (cleaved during evaporation) [26]. The literature available for magnesium contacts on silicon is very limited.

The NRC [28] has also measured the barrier height for magnesium on n and p-type silicon. Measurements of the contact resistance, R_c on n⁺ silicon indicate a barrier height of $q\phi_{Bn} \approx 0.42\text{eV}$ while results for p⁺ silicon give $q\phi_{Bp} \approx 0.85\text{eV}$. Since the sum of $q\phi_{Bn}$ and $q\phi_{Bp}$ is expected to equal the bandgap E_g , the barrier on p-type should be much lower than measured. The difference may be due to the additional barrier height introduced by the p⁺ silicon of $E_c - E_F \approx 0.9\text{eV}$. For unannealed silicon, the results agree closely with Ref. 26. However, measurements for annealed magnesium show an increased barrier height of $q\phi_{Bn} \approx 0.48\text{eV}$.

Magnesium on n-type material exhibits a linear behavior with low resistance, $R_m = 140\Omega$ which compares with the expected substrate resistance of $R_s \approx 50-180\Omega$ as shown in Fig. 3.6a. Because of the linear nature of the I-V curve and the fact that $R_m \approx R_s$, it is assumed that R_c is less than R_m and good ohmic contact with the n-type material has been made as predicted. In order to keep R_c smaller than R_m and

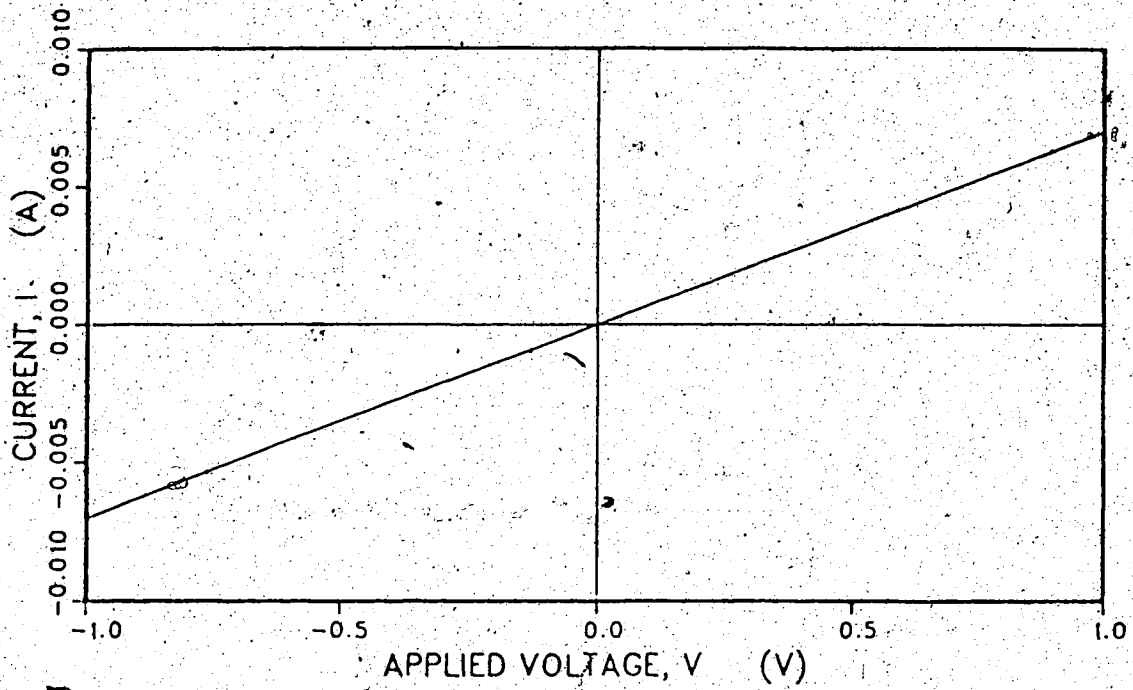


Fig. 3.6a I vs V for Mg on 4 Ω -cm n-type silicon.
(Re-drawn from original measurement curve.)

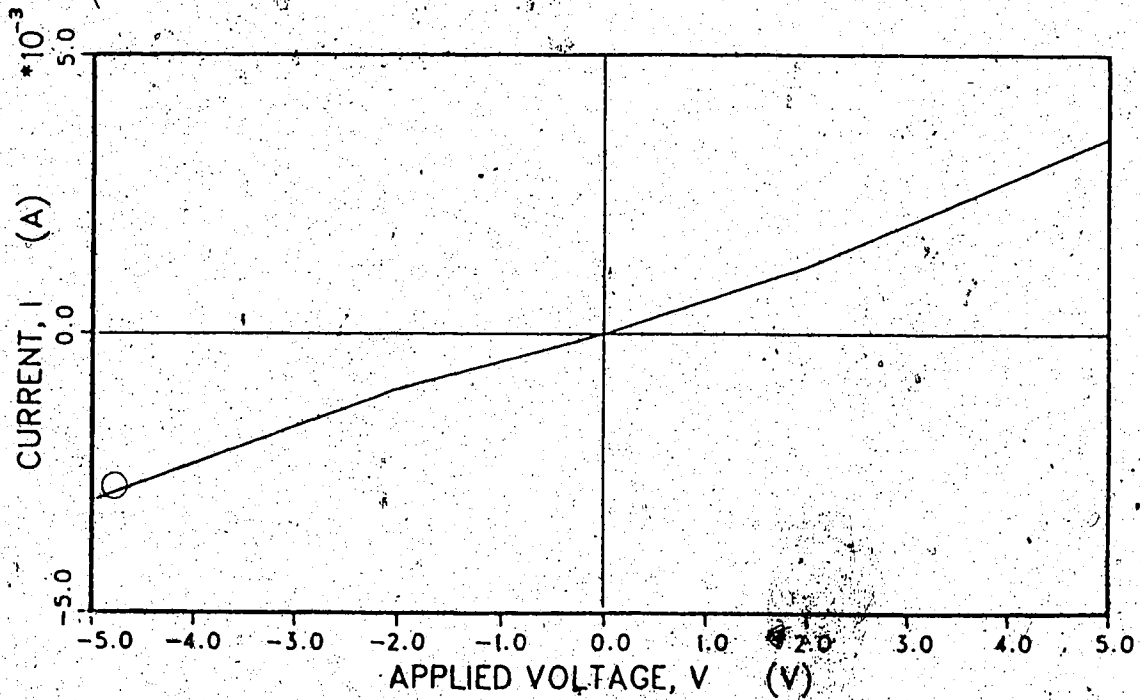


Fig. 3.6b I vs V for Mg on 0.02 Ω -cm n-type silicon.
From MBE 360 #2C split contact before notch removed.
(Re-drawn from original measurement curve.)

R_s , it is required that $q\phi_{Bn} \leq 0.42\text{eV}$ which is similar in magnitude to the unannealed values.

The contact resistance was also measured using the split contacts on the nipi mesa before the notch was etched. The magnesium contacts exhibit a linear behavior as shown in Fig. 3.6b. The measured resistance of $R_m \approx R_s \approx 1.5\text{K}$ implies that $q\phi_{Bn}$ must be less than 0.45eV . Tunneling is expected to occur on the mesa edge though so $q\phi_{Bn}$ cannot be reliably estimated in this way.

The results for magnesium on FZ vary substantially from sample to sample. Although the FZ is an n-type substrate, results indicate a high barrier height. Curve fitting of the predicted reverse bias current, I_{sn} to the I-V data, requires that $q\phi_{Bn}$ be in the range of 0.46 to 0.6eV , depending on the sample. As has been noted, the physical appearance of the Mg-Al contacts on the FZ substrates is very poor. Some of the problems in fabrication may now be showing up in the electrical characteristics of the contacts and it may be that the barrier height is in fact varying across the samples. The length of time between substrate cleaning (removal of SiO_2) and magnesium evaporation was short but it was not a controlled factor and it is quite possible that a thin oxide layer existed on the substrate before magnesium evaporation. As noted, oxide contamination can result in substantial variations in the barrier height as well as in the general profile of the I-V curves.

The contacts with the lower $q\phi_{Bn}$ usually have an I-V profile similar to the exponential behavior associated with the thin oxide layer. Samples with the higher barrier usually have the expected square root dependency. See Fig. 3.7 for an example. In conclusion,

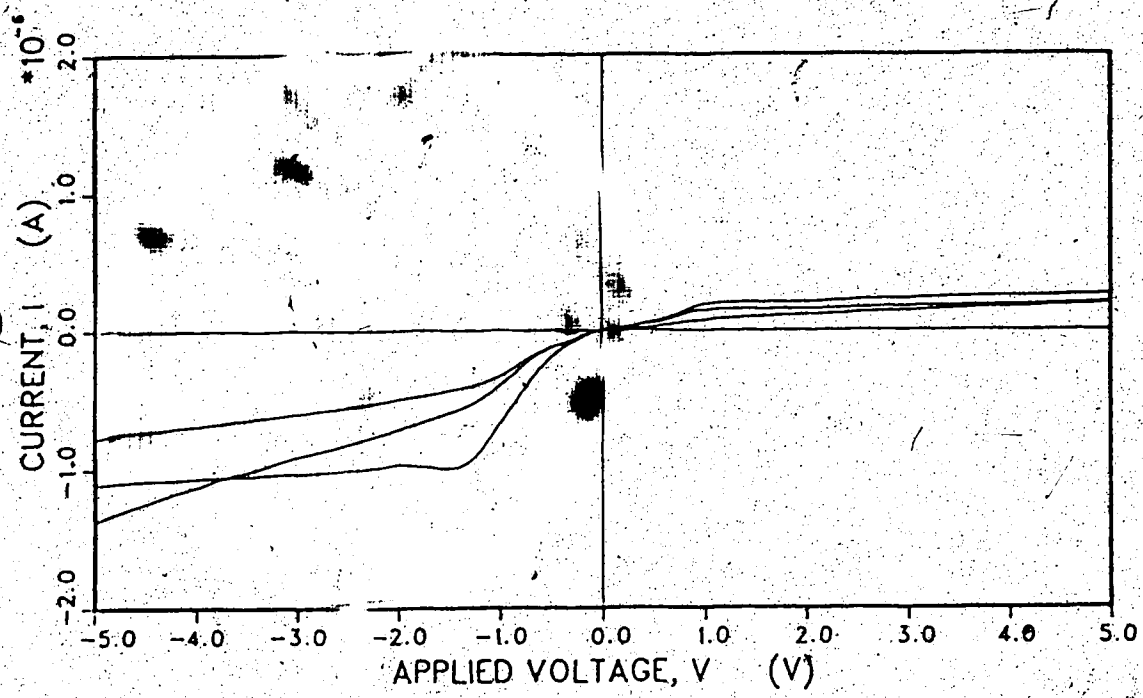


Fig. 3.7 I vs V for Mg on FZ substrate.
Shown are the 3 Mg substrate pairs from MBE 360 #4B.

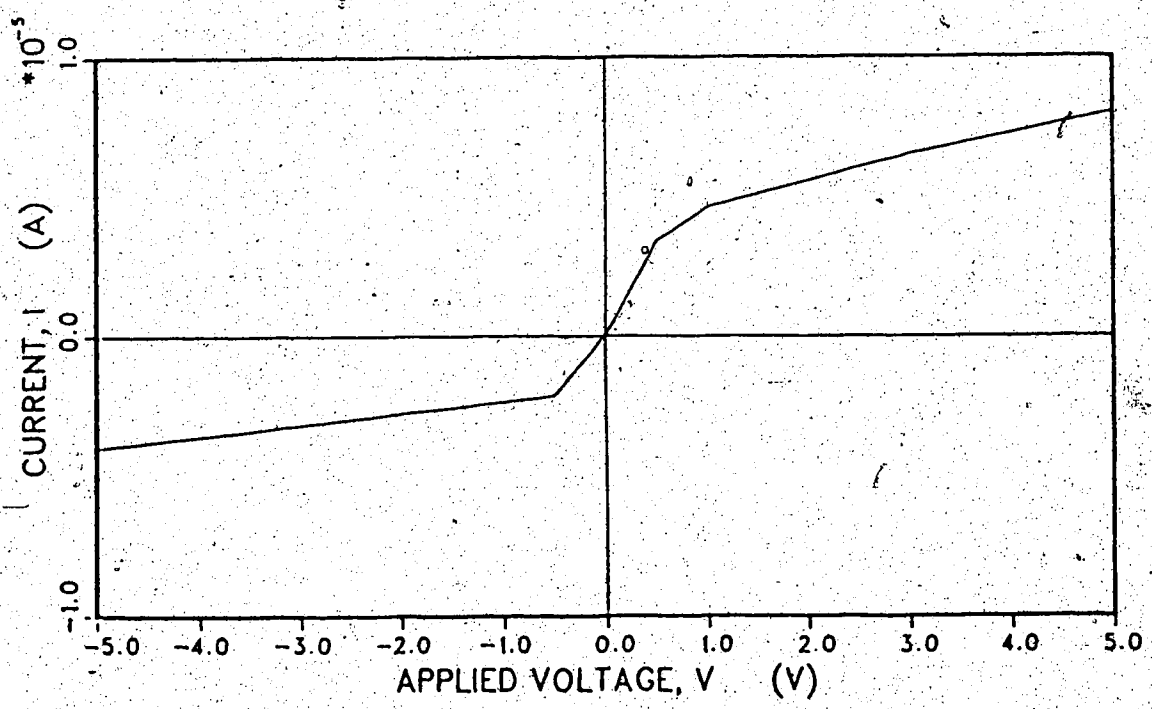


Fig. 3.8 I vs V for aluminum on FZ substrate.
From MBE 391 #5A.
(Re-drawn from original measurement curve.)

there does appear to be some sort of an oxide effect associated with the magnesium contacts which has inhibited the current flow. Whether it is due to a thin oxide layer or to some other form of contamination has not been determined. Although the high barrier height on FZ was not expected, it is in fact a desirable characteristic for the npi mesas since it provides better mesa isolation from substrate effects. The results for magnesium contacts are summarized in Table 3.3.

Aluminum was tried as a contact metal both the n-type and p-type mesa contacts on MBE 360 #2B and MBE 391 #5A. The expected barrier height for aluminum on silicon is $q\phi_{Bn} = 0.7\text{eV}$ [23] and hence the aluminum will form ohmic contacts with p-type silicon and rectifying contacts on n-type silicon. In fact aluminum is used commercially for n-type Schottky diodes. For high doping concentrations of Nd though, aluminum is also expected to form an ohmic contact due to tunnelling effects. The doping levels on the mesa edges where the contacts are placed are expected to be at least 10^{18}cm^{-3} and above as the edge drops off which should be sufficient for tunneling to occur. The advantage of using aluminum is to reduce the substrate effects by providing a better rectifying behavior with the substrate.

The aluminum contacts have not been fully investigated as results are only available for the samples listed above. For aluminum on FZ, the values of R_m vary from 200K to 2M and the current levels measured were much higher than expected as shown in Fig. 3.8. Curve fitting of $q\phi_{Bn}$ indicates a barrier height of about 0.53eV. As discussed above, if there is an oxide contamination with aluminum contacts, $q\phi_{Bn}$ and $q\phi_{Bp}$ reverse in magnitude which seems to be the case here. Muller and Kamins [22] also note the importance of cleanliness in aluminum contact

fabrication. As with the magnesium, it appears that a thin SiO_2 layer during evaporation may be present.

Gold antimony is expected to form a Schottky ohmic contact with n-type silicon as has been described earlier. The antimony will diffuse partly into the silicon during annealing forming a graded junction. The I-V curves for gold antimony on n-type and FZ substrates indicate a barrier height $\phi_{Bn} = 0.5\text{eV}$ as shown in Figs. 3.9a and 3.9b. The problems with gold antimony sticking to the substrate has restricted the availability of data on gold antimony for this work.

Table 3.3 Summary of Magnesium Results.

Source:	Doping (cm^{-3})	ϕ_{Bp} (eV)	ϕ_{Bn} (eV)
Archer [26] (not annealed)	$N_a = 2 \times 10^{15}$ $N_d = 10^{16}$		0.4 0.4
NRC not annealed	$N_a = 6.5 \times 10^{17}$ $N_d = 2 \times 10^{18}$	0.8	0.42
NRC annealed	$N_d = 2 \times 10^{18}$		0.48
D1	$N_d = 10^{15}$		<0.42
Split contacts	$N_d = 10^{18}$		<0.49
FZ	$N_d = 10^{12}$		0.45-0.6
P1	$N_a = 10^{15}$	0.52	

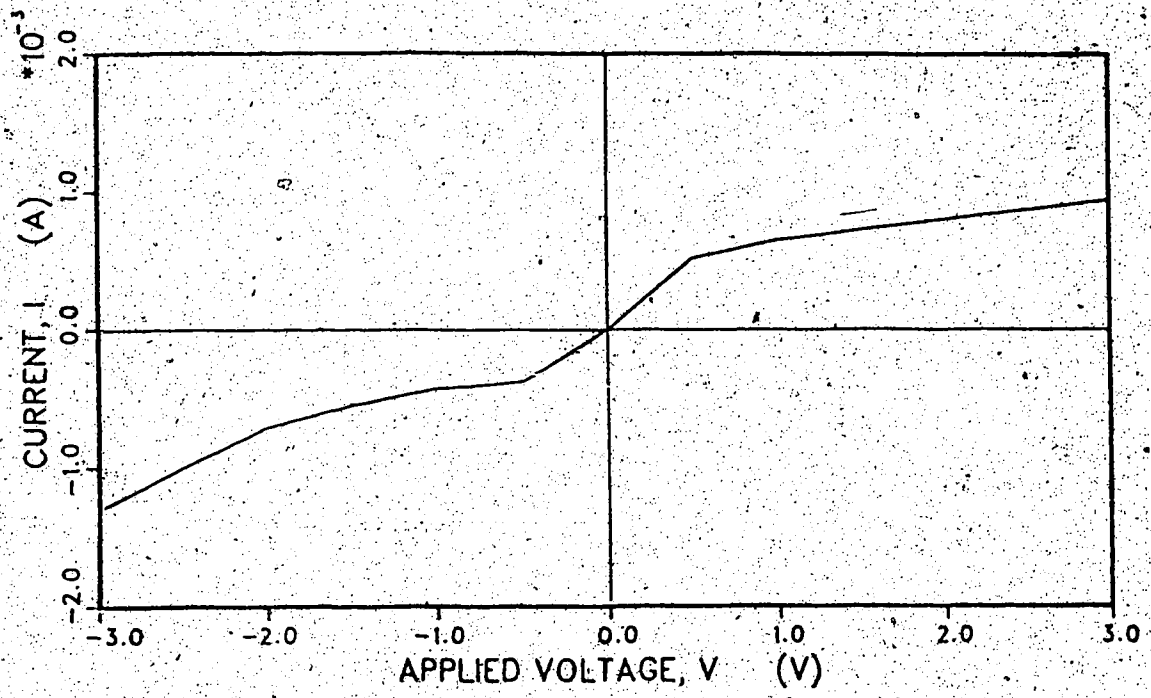


Fig. 3.9a I vs V for gold antimony on n-type substrate.
From MBE 405 #3A.
(Re-drawn from original measurement curve.)

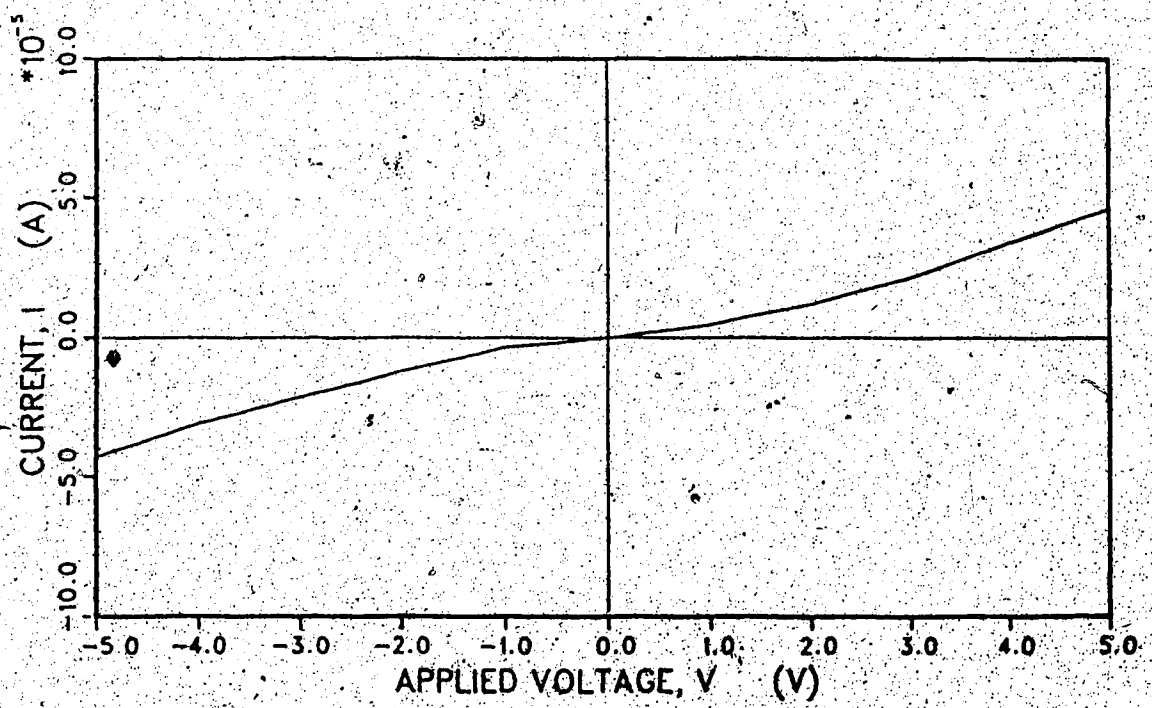


Fig. 3.9b I vs V for gold antimony on FZ substrate.
From MBE 360 #1E.
(Re-drawn from original measurement curve.)

Chapter 4

Electrical Characteristics

A doping superlattice can be considered as a multilayer diode with an unusual geometry as shown in Fig. 2.1b. Each layer will form a p-n junction with the layers above and below resulting in a set of parallel diodes tied together at the contacts. The I-V curves for a nipi from MBE 360 shown in Fig. 4.1 certainly exhibit a diode-like behavior. However, the unusual geometry and complications related to the processing have resulted in some unexpected electrical behavior.

Chapter 4 addresses the electrical characteristics of the silicon nipi and the problems associated with it. Comments on the geometry follow in this section. Section 4.1 discusses the problems found in making contacts on the sides of the nipi which are rectifying with the substrate. The reverse bias characteristics of the nipi's are analysed in Section 4.2 and the forward bias characteristics of the mesa diode are investigated in Section 4.3. Comparison of the electrical behavior with the current transport theory given in the appendix indicates that the substrate leakage effects may still be significant. The tunability of the conductance between the split contacts is discussed in Section 4.4.

The geometry of the nipi diode is quite different than a conventional diode and some of these features are noted here. The area of the p-n junction is large compared to conventional diodes. Even with one period, the junction area would be about 0.01cm^2 , but when multiplied by the number of layer interfaces, the area is on the order of one cm^2 . (For the split contact nipi with 20 periods the p-n junction area is 0.38cm^2 .) The distance between the contact metals is very

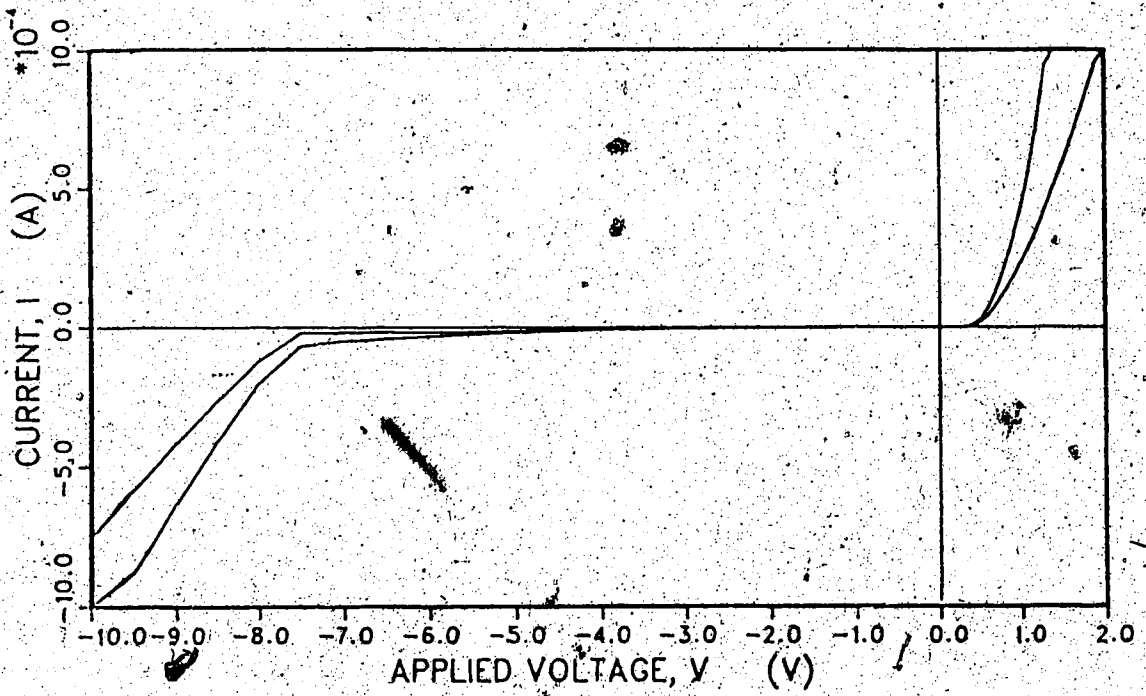


Fig. 4.1 I vs. V of nipi diode for MBE 360 #1E.
Curves are shown for two contact pairs on the split contact mesa.

large (0.4 to 1.0mm). Any design which makes use of the shadow mask technique will be required to be this wide because of the widths of the intrinsic regions at the mesa edges.

It would be simplest to treat the p-n junction interface as if it were uniform over the entire width of the n-p-n-p region. Any fields would be considered to be directly across the p-n junction and would be negligible in the quasi-neutral regions. This would require that the central region of each layer remain as a conducting channel throughout the entire width of the layer. However, as the extent of the depletion region approaches the layer thickness, this assumption may no longer be valid.

The geometry of the nipi mesa contributes to the problem of substrate effects since the area of the mesa-substrate interface is quite large (0.01cm^2 for the split contact mesa). In addition, the width of the depletion region in the substrate ($27\mu\text{m}$ on FZ, $1\mu\text{m}$ on CZ) is significant when compared with the mesa thickness of $1.2\mu\text{m}$. These two factors contribute to the problems associated with substrate leakage.

4.1 Notes on Substrates

The choice of substrate material will effect the measured electrical characteristics of the mesa diode. Some aspects of the substrate effects are discussed in this section. This includes comments on the n-type and FZ substrates used. As well the problem of surface contamination around the mesa and its effect on the contacts is presented.

The first two sets of mesas (MBE 318 and 321) were grown on n-type

CZ substrates with $\rho = 4 \Omega\text{-cm}$. The nipi's processed from these wafers showed a very large reverse bias leakage current ($\approx 1 \mu\text{A}$) and it was felt that the substrate current was probably the cause. In order to help reduce the leakage effects, an n-type substrate with a much lower impurity concentration was acquired. The FZ wafers have a resistivity of $\rho = 7000 \Omega\text{-cm}$ ($\pm 30\%$) and hence a doping concentration of approximately 10^{12}cm^{-3} . This is very nearly intrinsic material ($n_i \approx 10^{10} \text{cm}^{-3}$) and it should be noted that the hole population in this case is only a factor of 2,000 less than the electron population.

The FZ wafers were expected to help in two ways. First, the high resistivity would increase the substrate resistance by a factor of 1000. Second, the lower doping concentration would help to improve the rectifying behavior of the n-side contact with the substrate. The diode characteristics of the M-S contacts on FZ have been discussed in Chapter 3. Both of these improvements have been observed although the magnesium barrier on FZ appears to be higher than expected ($R_c < 50\Omega$ on CZ, $R_c \approx 1M\Omega$ on FZ). The contact resistance for the platinum silicide contacts remained high on both substrate types ($R_c \approx 100M\Omega$).

The mesa contacts are situated such that a portion of the contact is on top of the mesa, a portion is on the actual edge of the mesa providing contact to each of the nipi layers and the remainder is lying on the substrate. The portion of the metal that is directly on the substrate should have the same rectifying behavior with the substrate as did the contacts that were only on the substrate. Unfortunately, there is an additional fabrication factor that completely changes the behavior of the mesa contact with the substrate.

During mesa growth, doping impurities are also being deposited on

the substrate around the mesa; boron on the p-side and arsenic on the n-side. This is evident in Plate IIe where a selective chemical etch has delineated the contaminated regions. These result in an interface of degenerately doped silicon between the contact metal and the substrate. The interface will probably not be a monolayer since some silicon deposition will occur beyond the edge of the shadow mask but the doping concentration can be expected to be very high ($\approx 10^{20} \text{ cm}^{-3}$). On the n-side, the layer may help to form a Schottky ohmic contact with the n-type substrate by forming an accumulation layer next to the contact metal. On the p-side, this interface was not expected to degrade the rectifying ability of the contact since the interface would result in a p^+ layer. However, the actual results for the p-side contacts turned out to be quite different.

One method of observing the substrate effects with the mesa contacts is to take I-V measurements using contacts on two different mesas as depicted in Fig. 4.2. The results for PtSi contact pairs on the substrate and from mesa-to-mesa are shown in Fig. 4.3a and Fig. 4.3b respectively for MBE 360 #4B. The contacts are all the same size and were processed at the same time. The spacing between the mesa-to-mesa pairs is in fact much larger than the substrate pairs and yet the current in the mesa-to-mesa contacts has increased by a factor of 1000. In addition, the square root behavior expected for the M-S junction that is clearly visible in Fig. 4.3a for the substrate contacts is not present in Fig. 4.3b. The I-V profile appears quite linear with a resistance on the order of the substrate resistance ($\approx 30 \text{ K}\Omega$). The rectifying behavior of the platinum silicide contacts that is so crucial to operation of the nipi has somehow been

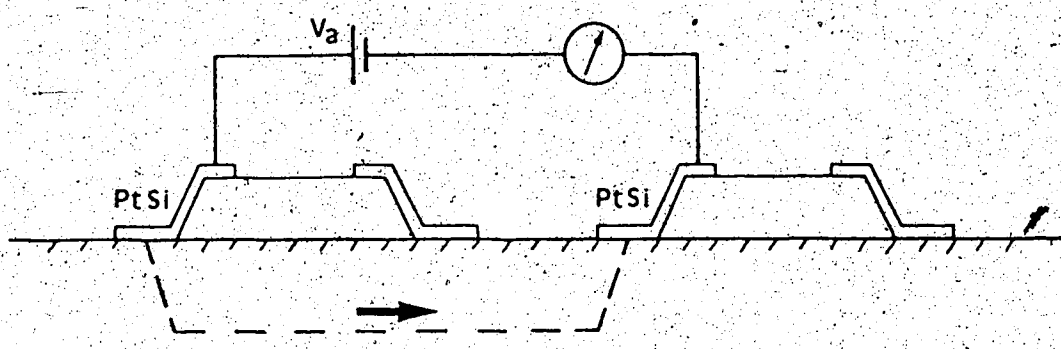


Fig. 4.2 Mesa-to-mesa contacts and I-V measurement.

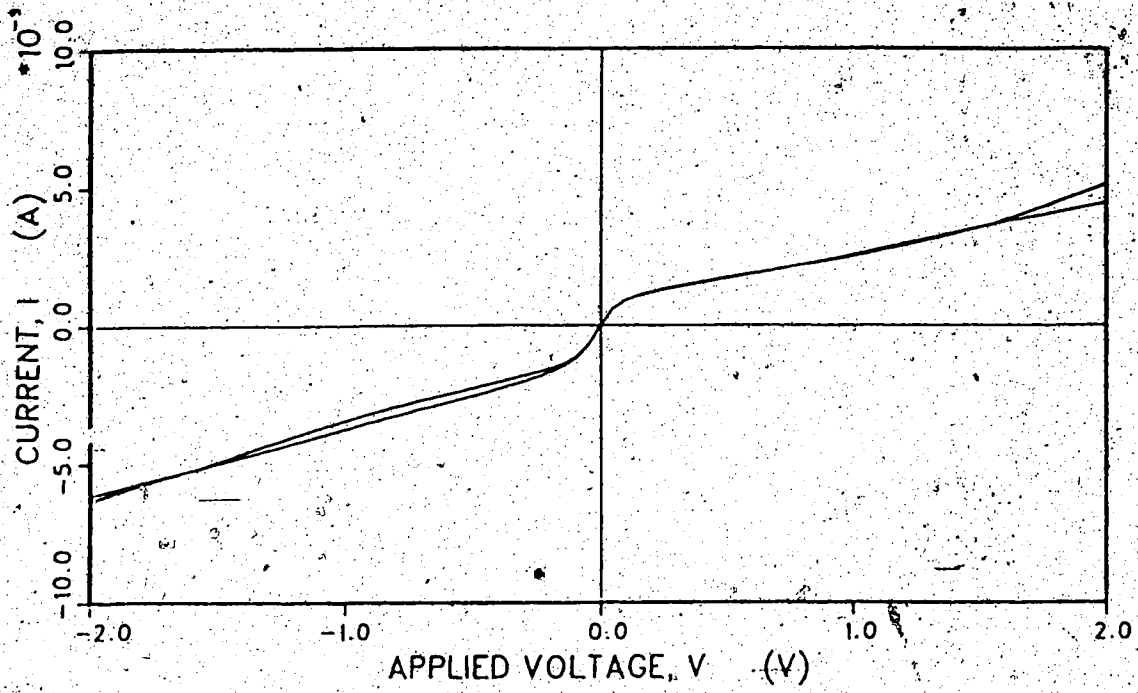


Fig. 4.3a I vs V for PtSi contacts, substrate pairs for MBE 360 #4B. Curves are shown for two contact pairs.

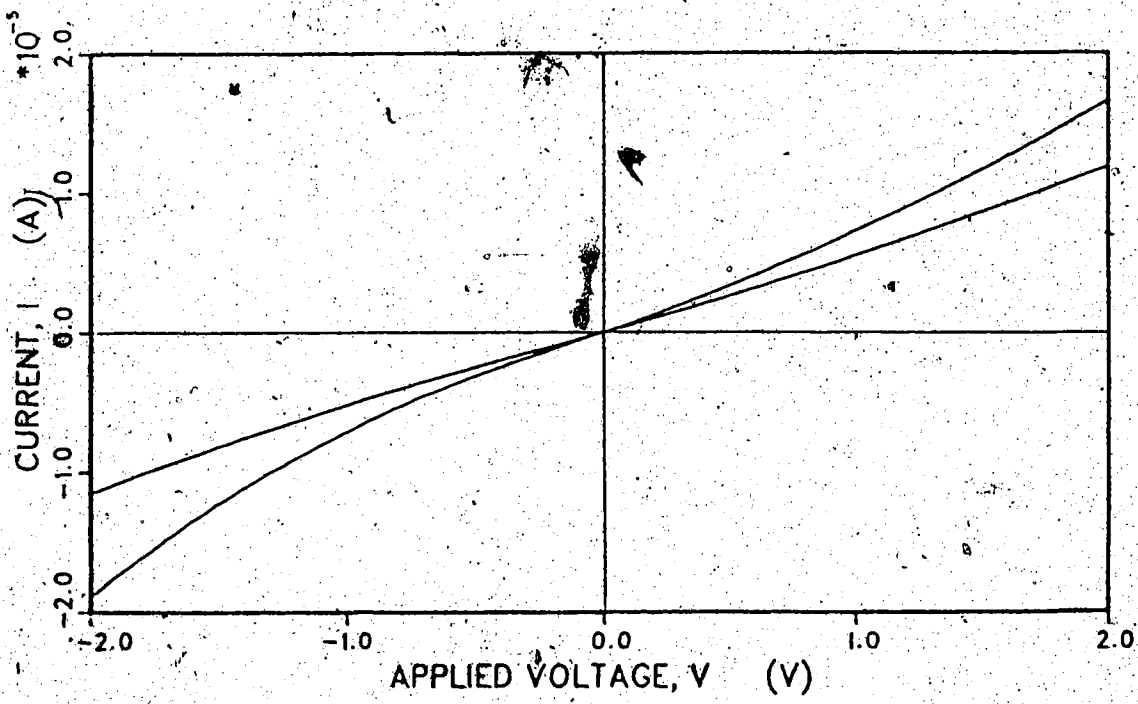


Fig. 4.3b I vs V for PtSi contacts, mesa-to-mesa for MBE 360 #4B. Curves are shown for two contact pairs.

destroyed. The majority of the MBE 360 samples were processed under these conditions and as a result exhibit leaky reverse bias characteristics.

In an attempt to improve the quality of the M-S junction for the mesa contacts, the surface around the mesa underwent an etch to remove the deposited contamination layer. Results of the etch are evident in Plate IIe as has been discussed in Section 2.4. The contacts were then processed in the usual manner. The results for MBE 391 #5E are shown in Figs. 4.4a and 4.4b. Although processed separately, the substrate pairs for the two samples are similar (Fig. 4.3a and Fig. 4.4a). However, the I-V curve for the mesa-to-mesa contact shows a substantial improvement. First, the profile has retained the square root dependence and secondly, the magnitude of the current has dropped by two orders. Table 4.1 compares the contact resistance for the etched and not-etched cases. The removal of the interface layer has restored the rectifying behavior of platinum silicide contacts with the substrate.

Even with the surface etch, the contact resistance observed for the mesa-to-mesa pair is still a factor of 30 less than for the substrate pair. The mesa-to-mesa results are not expected to improve beyond this amount because of a second current path between the two contacts: from the substrate to the bottom p-type layer to the PtSi contact. The predicted generation current through this route is of the same order of magnitude as that observed and hence it is not possible to determine to what extent the contact resistance has improved.

These observations are based on one processed sample, MBE 391 which has the problem of poor definition of the doping layers.

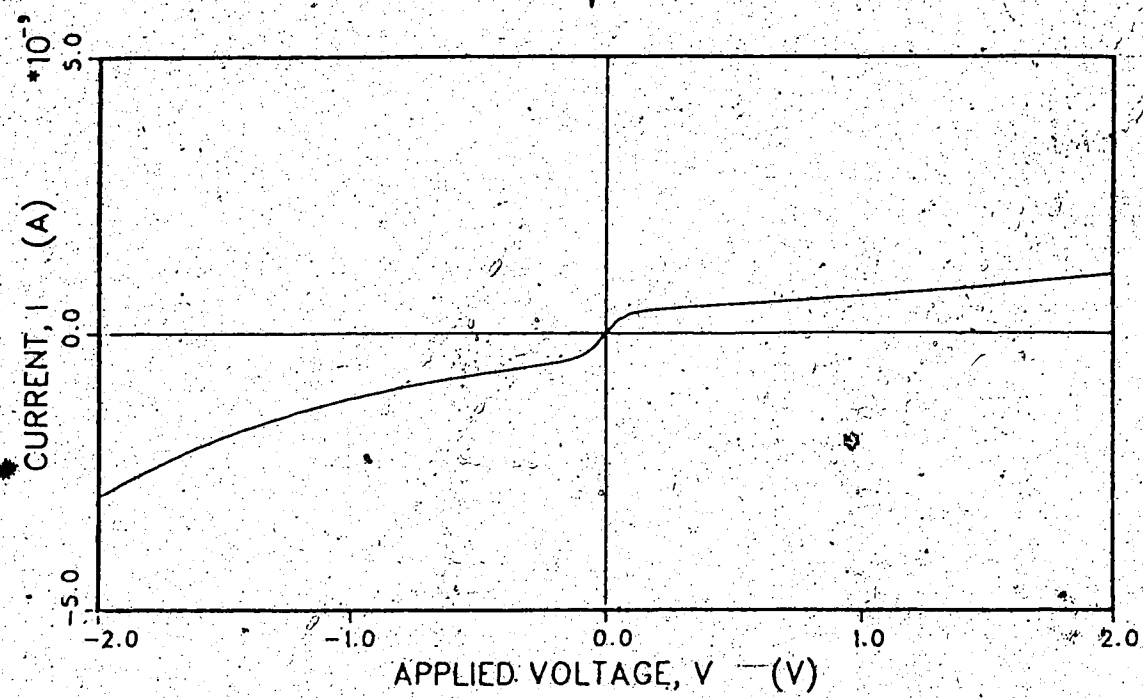


Fig. 4.4a I vs V for PtSi contacts, substrate pairs for MBE 391 #5E.

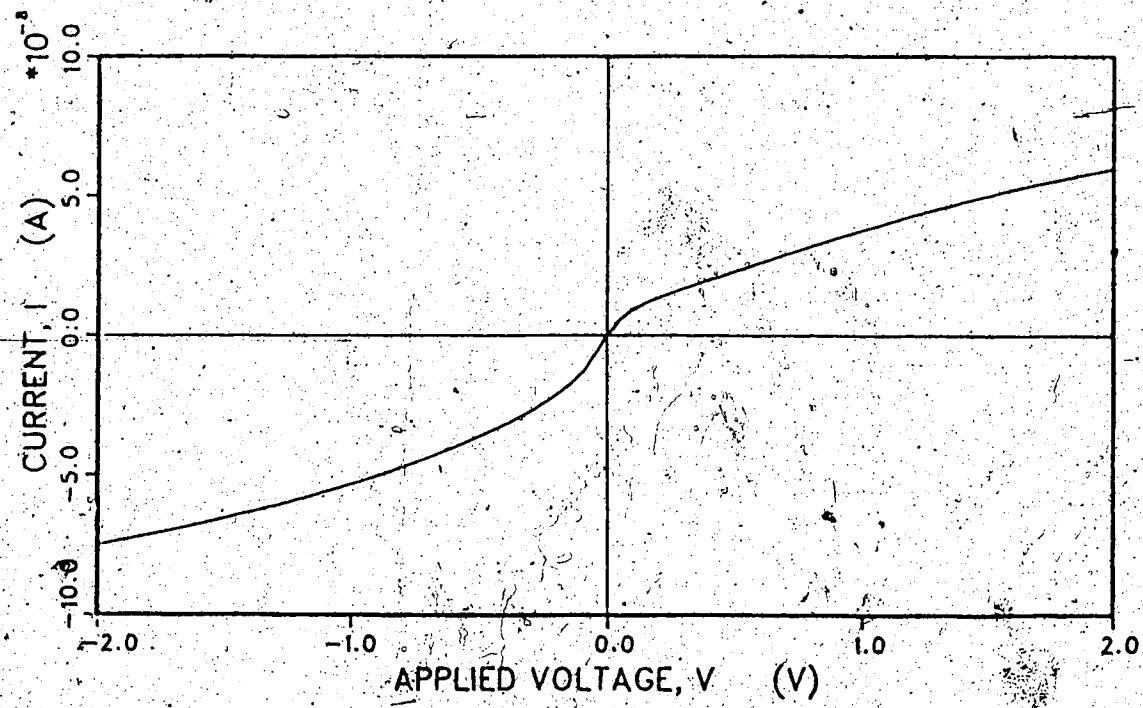


Fig. 4.4b I vs V for PtSi contacts, mesa-to-mesa for MBE 391 #5E.

Table 4.1 Comparison of Fig. 4.3 and Fig. 4.4

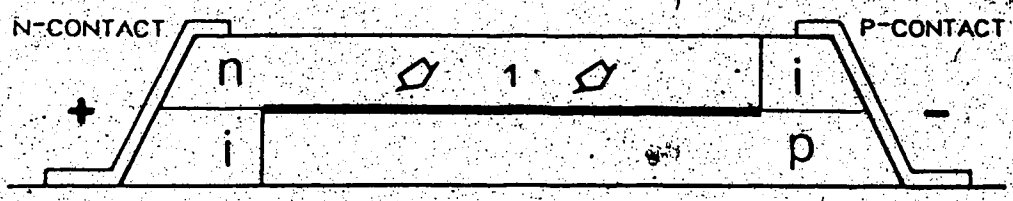
	Mesa to Mesa	Substrate Pairs	Ratio
Resistance at $V_a = 0v$			
MBE 360 #4B	200K Ω	70M Ω	350
MBE 391 #4E	8M Ω	200M Ω	25
Resistance at $V_a = -1v$			
MBE 360 #4B	200K Ω	400M Ω	2000
MBE 391 #4E	50M Ω	1.6x10 ⁹ Ω	30
Current at $V_a = -1v$			
MBE 360 #4B	5 μ A	2pA	1/2000
MBE 391 #4E	0.4pA	1pA	1/40

However, the above discussion is based on the PtSi contact measurements which should not be affected by the MBE growth conditions. Therefore the results and conclusions should be valid. Further measurements with other samples are required to verify the assumptions here. No comparable results are available for the n-side contacts at this time.

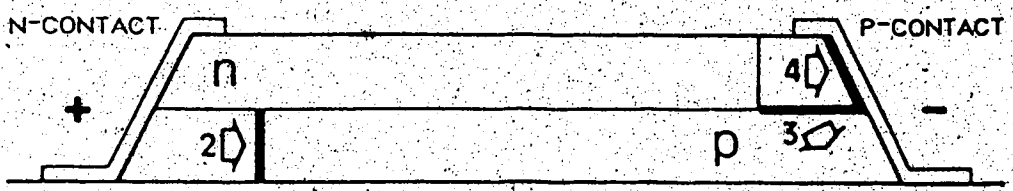
4.2 Reverse Bias Characteristics

In order to observe many of the predicted properties of nipi's it is important that reverse bias currents be kept small. Since future research with nipi's depends so strongly on this factor, a great deal of emphasis in this thesis has been on reducing the reverse bias leakage, in particular: mask design, doping profiles, substrates, rectifying contacts, surface etching and plasma etching. In this section the results of the reverse bias characteristics of the nipi's are presented. As well, the various current transport mechanisms for nipi diodes are discussed.

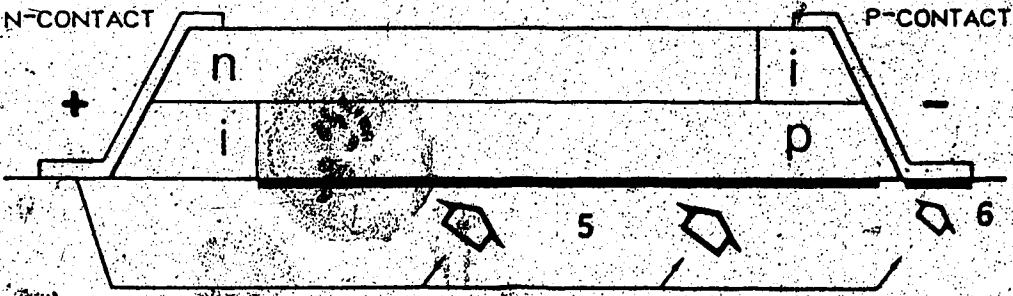
Three main routes for the reverse bias current, depicted in Fig. 4.5 are: (a) current transport across the p-n junctions; (b) current transport via the intrinsic regions found on both sides of the mesa; and (c) current transport through the substrate. (For clarity, only two of the many superlattice layers are shown in the figure.) For each of these paths, there will be several mechanisms for current transport, for example, the p-n junction current may be due to minority carrier diffusion, carrier generation or tunnelling. In order to simplify the discussion that follows, these various current sources are summarized in Tables 4.2, 4.3 and 4.4. (The column "Path" corresponds to Fig. 4.5.) In order to provide a method of comparison for the



A) LEAKAGE ACROSS P-N JUNCTIONS
 PATH 1 JUNCTION AREA = 0.38 CM²



B) LEAKAGE THROUGH INTRINSIC REGIONS
 PATH 2 JUNCTION AREA = 8X10⁻⁶ CM²
 PATH 3 JUNCTION AREA = 0.048 CM²
 PATH 4 JUNCTION AREA = 8X10⁻⁶ CM²



C) LEAKAGE THROUGH THE SUBSTRATE
 PATH 5 JUNCTION AREA = 0.12 CM²
 PATH 6 JUNCTION AREA = 3X10⁻⁴ CM²

Fig. 4.5 Diagram of reverse bias leakage paths. Only the first two layers of the superlattice are shown. Numbers refer to paths. Darkened lines indicate interface region associated with each path.

Table 4.2 Minority Carrier Diffusion Current.

See Eqn. A.3, A.4 $R_o = kT / qI_{so}$ $L_p = 9 \mu\text{m}$, $L_n = 25 \mu\text{m}$, $D_n = 5.2 \text{ cm}^2/\text{sec}$, $D_p = 2. \text{ cm}^2/\text{sec}$

M.C. - Dominant minority carrier type

Junction	Path	Area cm ²	N cm ⁻³	M.C.	I _{so} A	≈ R _o Ω
p-n junction	1	0.38	10 ¹⁸	n&p	3x10 ⁻¹⁴	10 ¹²
p - substrate	5	0.012	10 ¹²	p	2x10 ⁻⁹	30 M
n _i - p (hor.)	3	0.048	10 ¹⁵	p	2x10 ⁻¹²	10 ¹⁰
n _i - p (vert.)	2	8x10 ⁻⁶	10 ¹⁵	p	2x10 ⁻¹⁵	10 ¹³

Table 4.3 Generation Current.

See Eqn. A.7, A.8, A.13 $R_0 = 2kT / qI_{so}$

Junction	Path	Area cm ²	$x_d(0)$	τ μsec	I_{so} A	$\approx R_0$ Ω
p-n junction	1	0.38	350Å	0.1	1.6×10^{-8}	3 M
p - substrate	5	0.012	28μm	2	2×10^{-8}	3 M
PtSi - substrate	6	<0.0006	12μm	2	5×10^{-10}	100 M
n_i - p (hor.)	3	0.048	175Å	2	1×10^{-10}	500 M
n_i - p (vert.)	2	8×10^{-6}	1μm	2	1×10^{-12}	500 M
n_i - PtSi	4	8×10^{-6}	1μm	2	1×10^{-12}	500 M

Table 4.4 Metal Semiconductor Schottky Current.

See Eqn. A.1, A.2, A.3 $R_0 = kT / qI_{so}$ $N_c = 3.2 \times 10^{19} \text{ cm}^{-3}$, $D_n = 34.6 \text{ cm}^2/\text{sec}$

Junction	Path	Area cm ²	N_d cm ⁻³	$q\phi_i$ eV	$I_{ms0}(0)$ A	$\approx R_0$ Ω
PtSi - substrate	6	<0.0006	10^{12}	0.11	3×10^{-11}	10^9
n_i - PtSi	4	8×10^{-6}	10^{15}	0.29	2×10^{-11}	10^9

various current mechanisms, they are discussed in terms of R_0 as given in Eqns. A.10, A.11 and A.12 in Appendix A. The majority of the samples available suffer from the surface contamination discussed in Section 4.1. In these samples, the reverse bias current is via the ohmic contact with the substrate and hence they provide little information about the current transport within the nipi. Some samples are available which may be suitable for investigation of the reverse bias current. Two I-V curves for MBE 360 #1E are shown in Fig. 4.1 and in more detail in Fig. 4.6. For this sample, $R_0 = 1.2 \text{ M}\Omega$ while at higher voltages, the resistance drops to about 500 K Ω .

The reverse bias leakage across the p-n junctions is expected to be high because of the large surface area. Three current mechanisms are considered. The reverse bias saturation current across the p-n junction due to the minority carrier diffusion (Eqn. A.3), given in Table 4.2, Path 1, is too small and does not increase with V_a . Therefore there must be other sources for the leakage current. In the forward bias case, the recombination current was found to be the dominant factor under low bias conditions. The reverse bias equivalent, the generation current, can also be quite large (Eqn. A.7).

Assuming that the n-p junction is fully depleted will give an R_0 of 3 M Ω . Junction breakdown due to both Zener breakdown processes and avalanche processes are possible at high fields. For doping levels on the order 10^{18} cm^{-3} , both processes are expected to occur at field strengths of about 10^6 V/cm [22]. With a well width of 350 \AA , breakdown will occur at an applied bias of about -3.5v. For some samples, the reverse breakdown is observed at about -6.5v with a sharp increase in the current (See Fig. 4.1). The leakage effects described here start

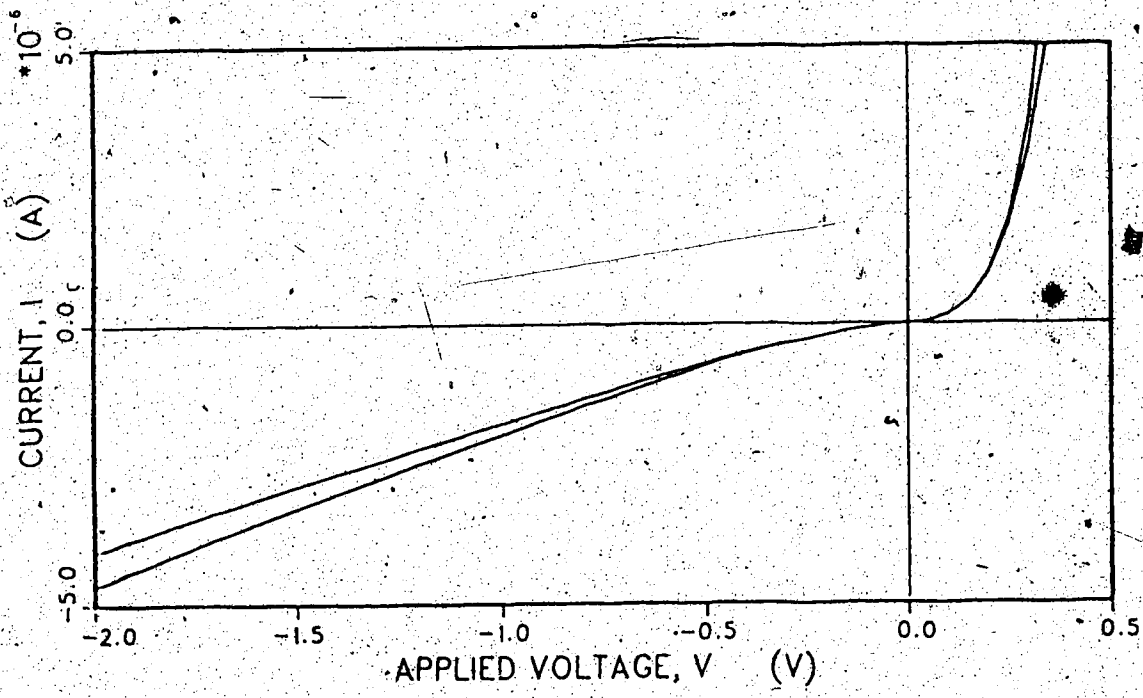


Fig. 4.6 I vs V for MBE 360 # 1E showing low current behavior. (Detail of Fig. 4.1)

at very small voltages and have a slow turn-on. It is therefore unlikely that the leakage is due to a breakdown process.

The second possible route for the reverse bias current is through the n_1 regions incorporated in the mesa edges. The resistance offered by these layers is small (about 2.5K on each side) so any current blocking effects must be due to reverse biased junctions, either metal-semiconductor or p-n. Leakage can occur via any of the three routes shown in Fig. 4.5b. Path 2 is through the graded horizontal junctions on the n-side of the mesa. Path 3 is through the horizontal interfaces. These regions should be fully depleted because of high doping in the p-layers. The current calculations for these two routes are given in Tables 4.2 and 4.3. Path 4 is directly to the PtSi contact. The two current mechanisms are Schottky diode diffusion and carrier generation calculated in Tables 4.4 and 4.3 respectively. In all cases of current transport via the n_1 regions, R_0 is much larger than the observed results and much larger than the other calculations and hence can essentially be ignored. The high blocking provided by these regions demonstrates the advantage of the shadow mask method of providing selective contacts.

Substrate leakage may travel via two routes as shown in Fig. 4.5c. Since the n-type contact is forward biased, current injection into the substrate will occur with relative ease. The current may then re-enter the mesa through the bottom p-layer of the mesa or travel directly into the p-side contact. If the PtSi contact does not form a rectifying barrier, leakage via the substrate to p-contact will be very large as discussed in Section 4.1. Assuming that this problem has been solved, and the Schottky barrier has been restored, there will still be some

reverse bias leakage. The M-S diffusion current is given in Table 4.4, Path 6 and the M-S generation current is given in Table 4.3, Path 6. In both cases, R_0 is much higher than the observed result and the metal substrate interface is not expected to contribute significantly to the reverse bias leakage.

The second substrate route is via the bottom layer of the mesa. Since the first layer grown for the nipi is p-type, there will be a reverse biased p-n junction at the mesa-substrate interface and two leakage mechanisms are possible. The minority carrier diffusion current is still smaller than the observed results ($R_0 \approx 30 \text{ M}\Omega$). However, the generation current is quite large with $R_0 \approx 3 \text{ M}\Omega$ as given in Table 4.3, Path 5. This is due to the combined effect of a large mesa footprint and a wide depletion region in the substrate.

In summary, there are two possible candidates for the dominant reverse bias current, both due to carrier generation. The first is across the p-n junctions (Path 1) and the second is across the mesa-substrate junction (Path 5). In both cases, the magnitude of R_0 agrees with the observed results. These calculations suggest that with this particular sample, the "best case" of lowest possible reverse bias leakage has been attained. It is not possible to ascertain which of the two paths is dominant but it appears that substrate effects in future measurements of nipi properties such as lifetime and photoconductivity may be significant.

4.3 Forward Bias Characteristics

Under forward bias, the current across the nipi will be very large while other associated leakage currents, such as substrate leakage are

expected to be smaller in comparison. Under these circumstances, it should be possible to extract valid diode parameters. In this section, the forward bias results are presented and these are compared with current transport models.

As a first approximation, the ideal diode equation is compared with the nipi diode measurements. The diode current, I_d depends exponentially on the applied voltage, V_a as outlined in Appendix A:

$$I_d = I_s = I_{s0} (\exp(qV_a/kT) - 1) \quad (A.3)$$

with I_{s0} given in Eqn. A.4. This equation can be linearized by plotting $\log(I_d)$ vs V_a for $V_a > 0$ resulting in:

$$\log(I_d) = \log(I_{s0}) + qV_a / kT \ln(10) \quad (4.1)$$

The intercept (extrapolated to $V=0$) will yield the saturation current I_{s0} and the slope of the curve should be $q/kT \cdot \ln(10)$. Fig. 4.7 shows the expected curve (dashed line) as well as a measured result for MBE 360 #1E with I_{s0} fitted to the curve. The value determined for I_{s0} is about 2×10^{-8} A which is much larger than the value predicted from Eqn. A.4 (6×10^{-14} A). The two curves shown in fact seem to have very little in common. Two other factors need to be included in order to obtain a reasonable model of the forward bias current.

The ideal diode equation does not take into account the series resistance that must be included in a real circuit. As the applied bias increases, the depletion region width decreases and the current-limiting factor becomes the bulk resistivity of the nipi. This can be accounted for by including a diode resistance, R_d in series with the ideal diode. The applied voltage V_a in Eqn. A.3 must be replaced

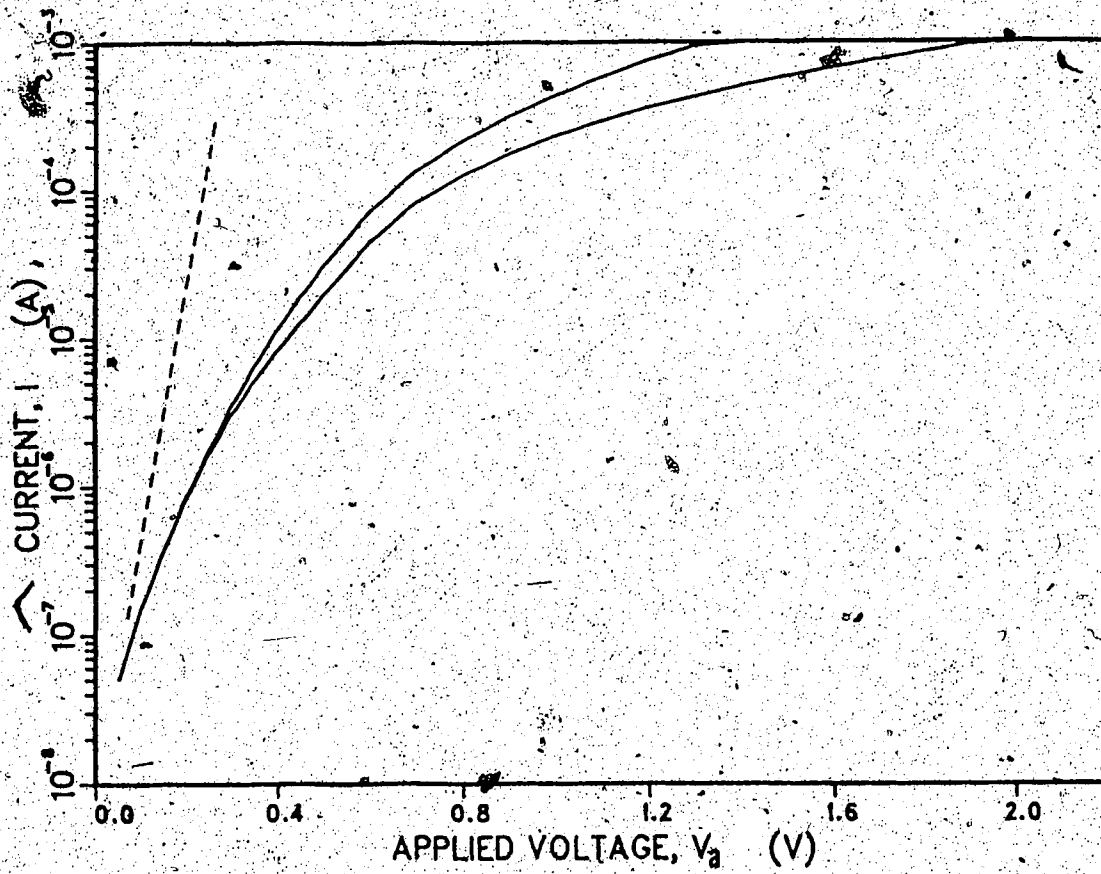


Fig. 4.7 Log(I) vs V_a for MBE 360 #1E.
 Dashed line represents ideal diode model. Curves are shown
 for two measurements across different contact pairs of the
 same split contact nipi mesa.

with the voltage across the diode V_d where $V_d = V_a - R_s I_d$.

The slope of the curve at small bias in Fig. 4.7 indicates that the exponential behavior varies with $q/2kT$ rather than with q/kT as in the ideal diode case. As discussed in Appendix A, this indicates that the recombination current probably dominates. An additional term can be added to the model which accounts for the recombination current in the depletion region:

$$I_r \approx \frac{q n_i x_d}{2r} \exp(qV_d/2kT) \tag{A.6}$$

For small values of V_a , the exponential behavior is expected to vary with $q/2kT$ rather than with q/kT . But as V_d approaches ϕ_i , the depletion width will decrease and the recombination current will drop off. Therefore, it is necessary to include both diode currents as well as the series resistor in the n-p-i diode model:

$$I_d(V_a) = I_r(V_d) + I_s(V_d) \tag{4.2}$$

with

$$V_d = V_a - R_s I_d \tag{4.3}$$

It is not possible to linearize this equation and so an iterative curve fitting approach is used. There are four parameters to be determined:

I_{s0} , R_s , ϕ_i , and I_{r0} . Two of these parameters can be determined from the $I-V$ curve. The junction resistance R_0 (Eqn. A.9) can be determined from the slope of the curve at $V_a = 0v$, and from this I_{s0} is found:

$$I_{s0} = 2kT / qR_0 \tag{A.11}$$

For large V_a , the exponential behavior will disappear and the curve will become linear. The slope of the $I-V$ curve can be used to

determine R_0 . Table 4.5 lists these results for some of the nipi's measured. The diode resistance is expected to be around 300 Ω and will vary depending on the sample position on the wafer and the mesa width. For the majority of cases, the values of R_0 are too low because of the substrate leakage that has been described in Section 4.1, and the values of I_{r0} determined from these low R_0 are probably not correct.

Under very low forward bias conditions, only the recombination current is expected to contribute to the diode current and the other diode parameters can be ignored. In the previous section, the reverse bias characteristics were found to depend on a generation current. However, it was not possible to determine through which junction, (the substrate-mesa interface or the p-n junctions of the nipi), this current flows. These two current models have been "fit" with the results for MBE 360 #1E as shown in Fig. 4.8. The curve for the substrate generation current (Path 5 of Fig. 4.5) fits the measured current very closely. The model for the nipi generation current (Path 1 of Fig. 4.5) cannot be made to fit any better than shown because of the larger slope. In both cases the same value has been used for I_{r0} . The series resistance for the substrate current is much higher than for the nipi and this has resulted in the better fit. For this particular sample, it appears that the dominant current is due to carrier generation in the substrate. Lack of more samples with a high R_0 has restricted the continuation of this investigation at present. This tentative conclusion is based on an empirical curve fit and hence from here we can work backwards to determine the effective lifetime τ for the FZ substrate. From Eqn. A.13, τ is found to be 1.3 μsec which agrees closely with the approximation given in Appendix A.

Table 4.5 Forward Bias Results for Nipi Diodes.

MBE Sample	R (V _s =0v)	I ₀	R _a	qφ _i
360 #4B	20K Ω	1.3E-6 A	160 Ω	0.5 eV
	20K	0.9E-6	360	0.8
360 #1E	1.1M	2.4E-8	400	0.6
	1.1M	4E-8	1000*	
360 #1E 77°K	200K		360	0.8
360 #3A	100K	2.6E-7	160	0.5
	150K	1.6E-7	260	0.5
360 #3A 77°K	150K	5.0E-8		0.7
	500K	1.6E-7		0.9
391 #3B	5K	5.2E-6	500	0.5
391 #5E (very leaky)	10K	2.6E-6	80	0.9
404	20K	1.3E-6	3000*	0.6
405 #3A	250K	1.0E-7	600*	0.6
318	30K		100	0.5
368 #1A			600	

* R_a may be lower than the value given.

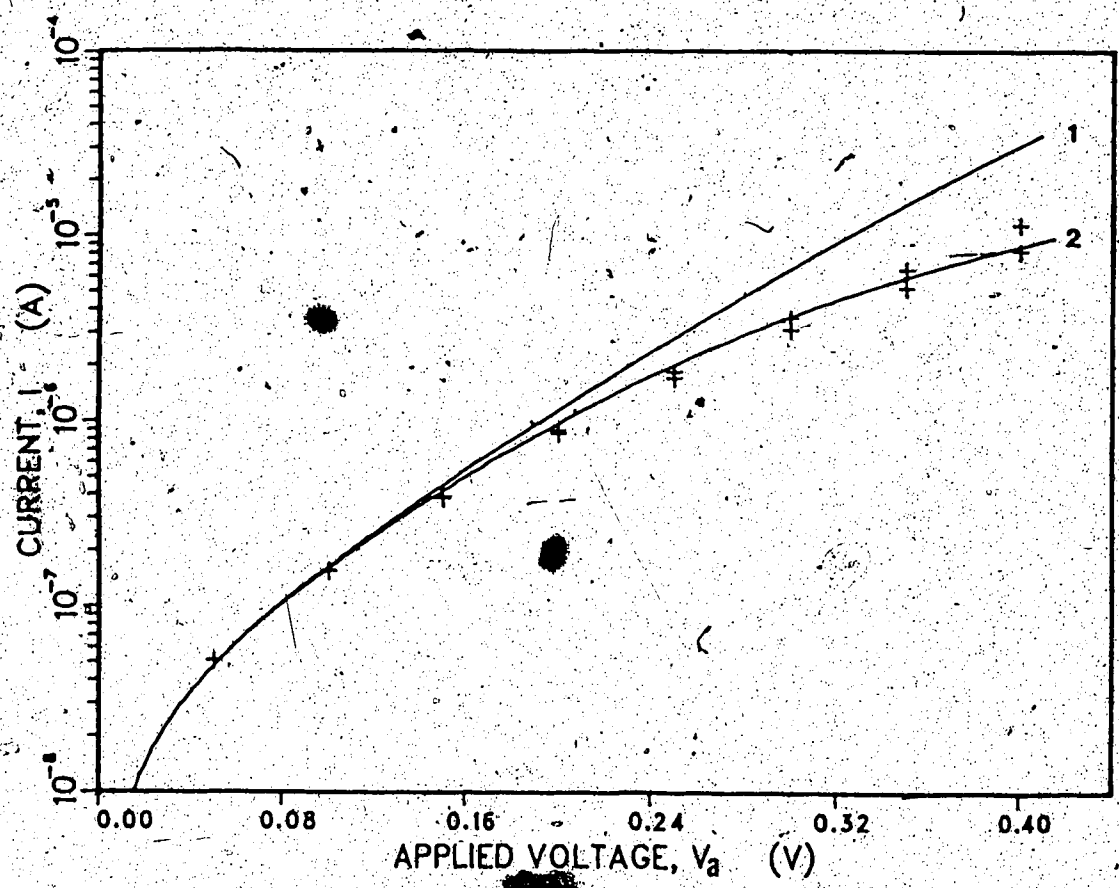


Fig. 4.8 MBE 360 #1E I-V curve at low forward bias.
Measured data points indicated by '+'.
Curve #1 represents recombination in the nipi.
Curve #2 represents recombination in the substrate.

At larger values of forward bias, substrate effects will not contribute significantly because of the large series resistance. In this situation, the ideal diode equation can be fitted to the measured I-V data. Although there may be other contributions to the diode current, such a comparison should at least yield an upper bound on I_{s0} . If the expected value of I_{s0} is used, the ideal diode model predicts a current that is too large as shown in Fig. 4.9a. In order to obtain a reasonable fit, the value of I_{s0} must be reduced to 1×10^{-18} A as shown in Fig. 4.9b. Curve fitting at large forward bias can also be done in the case of the leaky diodes. In Fig. 4.10, where MBE 360 #4B has been used, the value required for I_{s0} is still lower than the estimated value. From Eqn. A.4, there are two parameters which may be related to the lower value of I_{s0} , the junction area A , and the diffusion length, L_n and L_p . It is possible that the entire width of the mesa is not being utilized in the current transport resulting in a smaller effective area. As well, the narrow layers may contribute to a much longer diffusion length. The reason for the lower values for I_{s0} has not been determined as yet.

Investigation of the forward bias behavior of the nipi has revealed some characteristics of silicon doping superlattices. The I-V behavior with low bias follows a $2kT/q$ exponential behavior. Under low forward bias conditions, the dominant current mechanism is found to be the substrate-mesa generation current. This implies that the substrate must also be playing a large part in the reverse bias currents. The large distance between the contacts results in ohmic losses across the diode that are not negligible. As well, the saturation current is smaller than predicted by the ideal diode model. The number of

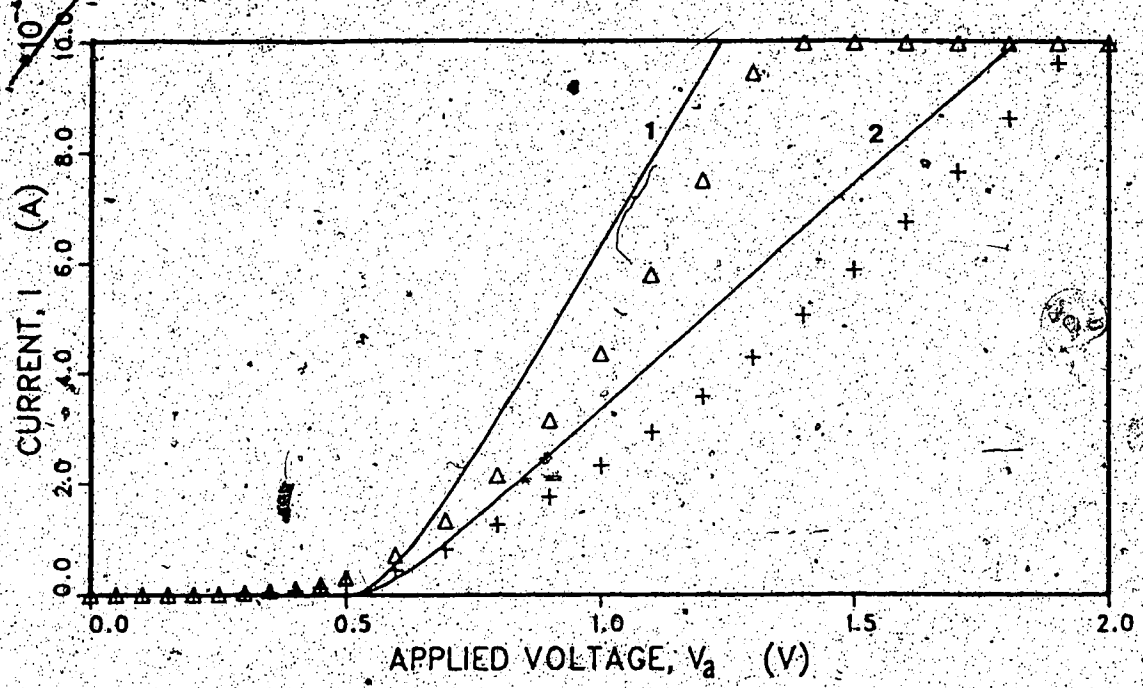


Fig. 4.9a MBE 360 #1E I-V curve for large forward bias.
 Points are data collected from split contact nipi.
 Curves represent ideal diode model with $I_{s0} = 3 \times 10^{-14}$ A.
 Curve #1 is for $R_d = 600 \Omega$ (Δ - measured data).
 Curve #2 is for $R_d = 1180 \Omega$ (+ - measured data).

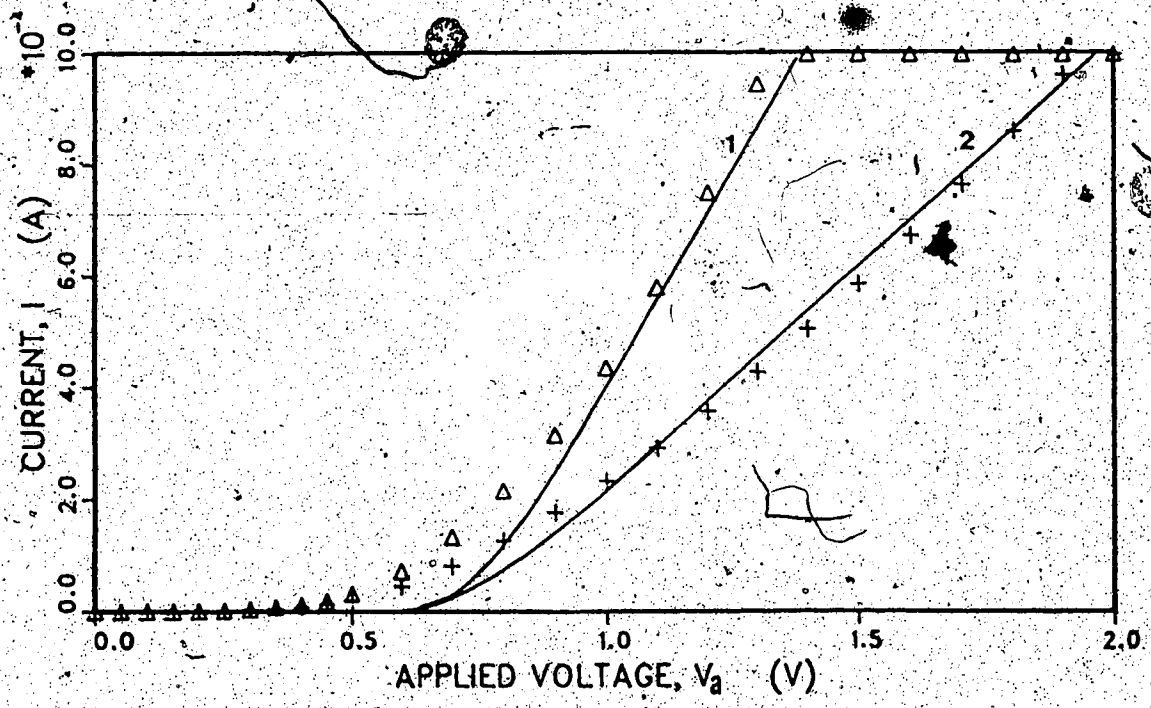


Fig. 4.9b Same as Fig. 4.9a except with $I_{s0} = 1 \times 10^{-16}$ A.

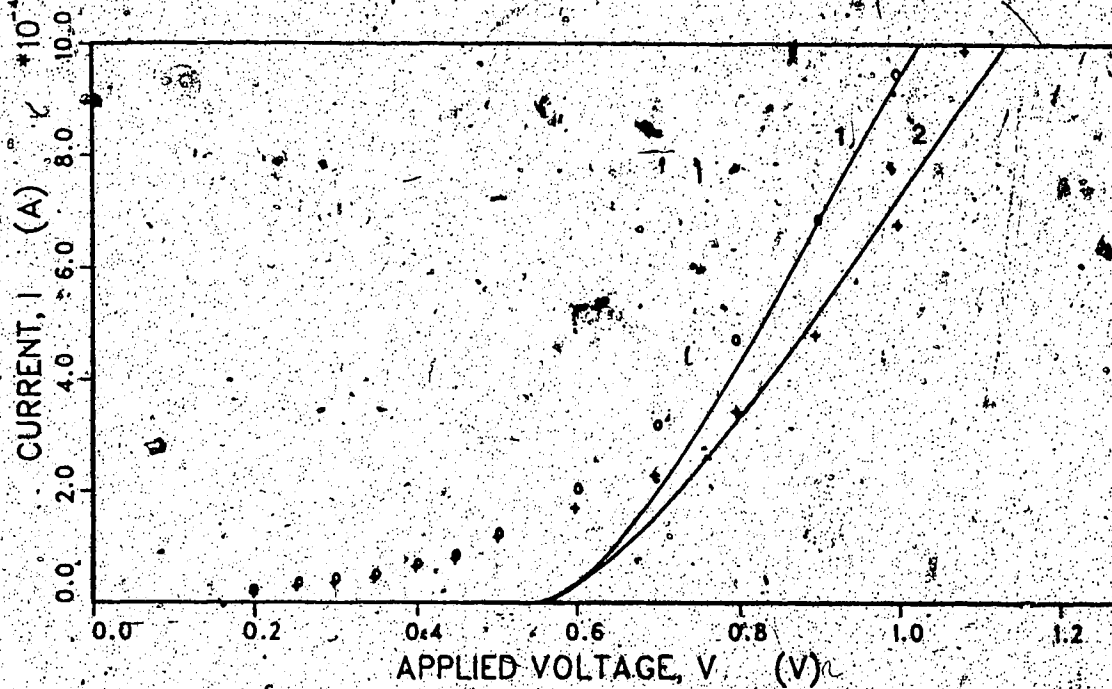


Fig. 4.10 MBE 360 #4B I-V curve for large forward bias.
 Points are data collected for two nipi's.
 Curves represent ideal diode model, with $I_{s0} = 5 \times 10^{-14}$ A.
 Curve #1 is for $R_d = 350 \Omega$. (o - measured data)
 Curve #2 is for $R_d = 450 \Omega$. (+ - measured data)
 Only the ideal diode current term of Eqn. 4.2 is included here. This model represents an upper bound on the current.

available samples was limited and more testing is needed to verify these observations.

4.4 Transconductance

Many of the tunable properties of the nipi, in particular the tunable absorption require the ability to vary electric field and hence the potential across the p-n junction. The range of the variation can be calculated indirectly in the nipi by measuring the conductance of the n and p type layers. In this section the transconductance measurements are presented.

Split contacts have been added to some of the mesas in order to measure the transconductance. A small voltage is applied across the split contacts and the current flow across them is measured as shown in Fig. 4.11. From the I-V curve, the conductance between the split contacts in either the p or n layers can be calculated. Because of the etched notch, the current will travel through the central p-n-p-n region of the mesa.

The nipi can be considered as a multilayered junction FET where the two split contacts represent the source and drain electrodes as shown in Fig. 4.12a. If the p-side split contacts are used then the p-type layers act as the channel and the n-type layers operate as the two gates (tied together). For the measurement performed here, the voltage across the split contact is kept small so the device is always being operated below saturation. (See Fig. 4.12b.) The width of the depletion region is not expected to vary along the length of the channel due to the small voltages applied. The term transconductance is then similar to the FET parameter, mutual transconductance, g_m . In

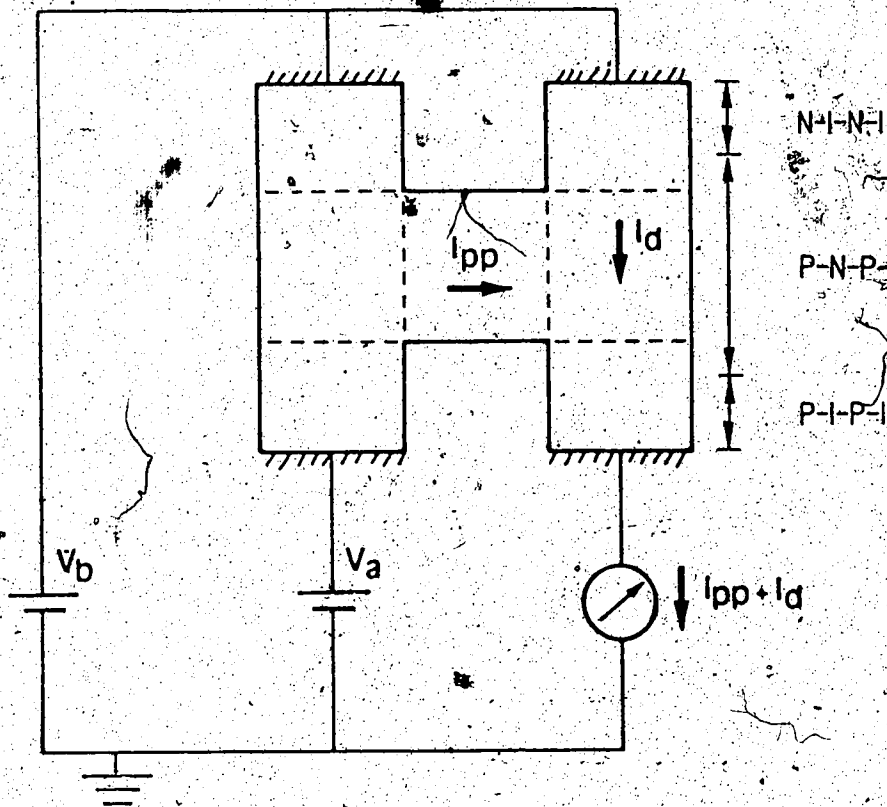


Fig. 4.11 Circuit setup for transconductance measurements.
 The path length for I_{pp} will be about $\frac{3}{4} + \frac{2}{3} + 1 + \frac{2}{3} + \frac{3}{4} \approx 3.8$ \square 's with the path length around a corner taken as $\frac{2}{3}$ of a square [22].

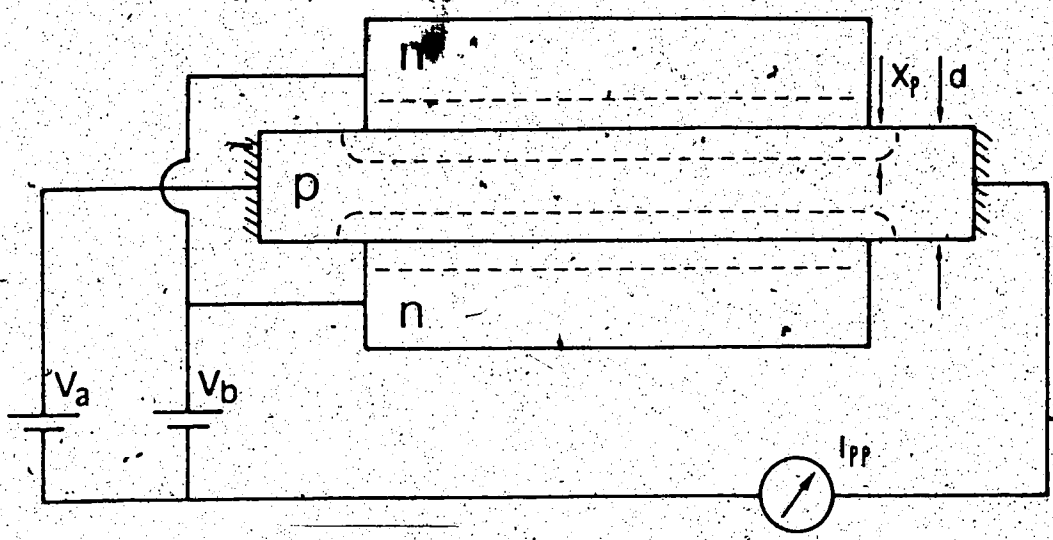


Fig. 4.12a Cross-sectional view of transconductance measurement across split contacts. Figure is drawn to show similarity with a FET. Dashed lines represent limits of the depletion region. The "channel" length is about 1 mm.

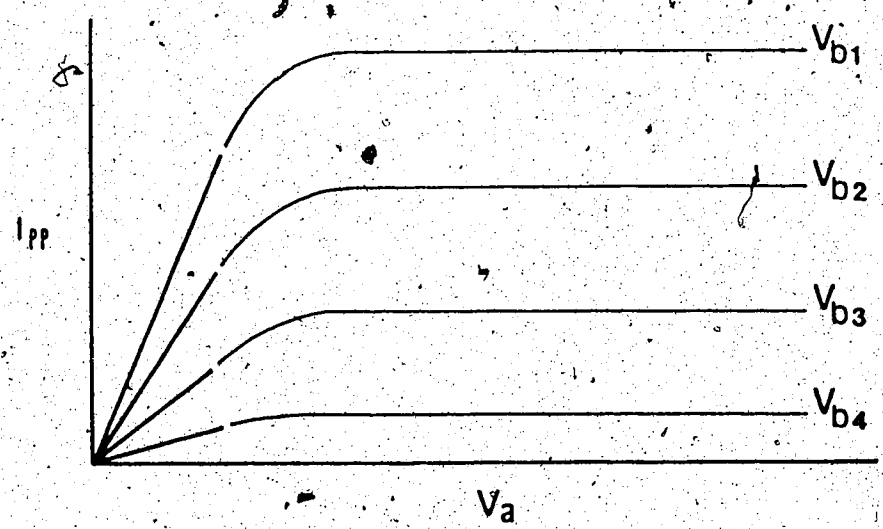


Fig. 4.12b Typical I vs V characteristics for a FET. The bold lines correspond to the region where the transconductance measurements are made.

the case of very narrow layers, this comparison will no longer be true. This thesis considers only nipi's with wider layer widths.

The current transport in each layer is restricted by the width of the depletion region. As the bias across the nipi diode changes, the width of the depletion region in each layer will vary and hence the conductance will vary with the amount of external bias. At some value of reverse bias in the nipi diode, the depletion region will extend across the entire layer (full depletion) and the conductance should drop to zero. When a forward bias is applied, the depletion region will reduce in width and a maximum value for the conductance should be reached.

The value of the maximum conductance, G_0 , when the depletion width is zero can be calculated by approximating the current path between the split contacts: $L \approx 3.8 \mu\text{s}$. (See Fig. 4.11.) The resistance between the split contacts will be: $R_s = \rho \times L / T$. Letting $\rho = 0.02 \Omega\text{-cm}$ for $N_d = 2 \times 10^{18} \text{cm}^{-3}$ [22] with $T = 350 \text{\AA} \times 20$ layers gives $R_s = 1 \text{K}\Omega$ and $G_0 = 1 \text{mS}$ for MBE 360. However, the maximum observable value will be much smaller since under the forward bias conditions needed to reduce depletion region width, the large diode current obscures the split contact current. For example, the largest value of G_m observed for GaAs is about $1/3 G_0$ at a forward bias of 0.4V [15]. The samples available for transconductance measurements have been designed to optimize some of the expected optical properties, namely, they were designed to be fully depleted at zero bias. Hence the variation in the transconductance is expected to be limited.

The conductance will depend on the cross-sectional area available for current transport. In the case of uniform doping with abrupt

junctions, the conductance G will be proportional to the width of the undepleted region:

$$G_{pp} = G_o (1 - 2 x_p / d) \tag{4.4}$$

where d is the layer width and x_p is the width of the depletion region in the p-type layer:

$$x_p = \sqrt{\frac{2\epsilon}{q} \frac{(\phi_i - V_b)}{(N_a + N_d)} \frac{N_d}{N_a}} \tag{4.5}$$

The diode bias at which the layer will be fully depleted is found by substituting x_p = d/2 giving:

$$V_o = \phi_i - \frac{q}{2\epsilon} \frac{N_a}{N_d} (N_a + N_d) (d/2)^2 \tag{4.6}$$

$$\text{and } G_{pp} = G_o \left[1 - \sqrt{\frac{(\phi_i - V_b)}{(\phi_i - V_o)}} \right] \tag{4.7}$$

The maximum value of G_{pp} will occur when V_b = φ_i. For the case of varying ρ(x) across the layer, the value of G_{pp} will be less than in the uniform doping case.

With a fixed value of the diode voltage, the current is measured over a small range of the split contact voltage V_s. The voltage is kept small in order to avoid disturbing the bias across the nipi diode. The set of I-V_s curves for MBE 360 #4B are shown in Fig. 4.13a. Ideally the curves should pass through the origin but the measured current consists of two components: the split contact current I_{pp} due to V_s and the diode current I_d due to V_b (Fig. 4.11). The contribution from the diode current will be large under forward bias and, as has been discussed, the reverse bias current for the nipi diode will also be quite substantial.

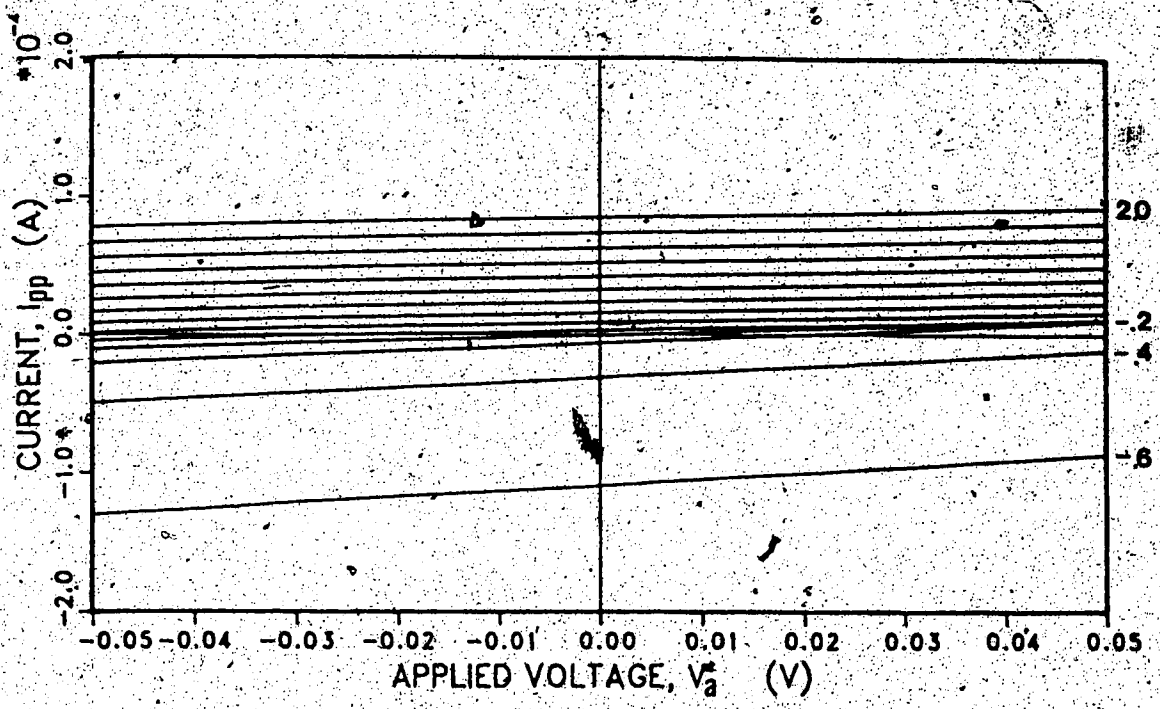


Fig. 4.13a Set of I-V curves collected across the split contacts. Measurements are for the p-type layers from MBE 360 #4B. The diode bias V_b ranges from -0.6v to 2.0v in steps of 0.2v.

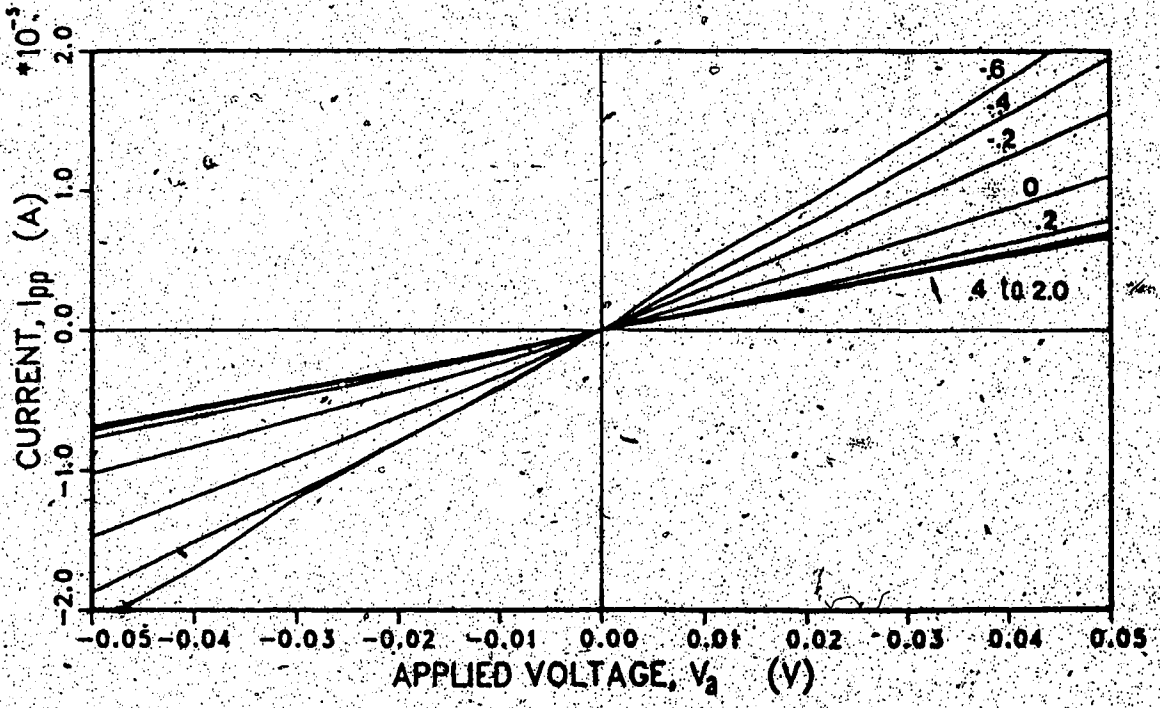


Fig. 4.13b I-V curves of Fig. 4.13a with offset removed.

Since the conductance is measured from the slope of the I-V curves, the offset does not cause a problem. Fig. 4.13b shows the same set of curves centered on the origin (offset removed) and the variation in the conductance with V_b becomes evident. However, as a larger reverse bias is applied, the slopes do not reduce to zero but approach a background level. This can also be seen in a plot of G_{pp} vs V_b shown in Fig. 4.14a. The background conductance appears to be independent of the applied bias. The magnitude of the background level is very large in comparison to the range of G_{pp} . Similar results are shown in Fig. 4.14b for magnesium contacts on the n-side of MBE 360 #4B.

The background level appears to depend on the doping with the higher doped layers having a larger background. Measurements of the background levels for some samples are given in Table 4.6. For the MBE 360 samples, the doping concentration and background appear to be related. This is also substantiated by the background measurements for MBE 404 and 405 which have both higher doping and wider wells. The background conductance is not expected to be due to the substrate because of the much higher resistance. This is partially confirmed by the results for MBE 404 and 405 which were grown on different substrates (CZ and FZ substrates respectively) and yet have a similar background level. As well, MBE 404 and 405 have been processed with the surface etch and show a higher background than those such as MBE 360 #4B which were not etched.

Although V_a is kept small, the diode current is a function of V_a as well as V_b . The affect of V_a on the diode current can be approximated from the diode conductance, $G_d = (\partial I / \partial V)$. Under reverse bias conditions, G_d is much smaller than G_{pp} but as the diode turns on

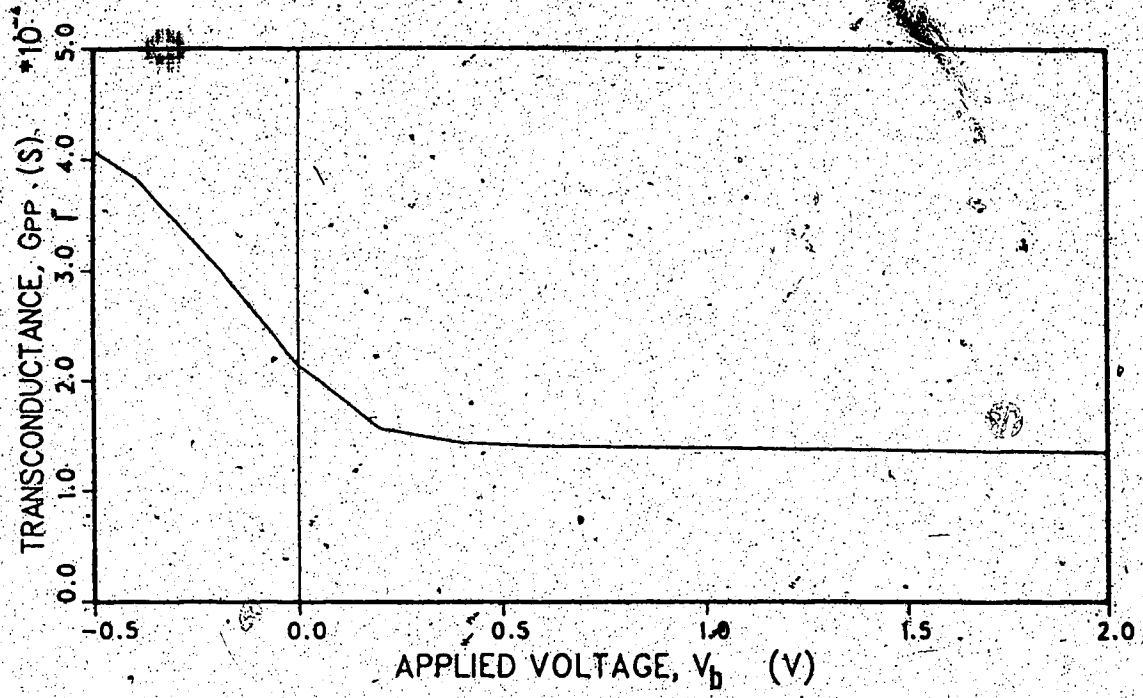


Fig. 4.14a Transconductance G_{pp} for MBE 360 #4B.

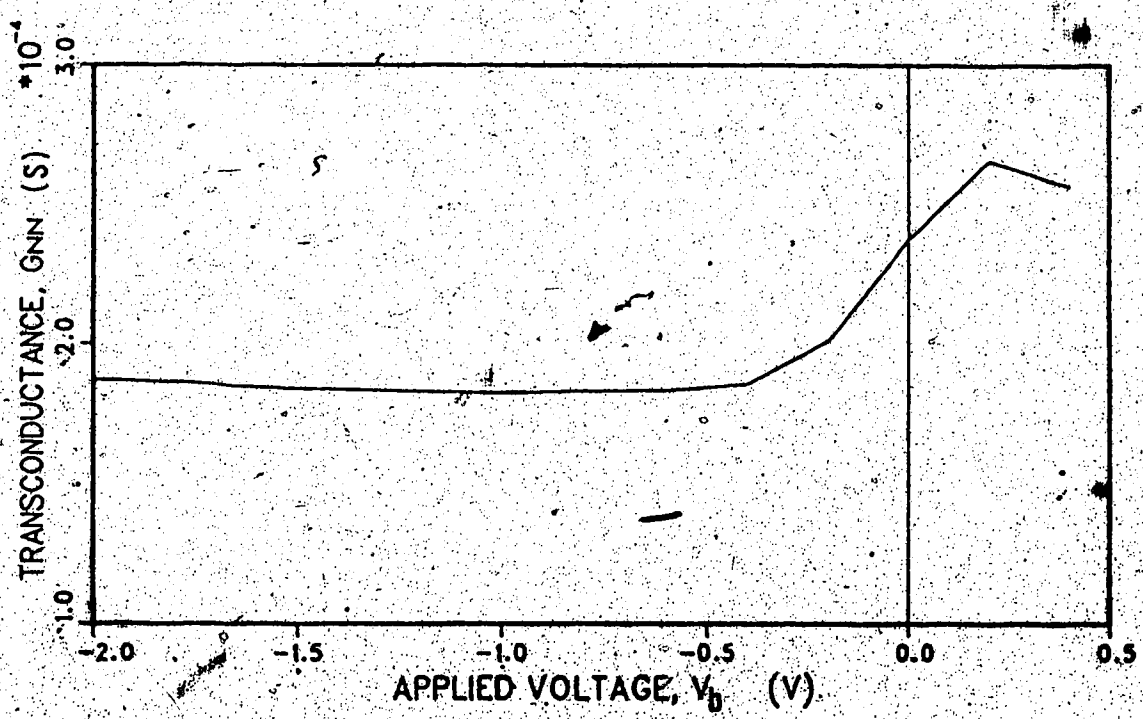


Fig. 4.14b Transconductance G_{nn} for MBE 360 #4B.

G_d increases rapidly and becomes much larger than G_{pp} . For the case of the p layers, the diode current tends to increase the value of G_{pp} and a sharp change in slope is observed. For the n-layers, the diode current tends to reduce G_{nn} and the curve turns over as shown in Fig. 4.14b. This provides a cutoff point for the conductance curves under forward-bias.

Table 4.6 Transconductance Background Levels:

MBE Sample:	G_{pp}	G_{nn}	N_a	N_d
	mS	mS		
360 #4B	0.18	0.12	high	low
360 #4B TAG	0.14	0.18	↑	↓
360 #3A	0.1	0.4	↑	↓
360 #1E	0.02	0.4	low	high
404 #3A	0.85			
405 #	0.8			

Chapter 5

Optical Characteristics

One of the first projects undertaken in this thesis was the theoretical calculation of the tunable absorption in a silicon doping superlattice. Similar calculations have been done previously for a direct bandgap material [12] but this is the first time the tunable absorption has been calculated for an indirect bandgap superlattice. Section 5.1 describes these calculations including details of the phonon interaction. Estimates for the expected shift in the absorption edge are presented for both room temperature and 77°K. (A version of Section 5.1 has been accepted for publication. See Ref. 11)

Measurements of the photoconductivity in a nipi were carried out in order to observe the shift in the absorption. However preliminary results have not displayed the expected shift. These results are presented in Section 5.2 along with a discussion of problems encountered.

5.1 Modelling of Nipi Absorption

The energy band diagram for a doping superlattice under equilibrium conditions is shown in Fig. 5.1. The energy bandgap in a doping superlattice remains constant, but the edges of the conduction and valence bands are modulated in the direction perpendicular to the superlattice period. This periodic modulation energy gap results in an effective bandgap E^{eff} which may be tuned by varying the electron and hole concentrations with external biasing [29]. The optical absorption at energies near and below the bandgap energy will be affected by the internal electric field associated with this modulated band structure.

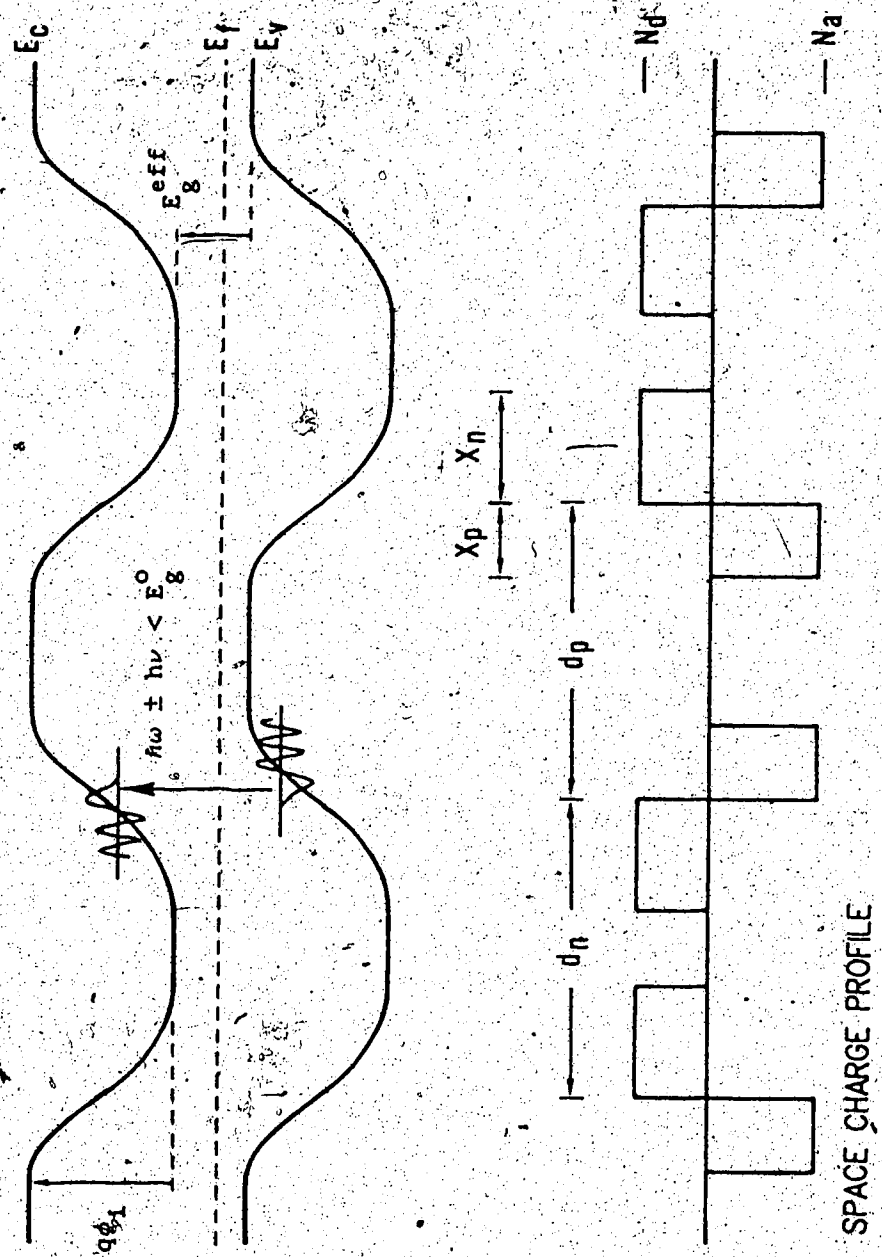


Fig. 5.1 Energy band diagram for a silicon doping superlattice. Also shown is the space charge distribution. Equilibrium conditions without full depletion are depicted.

Optical absorption beyond the fundamental edge in doping superlattices has mainly been studied in direct bandgap materials, particularly, GaAs [12,30]. As a first step in the study of indirect bandgap superlattices, we have calculated the optical absorption in a silicon doping superlattice, with moderate layer thicknesses at room temperature and at 77°K. Because of the indirect bandgap structure of silicon, the absorption must be accompanied by the creation or annihilation of a phonon. Another complicating factor is the multi-valley band structure of silicon.

Rather than compute the space-charge distribution self-consistently, the depletion approximation is used, which simplifies the solution of Poisson's equation. This approximation holds except within a few Debye lengths of the edges of the space charge regions [22]. For case considered here, the Debye length is less than 10% of the depletion length at the maximum reverse external bias. The layer thicknesses are kept large enough that any sub-band effects resulting from the quantization of the motion in the direction perpendicular to the layers may be ignored. The equations for the periodic space charge potential and the 2-dimensional carrier densities have been given in Ref. 12 and will not be repeated here. The doping concentrations N_A and N_D are assumed to be constant with abrupt interfaces. Because the charge density in each case is piecewise constant, the electric fields are piecewise linear and continuous and the electric potentials are piecewise quadratic and continuous.

The absorption will depend on both the extent of the depletion in one period and upon the strength of the internal field. In order to optimize conditions for each case considered, we have assumed that

$N_d d_n = N_a d_p$ and also that the maximum allowed field is obtained at full depletion. The maximum allowed internal field \mathcal{E}_{\max} has been arbitrarily chosen as one-half the breakdown field which is determined by the doping concentration [23]. Under these conditions, the maximum depth of the space charge potential will be:

$$\Delta V_{\max} = \mathcal{E}_{\max}^2 \frac{\epsilon}{2q} \left(\frac{1}{N_a} + \frac{1}{N_d} \right) \quad (5.1)$$

The depth of the potential may be changed by varying the space charge distribution either by optical excitation or the application of an external bias. The layers are assumed to be contacted selectively and hence the field will be directly across the layers. Assuming that the Fermi energies of the electrons and holes remain fixed with respect to the band edges at the centres of their potential wells [8], the maximum space charge potential and the external bias V_{ext} are related by

$$\Delta V_{\max} = \varphi_i - V_{\text{ext}} \quad (5.2)$$

where φ_i is the built-in potential. Depending on the design parameters, a strong internal field may exist when $V_{\text{ext}} = 0.0\text{v}$ and which may be increased or decreased with the appropriate external bias.

Optical absorption at energies less than the fundamental edge in a semiconductor under the influence of an electric field is possible due to the Franz-Keldysh effect [31]. The theory of direct transitions in the presence of uniform electric fields [32] has been used for the calculation of optical absorption in GaAs doping superlattices [12].

The wave function envelopes in a constant electric field are Airy functions and the absorption coefficient may be calculated numerically.

For silicon, the calculation is similar but more complicated due to its

indirect (in k -space) band structure. However, the theory of phonon-assisted optical absorption has been described by Penchina [33] for cases in which the effective mass approximation is valid. The contribution from bound exciton states is not considered to be important and is ignored here [34].

The optical absorption coefficient for each phonon branch is given by [33]:

$$\alpha(\nu) = W_{\pm} (16/3\pi) \theta_F^2 \int_{V_{0\pm}}^{\infty} (V - V_{0\pm})^{3/2} |A_1(V)|^2 dV. \quad (5.3)$$

where

$$V_{0\pm} = (E_g - h\nu \pm h\nu_p) / \hbar\theta_F. \quad (5.4)$$

The photon energy is $h\nu$, the phonon energy is $h\nu_p$, the \pm indicates the emission or absorption of the phonon in the absorption process, and $\hbar\theta_F$ is an energy scaling factor proportional to the two-thirds power of the electric field, F . The quantity W_{\pm} is a weighting factor which depends on the electron and hole effective masses, the photon energy and the equilibrium phonon distribution.

In order to calculate the total absorption, Eqn. 5.3 is summed over the various contributing factors including (a) the reduced effective masses for holes, (b) the reduced effective masses for electrons, (c) emission and absorption processes, and (d) all contributing phonon branches. The integral is calculated numerically and the result is normalized using a known result for the absorption for zero field and $h\nu = 1.1$ eV [35].

The calculations were carried out for a field in the (100) direction and hence the electron reduced effective masses include the

two directions which involve the longitudinal reduced effective mass and the four directions which involve the transverse reduced effective mass. The (isotropic) reduced effective masses for the holes include contributions from the light and heavy holes. The split-off hole has not been included in the calculations as its contribution has not been observable in experimental results [36,37]. All four phonon branches (TA, TO, LA, LO) with energies of 18.2, 57.7, 41.4 and 51.3 meV respectively [36,38] have been included. The probability of a particular phonon branch participating in the transition process is proportional to the phonon density as given by Bose-Einstein statistics [39]. As well, experimental results [36,37] indicate that in addition to population factors, the phonon branches participate with different probabilities. MacFarlane et al. [37] found that (after accounting for phonon population factors) the coupling of the electrons to the 58 meV phonon branch is about 5.5 times stronger than to the 18 meV phonon branch. By including this factor in the calculations, we produce results that are close to the differential electro-absorption measurements of Frova et al. [36]. (Calculations for this comparison were performed with the field in the (111) direction). The differences may be due to excitonic effects, thermal broadening and limited information on the coupling ratio of the phonon branches.

For a doped superlattice, the internal fields are not constant due to the quadratic behavior of the potential. When the scale-length of the variation of the internal electric potential is larger than the effective range of the wavefunctions, the electric field may be considered to be constant in the regions in which transitions occur. The absorption coefficient for the superlattice is found by averaging

the absorption coefficient for the constant field case $\alpha(\nu, F)$ over one period. With the slow variation of the electric field from the linear approximation, the difference between the wave envelope functions and the Airy functions is expected to be negligible. A larger source of error is due to the uncertainty in the assumed starting point of the integration, V_0 , in Eqn. 5.3 which depends on the field strength, F . For the range of photon energies considered here, the resulting uncertainty in the absorption coefficient is less than 10% and is highest at the low photon energy end.

The average absorption coefficient at room temperature and at 77°K are given in Figs. 5.2 and 5.3. Several values of the external bias were used in each case, the maximum value being limited by the condition that the electric field is no more than one-half the breakdown field at any point in the superlattice. The effect of lowering the temperature is to shift the absorption curves to higher photon energy, or shorter wavelengths, away from the technologically interesting region of 1.3 μ m or 0.95eV. The results indicate that maximum absorption is achievable with modest external biases and that the absorption, although small, is tunable over orders of magnitude.

On the surface, it appears that the superlattice is on the verge of being useful for device fabrication. However, a process not mentioned so far is impurity absorption, the optical excitation of electrons into the empty states of the donor atoms. The impurity absorption coefficient for small $h\nu$ is very nearly proportional to the impurity concentration and is characterized by a minimum in the absorption spectrum in the range 1.2-1.5 μ m [39,40]. At room temperature and for doping concentrations typical of those assumed

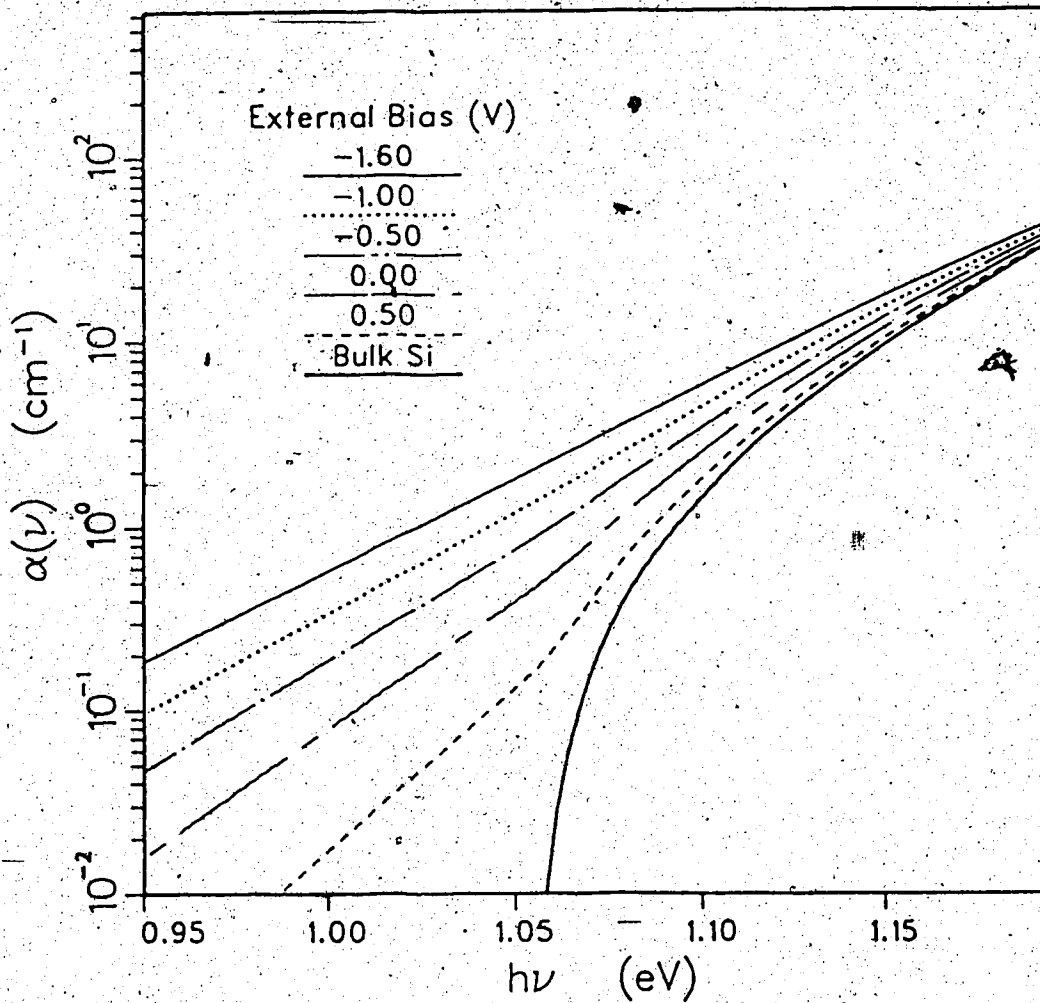


Fig. 5.2 Optical absorption coefficient vs photon energy at $T=300^\circ\text{K}$.

$N_a = N_d = 2.5 \times 10^{18} \text{ cm}^{-3}$, $n_n = d_p = 520 \text{ \AA}$.

The external bias voltages of 0.5, 0, -0.5, -1.0 and -1.6 v correspond to internal fields of 20, 40, 60, 80 and 100 $\text{V}/\mu\text{m}$ respectively.

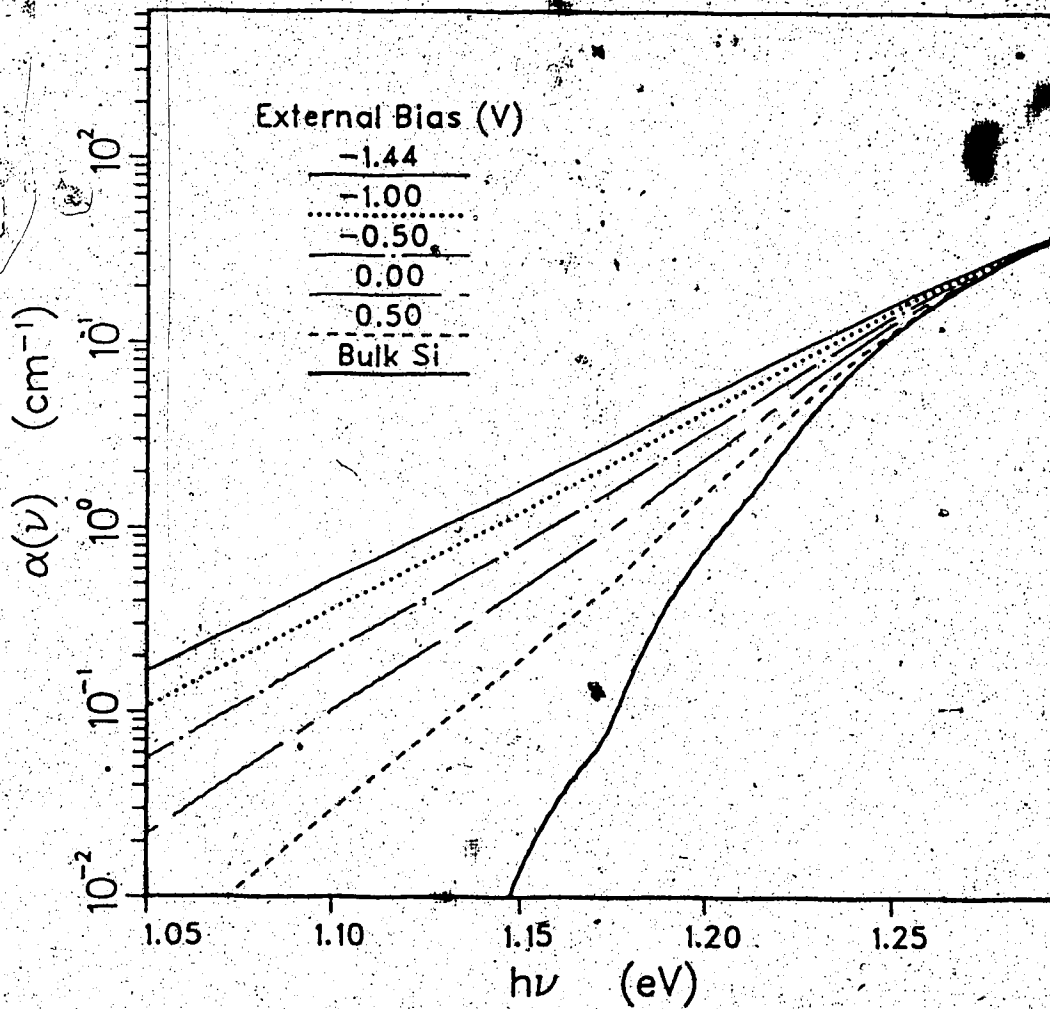


Fig. 5.3 Optical absorption coefficient vs photon energy at $T=77^\circ$. Same parameters as in Fig. 5.2. The external bias voltages of 0.5, 0.0, -0.5, 1.0 and -1.44 correspond to internal fields of 20, 40, 60, 80 and 100 $\text{V}/\mu\text{m}$ respectively.

here, the work of Spitzer and Fan [40] suggests an impurity absorption of at least 2cm^{-1} , an amount which swamps the largest Franz-Keldysh absorption calculated in this paper (Fig. 5.2) for wavelengths greater than $1.2\mu\text{m}$. A device based on the tunability of the absorption should have a coefficient much greater than the impurity coefficient. This is desirable in any event so that the devices remain small and have a fast response. In conclusion, it appears that silicon doping superlattices with moderate to large layer thicknesses can exhibit a small, but measurable, tunable absorption coefficient.

5.2 Photoconductivity Measurements

Preliminary measurements of the n_{ip} absorption have been made indirectly through photoconductivity measurements. The experimental method and the initial results are presented in this section, however, the predicted shift in the absorption has not been observed with these measurements. The major complications associated with the photoconductivity measurements and possible solutions are also discussed.

The absorption spectrum may be found indirectly by measuring the photoconductive current in the n or p-type layers through the split contacts. The relationship between the absorption coefficient and the photoconductive current may be derived in the following manner. From the equation for the drift current, the photoexcited current is found to be:

$$\Delta I = A q u_n \Delta n \mathcal{E} \quad (5.5)$$

where Δn is the number of electron-hole pairs per unit volume created by illumination and \mathcal{E} is the internal field. But,

$$\Delta n = G \tau \quad (5.6)$$

where τ is the excess carrier lifetime and G is the generation rate of electron-hole pairs per unit volume, with

$$G = P_0/h\nu \eta (1 - e^{-\alpha d}) \quad (5.7)$$

where $P_0/h\nu$ is the number of incident photons per second, η is the quantum efficiency and α is the absorption coefficient. Hence

$$\Delta I = A q u_n P_0/h\nu \eta (1 - e^{-\alpha d}) \tau \mathcal{E} \quad (5.8)$$

and in the case of small absorption:

$$\Delta I = A q u_n P_0/h\nu \eta \alpha d \mathcal{E} \tau \quad (5.9)$$

The absorption coefficient α is thus proportional to the change in the photocurrent ΔI . The magnitude of $\alpha(\nu)$ cannot be easily obtained from this measurement but the photocurrent can be scaled to represent the absorption. At higher photon energies, $\alpha(\omega)$ is independent of the internal field and can be approximated by the bulk value. The absorption coefficient is expected to follow:

$$\alpha(\nu, \mathcal{E}) = \alpha(\nu_1) \Delta I_{pp}(\nu, \mathcal{E}) / \Delta I_{pp}(\nu_1) \times \nu / \nu_1 \quad (5.10)$$

where $h\nu_1 \gg E_g^0$. For these measurements, $h\nu_1 = 1.2\text{eV}$ at room temperature and $h\nu_1 = 1.25\text{eV}$ at 77°K .

The method for measuring the photoconductive current is similar to that used for the transconductance measurements. The measurement setup is shown in Fig. 5.4 with a detail of the nipi shown in Fig. 5.4a. A voltage V_b across the nipi is used to control the bias and hence the potential across the layers. A small voltage V_a is applied across the split contacts and the photocurrent in the p-type layers can be measured. The photocurrent is measured via a resistor using a lock-in amplifier (LIA). The signal is further conditioned with an integrator before being sent to the computer. The light is passed through a

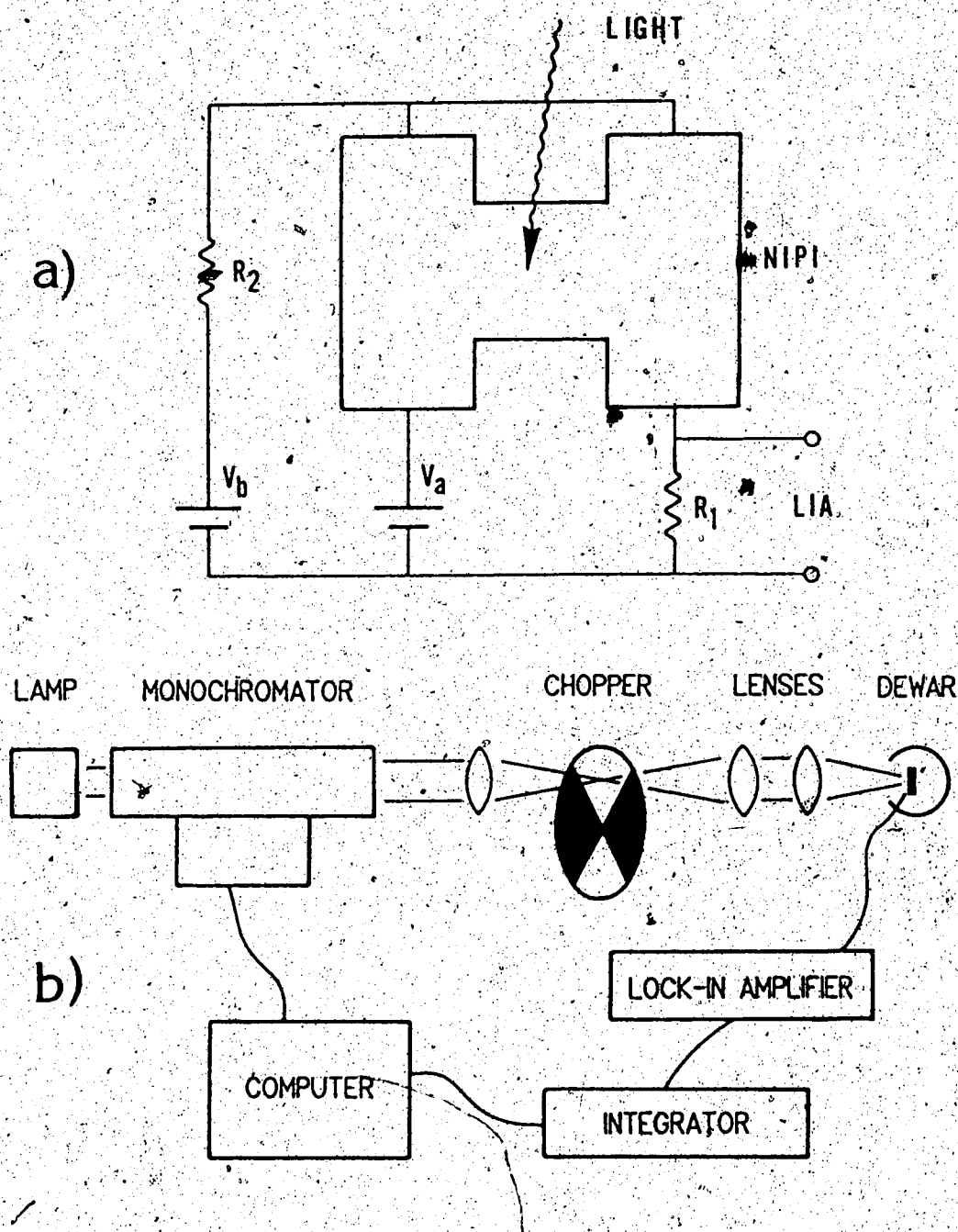


Fig. 5.4 Measurement setup for photoconductivity.
 a) Detail of electrical circuit for split contact nipi.
 R_1 was typically $1\text{k}\Omega$, R_2 was varied from 0 to $10\text{M}\Omega$.
 b) Equipment arrangement with nipi mounted in the dewar.

monochromator and a chopper before being focussed on the mesa. The nipi is mounted in a dewar so that low temperature measurements could be taken as well. The monochromator is also controlled by the computer via a stepper motor so the spectra can be collected automatically. Later on, the voltage sources were put under computer control so that the split contact bias and the diode bias could also be varied during a run. The lamp intensity has been factored out of the absorption curves which follow. Measurements were also made of the substrate absorption using the substrate contacts. The absorption in the substrate, shown in Fig. 5.5, may be compared with the calculated bulk value, shown in Fig. 5.2. However, this curve is also typical of the absorption curves collected for the nipi. A typical curve for the nipi absorption is shown in Fig. 5.6. The photocurrent for the nipi does not differ substantially from the substrate results. This is essentially true for all variations tried for diode voltage, split contact voltage, and resistor values. In the measurements performed to date, the expected shift in the absorption has not been observed. This is also the case for low temperature measurements. A typical result for the photocurrent at low temperature is shown in Fig. 5.7. The observed photoconductance is essentially due to bulk silicon only. Two major factors have contributed to the dominance of the bulk behavior.

(1) Substrate absorption may make up a substantial portion of the observed photocurrent. The absorption curves that are observed for the nipi are similar to the expected absorption for bulk silicon (without a strong field). As has been discussed in Chapter 4, the width of the depletion region under reverse bias will be large, (about $30\mu\text{m}$ at zero volts in comparison with a mesa thickness of one μm) and the current

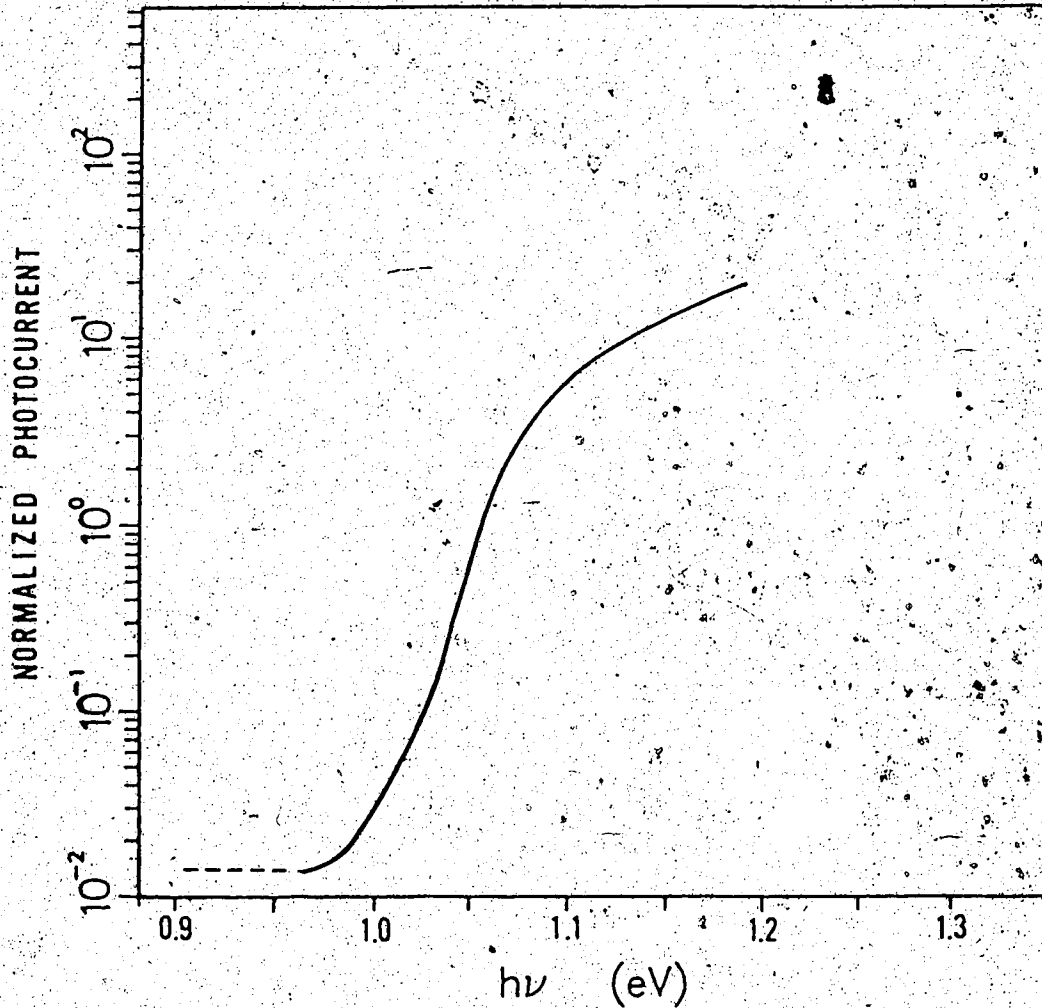


Fig. 5.5 Photoconductivity for bulk silicon. ✓
The measured photocurrent has been normalized to correspond to the optical absorption coefficient at $h\nu = 1.2\text{eV}$. The dashed line indicates the noise level in the measurement.

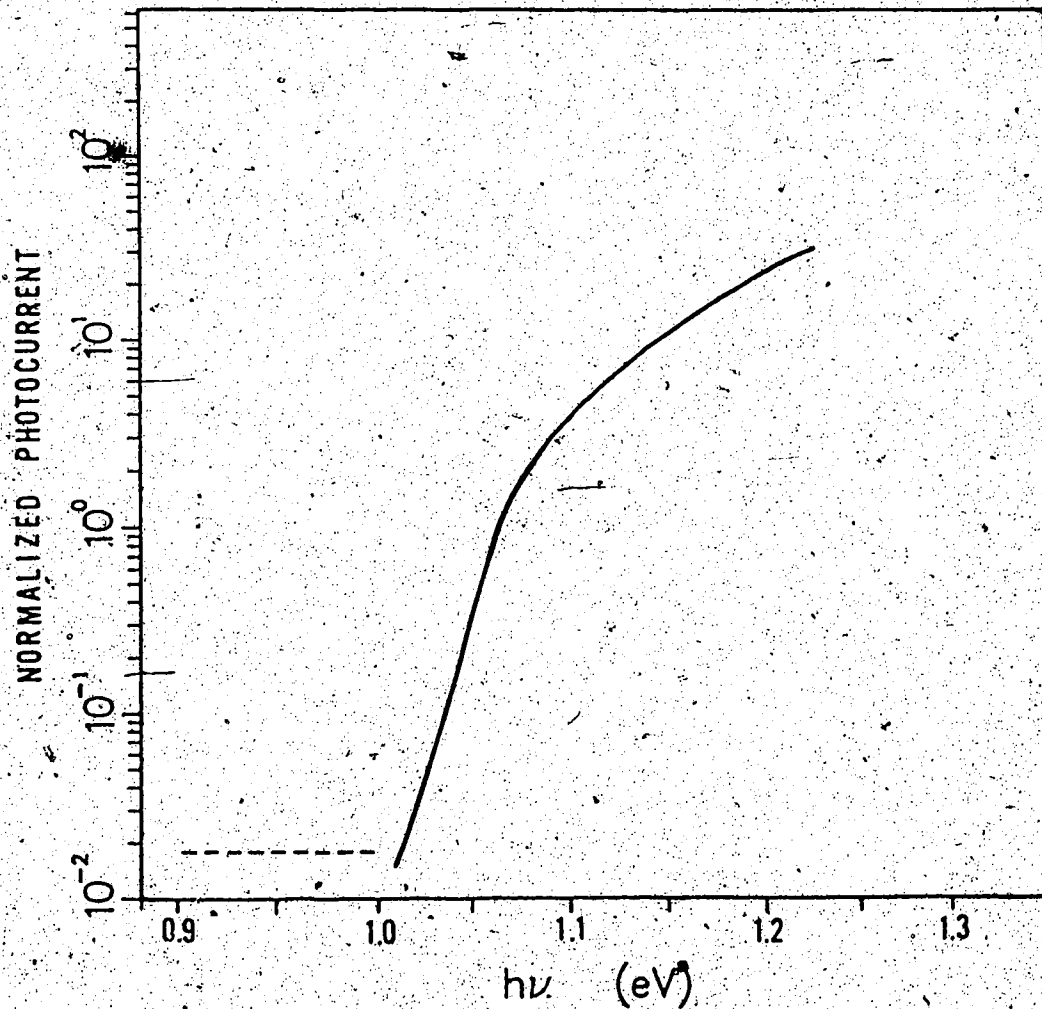


Fig. 5.6. Typical photoconductivity measurement of a nipi. From MBE 360 #1E, split contact mesa. The measured photocurrent has been normalized to correspond to the optical absorption coefficient at $h\nu = 1.2\text{eV}$. The dashed line indicates the noise level of the measurement. The measurement was taken at 0.5v reverse bias with a voltage across the split contacts of $V_a = 0.1\text{v}$.

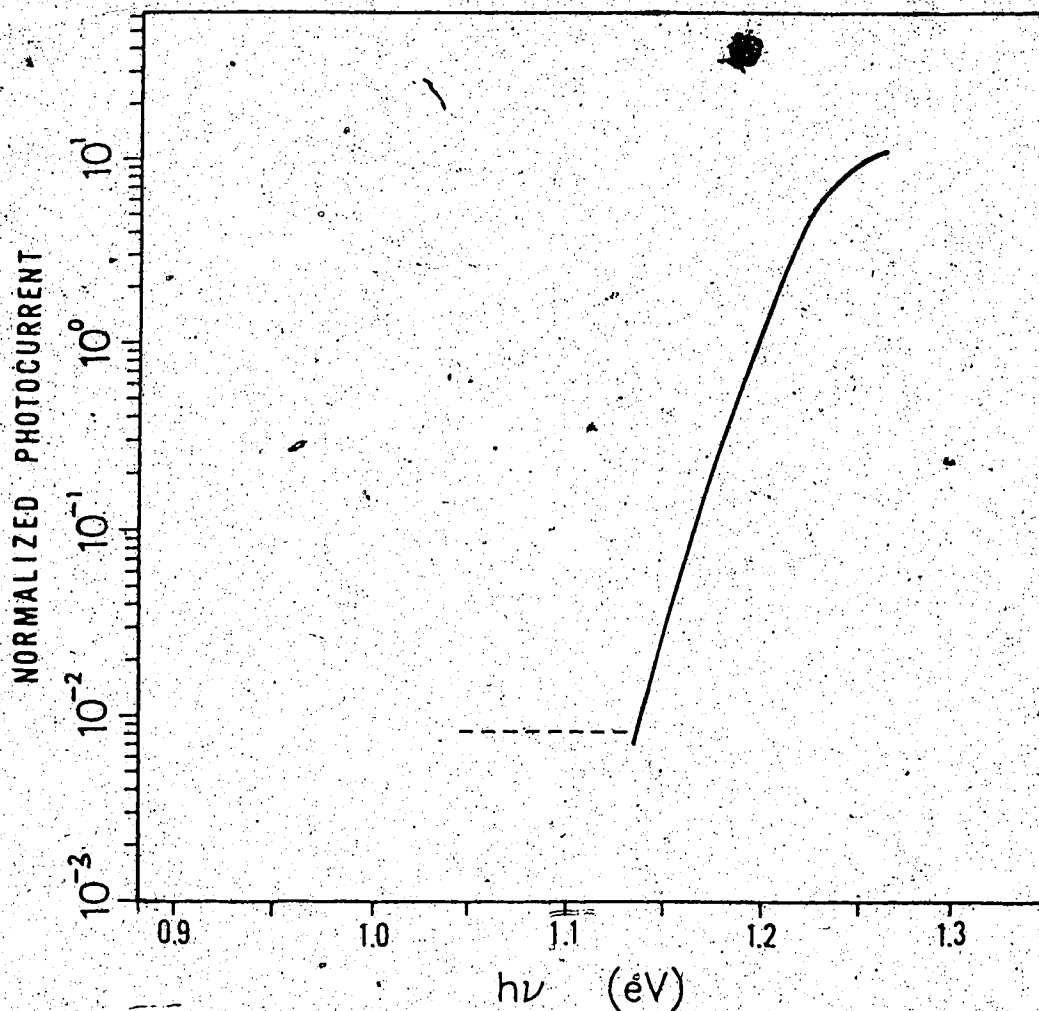


Fig. 5.7 Typical photoconductivity measurement of a nipi at 77°K. From MBE 360 #1E, split contact mesa. The measured photocurrent has been normalized to correspond to the optical absorption coefficient at $h\nu = 1.25$ eV. The dashed line indicates the noise level of the measurement. The measurement was taken with no external bias and with a voltage across the split contacts of $V_b = 0.1$ v.

through the substrate may in fact be larger than the current through the nipi. Hence, the photoconductive current that is due to the substrate may 30 times larger than the nipi current. For the absorption shift to be observed, it would have to be at least a factor of 30 stronger than the bulk absorption.

(2) A second complication may have reduced the internal field in the nipi. The graded junctions that have been observed with the SIMS measurements will have two effects. The graded profile as compared to a step profile will result in a lower built in electric field. If a sinusoidal approximation is used, the field will be reduced by a factor of 0.6. The rolloff in the doping profile will result in compensation of the opposite impurity resulting in a lower overall doping concentration. The compensation effects will become particularly large in the case when one of the doping concentrations is much higher. Unfortunately, most of the photoconductivity measurements were made with such a sample MBE 360 #1E, ($N_a > N_d$). Instead of the expected fields of up to $100 \text{ V}/\mu\text{m}$, they may have been more on the order of $5\text{-}40 \text{ V}/\mu\text{m}$ which, as can be seen from Fig. 5.2, reduces the absorption shift significantly.

One possible method of reducing the substrate effects which is currently being considered is through lateral injection of light into the mesa through the side. In order to improve the internal field strength, new nipi's are being grown with wider wells and higher doping concentrations. The possibility of setting up an ion beam doper for the p-type impurity is also being considered. With each of these improvements, the chances of observing the expected shift in the absorption become more likely.

Chapter 6

Summary and Conclusions

Since the commencement of this project, much of the necessary groundwork for the fabrication of silicon doping superlattices has been completed and several major accomplishments have been attained. The achievements are the result of a great deal of collaboration and cooperation. I am pleased to have participated in this effort.

The first part of this project involved theoretical calculations of the tunable absorption coefficient due to the Franz-Keldysh effect in a silicon doping superlattice. These calculations included phonon interaction related to the indirect band structure of silicon and a modulated potential. The theory predicted that a small but measurable increase in the absorption should be observable.

Next, work was initiated on the fabrication of nipi's with the intention of measuring the absorption shift. The first step involved the design and fabrication of a shadow mask. Etching procedures were developed and several silicon shadow masks have since been produced. These masks were used to produce superlattice mesas with built-in contact selectivity during MBE growth. The design of the shadow mask has gone through two phases of development. A pattern mask set has also been designed and processing methods developed for producing selective contacts on the nipi's.

Electrical measurements show that a nipi has been produced with selective contacts. However, larger than expected leakage currents were observed and for this reason, a large portion of this work has been devoted to the analysis of the electrical characteristics of both the contacts and the nipi's. Electrical results show that

metal-semiconductor contacts have been produced with the rectifying qualities necessary for the nipi contacts. When these contacts are placed on the nipi mesa, their rectifying ability is greatly reduced. Surface etching appears to restore the contact qualities. The electrical behavior of the nipi has been compared with conventional current transport theory. Substrate effects still seem to be substantial in the nipi despite the improved mask design. The conductance in the layers has been measured with a split contact arrangement and the conductance is found to vary with an applied bias across the nipi. A large background conductance is also present. These results are still tentative due to an insufficient number of processed samples at the time this work was completed. More work is needed to verify and further investigate these effects.

Measurements of the nipi photoconductivity were made but to date the expected shift in the absorption spectrum has not been observed. The observed photocurrent may be due to substrate absorption rather than absorption in the nipi. As well, the reduced electrical field due to the graded junctions has lowered the magnitude of the expected absorption shift. These two complications have resulted in an unobservable variation in the absorption coefficient. The phenomenon may still be observable with different superlattice designs and measurement methods.

Several goals have been achieved in the course of this project. Calculations of the tunable absorption were carried out for the first time in an indirect bandgap nipi. A shadow mask was fabricated from a silicon wafer using an anisotropic etch and used to make grown-in selective contacts during MBE growth. Selective contacts using the

shadow mask method have been made for the first time on a silicon nipi. As well, some characterization of the electrical behavior of the nipi's has been carried out.

This project started with a fairly high goal and a great deal of the fundamental work required for silicon nipi research has been done. However, there are still many unresolved questions and problems left to investigate. In particular, effects associated with the substrate need to be addressed. More study is also needed of the quality of the superlattice layers. These basic issues need to be resolved before nipi's with thinner layers can be studied. Research on silicon doping superlattices is continuing at both the University of Alberta and the NRC Microstructural Sciences Laboratory.

REFERENCES

1. L. Esaki and R. Tsu, IBM J. of Research and Development 14, 61, 1970.
2. G.H. Döhler, Phys. Status Solidi 52, 533, 1972.
3. G.H. Döhler, CRC Crit. Rev. in Solid State and Materials Science 13, 97, 1987.
4. Y. Shiraki, J. Vac. Sci. Tech. B3, 725, 1985.
5. Y. Ota, Thin Solid Films 106, 1, 1983.
6. C. Priester, G. Allen and M. Lannoo, Phys. Rev. B35, 2904, 1987.
7. W. Enge and H. Heluan, Chin. Phys. 6, 226, 1986.
8. H.G. Schmidt-Weinmar, K.H. Teo, J.N. McMullin and G.H. McKinnon, Can. J. Phys. 65, 1064, 1987.
9. K. Nakagawa and Y. Shiraki, Solid State Comm. 58, 819, 1986.
10. E.D. Ahlers and F.G. Allen, Proc. of the 2nd Int. Silicon MBE Symposium, Hawaii, Oct. 1987 (Electrochem. Soc., in press).
11. J.N. McMullin, G.H. McKinnon, H.G. Schmidt-Weinmar and K.H. Teo, Superlattices and Microstructures (in press).
12. G.H. Döhler, H. Künzel and K. Ploog, Phys. Rev. B25, 2616, 1982.
13. C.Y. Chang, Y.K. Fang and S.M. Sze, Solid-State Electronics 14, 541, 1971.
14. G.H. Döhler, G. Hasnain and J.N. Miller, Appl. Phys. Letters 49, 704, 1986.
15. C.J. Chang-Hasnain, G. Hasnain, N.M. Johnson, G.H. Döhler, J.N. Miller, J.R. Whinnery and A. Dienes, Appl. Phys. Letters 50, 915, 1987.

16. G. Hasnain, C.J. Chang-Hasnain, G.H. Döhler, J.N. Miller, N.M. Johnson, J.R. Winnery and A. Dienes, *Superlattices and Microstructures* 3, 277, 1987.
17. D. Landheer, M.W. Denhoff, M. Buchanan, T.E. Jackman, G.H. McKinnon, K.H. Teo and J.A. Jackman, *Appl. Phys. Letters* (in press).
18. W. Kern and C.A. Deckert, in *Thin Film Processes*, J.L. Vossen and W. Kern Eds., Academic Press, Orlando, 401, 1985.
19. R.M. Finne and D.L. Klein, *J. Electrochem. Soc.: Solid State Science* 111, 965, 1967.
20. J.A. Jackman, P. Williams, T.E. Jackman and D.C. Houghton, in *Sims VI*, (to be published).
21. W. Schottky, *Naturwiss.* 26, 843, 1938.
22. R.S. Muller and T.I. Kamins, *Device Electronics for Integrated Circuits*, J. Wiley and Sons, Toronto, 1977.
23. S.M. Sze, *Physics of Semiconductor Devices*, J. Wiley and Sons, Toronto, 1969.
24. H.C. Card and E.H. Rhoderick, *J. Phys. D: Appl. Phys.* 4, 1602, 1971.
25. H.K. Henisch, *Rectifying Semiconductor Contacts*, Oxford at the Clarendon Press, Oxford, 1957.
26. R.J. Archer and M.M. Atalla, *Annals of the N.Y. Academy of Sciences* 101, 697, 1963.
27. J.M. Andrews and J.C. Phillips, *Phys. Rev. Letters* 35, 56, 1975.
28. P. Janega, personal communication.
29. G.H. Döhler, H. Künzel, D. Olego, K. Ploog, P. Ruden, H.J. Stolz, and G. Abstreiter, *Physical Review Letters* 47, 864, 1981.

30. G.H. Döhler and P.P. Ruden, *Physical Review* **B30**, 5932, 1984.
31. W. Franz, *Z. Naturforsch.* **13**, 484, 1958; L.V. Keldysh, *Soviet Physics JETP* **7**, 788, 1958.
32. D.E. Aspnes and N. Bottka, in *Semiconductors and Semimetals*, Ed. R.K. Willardson and A.C. Beer, Vol. 9, Academic Press, New York, 457, 1972.
33. C.M. Peiching, *Physical Review* **138**, A924, 1965.
34. B.Y. Loo, J.D. Dow and F.C. Weinstein, *Physical Review* **B4**, 4424, 1971.
35. W.C. Dash and R. Newman, *Physical Review* **99**, 1151, 1955.
36. A. Frova, P. Handler, F.A. Germano and D.E. Aspnes, *Physical Review* **145**, 575, 1966.
37. G.G. MacFarlane, T.P. MacLean, J.E. Quarrington and V. Roberts, *Physical Review* **111**, 1245, 1958.
38. W. Spitzer, in *Semiconductors and Semimetals*, Ed. R.K. Willardson and A.C. Beer, Vol. 3, Academic Press, New York, 17, 1967.
39. J.I. Pankove, *Optical Processes in Semiconductors*, Prentice Hall, Englewood Cliffs, N.J., 1971.
40. W.G. Spitzer and H.Y. Fan, *Physical Review* **108**, 268, 1957.
41. P.A.H. Hart, in *Handbook on Semiconductors Vol. 4 Device Physics*, T.S. Moss Ed., vol. 4 ed. by C. Hilsum, North-Holland, New York, 87, 1981.

Appendix A

Current Transport Models

The mechanisms of current transport in metal-semiconductor (M-S) and semiconductor-semiconductor junctions are reviewed here. The following theories have been used in the analysis of the various junctions encountered in this project. Only the results of each model are outlined.

1. Schottky Barrier Diffusion Theory

The current flow in a M-S junction will depend on the ability of carriers to cross the built in potential barrier resulting from the M-S interface. The current in the depletion region depends on the local field and on the carrier concentration gradient. The current can be obtained by integrating the equations for carrier diffusion and drift across the depletion region [22]. For a metal on n-type silicon the diode equation will be:

$$I_{ms} = I_{ms0} (e^{qV_a/kT} - 1) \quad (A.1)$$

where

$$I_{ms0} = A q \mu_n N_c \left[2q(\phi_i - V_a)N_d/\epsilon \right]^{1/2} \exp(q\phi_{Bn}/kT) \quad (A.2)$$

Two features are important to note. The reverse bias current is not constant but varies with the square root of the applied voltage. The magnitude of the current is a very sensitive function of the barrier height, $q\phi_{Bn}$.

2. P-N Junction Diffusion Theory

The diffusion of minority carriers in the quasi-neutral regions determines the current transport in the ideal diode analysis [22]. The minority carriers will recombine based on the Shockley-Hall-Read (SHR) model. The minority carrier distribution will follow an exponential decay with the diffusion length, L_p determined by $\sqrt{D_p \tau_p}$ ($L_n = \sqrt{D_n \tau_n}$ for electrons) where τ_p and τ_n are the minority carrier lifetimes. The diffusion current is given by:

$$I_s = I_{s0} (e^{qV_a/kT} - 1) \quad (A.3)$$

where

$$I_{s0} = A q n_i^2 \left(\frac{D_p}{N_d L_p} + \frac{D_n}{N_a L_n} \right) \quad (A.4)$$

In this case, the saturation current I_{s0} is independent of the applied voltage. The side of the junction with the lower doping will determine I_{s0} since L_n and L_p also decrease with lower doping concentrations.

3. Generation-Recombination Currents

Under bias, the electron and hole populations in the space charge region will be disrupted from their equilibrium values. This will result in a net rate of generation or recombination of carriers which can significantly alter the junction current. This is equally true in p-n junctions and M-S junctions. The total current can be found by integrating the recombination rate over the space charge region [22]:

$$I = A \frac{q n_i x'}{2\tau} \cdot \frac{(e^{qV_a/kT} - 1)}{(e^{qV_a/2kT} + 1)} \quad (A.5)$$

Under forward bias (with $V_a > kT/q$), there will be an excess of

carriers in the depletion region ($n \cdot p > n_i^2$) which will result in a net recombination current and the equation may be reduced to:

$$I_r = A \frac{q n_i x'}{2\tau} e^{qV_a/2kT} \quad (A.6)$$

where x' is some portion of the space charge region but can be approximated with x_d [23]. The important thing to note is the $kT/2q$ dependence rather than kT/q as expected in the ideal diode analysis.

Under reverse bias, the carriers in the depletion region will be swept out by the field causing $n \cdot p$ to be less than n_i^2 . In this case there will be a net generation of carriers and the equation becomes:

$$I_s = A q n_i x_i / 2\tau \quad (A.7)$$

where

$$x_i = x_d(V_a) - x_d(0) = \sqrt{\frac{2\epsilon}{q(N_d + N_a)}} \left[\sqrt{\phi_i - V_a} - \sqrt{\phi_i} \right] \quad (A.8)$$

For $V_a \gg \phi_i$ the generation current follows the same square root dependence on voltage seen in the M-S junction.

The value of the effective lifetime τ is not known with any precision. This lifetime is not the same as the minority carrier lifetime but it is expected to follow the same behavior [5]. The following values which are used in this work have been estimated from a survey by Slotboom [41]:

$$\text{For } N_d \leq 10^{15} \quad \tau \approx 2 \mu\text{sec}$$

$$\text{For } N_d \approx 10^{18} \quad \tau \approx 0.2 \mu\text{sec}$$

These are approximations only but they have been partially confirmed by some of the measurements in this work (Section 3.3 and Section 4.3).

In order to provide some method of comparison of the current models and also to be able to extract some of the diode parameters from the measurements, the current-voltage characteristics can be defined in terms of a resistance. The contact resistance for a metal-semiconductor junction can be defined as:

$$R_c^{-1} = \left. \frac{\partial I}{\partial V_a} \right|_{V_a \rightarrow 0} \quad (A.9)$$

We extend this definition to apply to the p-n junction as well the M-S junction and define the junction resistance, $R_o = R_c$. This resistance can be easily calculated from the slope of the measured I-V curves. From the derivatives of Eqns. A.1, A.3 and A.5 taken at $V = 0v$, the following relationships are found.

For the Schottky diode model:

$$R_o = kT / qI_{ms0}(0) \quad (A.10)$$

For the ideal diode model:

$$R_o = kT / qI_{s0} \quad (A.11)$$

For the generation-recombination model:

$$R_o = 2kT / qI_{ro} = 2kT / qI_{s0} \quad (A.12)$$

where

$$I_{s0} = I_{ro} = A q n_i x_d(0) / 2\tau \quad (A.13)$$